

**MBE GROWTH OF III-V MATERIALS WITH
ORIENTATION-PATTERNED STRUCTURES
FOR NONLINEAR OPTICS**

A DISSERTATION
SUBMITTED TO THE DEPARTMENT OF MATERIALS SCIENCE AND
ENGINEERING
AND THE COMMITTEE ON GRADUATE STUDIES
OF STANFORD UNIVERSITY
IN PARTIAL FULFILLMENT OF THE REQUIREMENTS
FOR THE DEGREE OF
DOCTOR OF PHILOSOPHY

Xiaojun Yu

March 2006

© Copyright by Xiaojun Yu 2006
All Rights Reserved

I certify that I have read this dissertation and that, in my opinion, it is fully adequate in scope and quality as a dissertation for the degree of Doctor of Philosophy.

James S. Harris, Jr. (Principal Adviser)

I certify that I have read this dissertation and that, in my opinion, it is fully adequate in scope and quality as a dissertation for the degree of Doctor of Philosophy.

Martin M. Fejer

I certify that I have read this dissertation and that, in my opinion, it is fully adequate in scope and quality as a dissertation for the degree of Doctor of Philosophy.

William D. Nix

Approved for the University Committee on Graduate Studies

ABSTRACT

There are numerous applications of nonlinear optical frequency conversion in the infrared, ranging from generation of coherent radiation for spectroscopy and military applications, to wavelength conversion in communication systems. Semiconductors, such as $\text{Al}_x\text{Ga}_{1-x}\text{As}$ and GaP have excellent properties for nonlinear frequency conversion, in particular large nonlinear coefficients and transparency throughout the mid-infrared. However, due to the absence of birefringence, quasi-phasematching (QPM) has to be used for the phasematching, requiring a modulation of the sign of the nonlinear optical coefficient along the optical path in the material. In this work, we have developed an all-epitaxial process to fabricate orientation-patterned $\text{Al}_x\text{Ga}_{1-x}\text{As}$ and orientation-patterned GaP structures, used for both bulk-like and waveguide devices. Various nonlinear optical interactions have been demonstrated which show that orientation-patterned $\text{Al}_x\text{Ga}_{1-x}\text{As}$ is a promising candidate for infrared applications.

Our orientation-patterned GaAs template is fabricated in three steps. First, we use the polar-on-nonpolar growth of GaAs/Ge/GaAs heterostructure to control the lattice inversion. The orientation pattern is then defined by a combination of photolithography and a series of selective chemical etching steps. Template and waveguide growth is completed using MBE regrowth. Critical regrowth issues are elimination of antiphase defects within each single domain of the template while still maintaining the induced antiphase domains at the pattern boundaries. Appropriate growth conditions were developed which met these challenges and produced vertical propagation of domain boundaries under all MBE conditions tested. Low-corrugation template has been achieved by optimizing the growth conditions of GaAs on Ge. QPM periods demonstrated are short enough to phasematch any interaction in the transparency range of $\text{Al}_x\text{Ga}_{1-x}\text{As}$.

Using this technique, we fabricated low-loss $\text{Al}_x\text{Ga}_{1-x}\text{As}$ QPM waveguide devices and demonstrated second harmonic generation with a pump laser at 1.55 μm . A waveguide loss, ~ 4.5 dB/cm at 1.55 μm , was measured, which is close to that of the unpatterned waveguides. Record-high conversion efficiency, 43 %W⁻¹, was demonstrated, which is the highest value reported to date for AlGaAs nonlinear waveguides. These achievements provide solid basis for the fabrication of highly efficient nonlinear optical devices based on the GaAs material system.

In addition to the orientation-patterned GaAs growth, we also investigated the growth of single-phase GaP on Si, aiming at transferring growth technologies of GaAs on Ge to GaP on Si. By controlling proper growth conditions, we successfully grew two distinct single-phase GaP on Si and fabricated the first orientation-patterned GaP template on Si. Further progress will lead to GaP-based nonlinear devices for high power operation with a broader wavelength region.

ACKNOWLEDGEMENTS

This dissertation would not have been possible without the contribution of many individuals to whom I am greatly indebted. First of all, I would thank my advisor, Prof. James S. Harris for guidance of this project. Prof. Harris offered me this great opportunity to work in his research group on this exciting and challenging project. Without his vision, thoughtfulness and brilliance, most of the achievement would not be possible. It is also a great experience to work with Prof. Harris. In his group, I enjoyed the freedom to make decisions and to try every absurd idea. His influence on my career, vision and learning process is tremendous. I will benefit from it for the rest of life.

I am also deeply indebted to Prof. Martin M. Fejer, who is, in effect, my co-advisor. Most of the work was carried out under his direct supervision with his students. I would thank him for so many instructive discussions and effective suggestions, not only related to nonlinear optics, but also regarding on crystal growth, and device fabrication. Without his work, most of the experimental success would not have been possible.

I would express my gratitude to Prof. William D. Nix. Prof. Nix has kindly served in all of my required committees and was always patient to discuss questions regarding on my own research whenever approaching to him. His enthusiasm on the material research and on educating young researchers also influenced me. I would also thank Prof. Robert Feigelson and Prof. Thomas Kenny for serving in my oral committee. I would also be grateful to Dr. Fu-Mei Chen for supporting me at Stanford via the Stanford Graduate Fellowship program. This fellowship gave me a great chance to take the time to explore different ideas in the initial phase of my research without having to worry about funding and I would like to thank our department for giving me this great opportunity.

Most of our works done in this project are based on the achievement of previous students and the collective efforts of my coworkers. I would particularly thank Dr. Loren Eyres and Dr. Thierry Pinguet. They helped me on the initial stage of this project and provided a lot of useful advice. I would thank Luigi Scaccabarozzi. Without him, most of the fabrications and measurements would not have been possible. I would also thank Paulina Kuo, who spent a lot time with me to recover all the missing techniques since the graduation of previous students. Other contributors to this project including Ofer Levi and Konstantin Vodopyanov also provided instructive discussions which induced me to think questions from various aspects. I would also thank Angie Lin, who will take over my work, about her help on my latest work. I

wish her good lucks and hope MBE treats her nicely. I would also wish good luck to Yijie.

The experience in Harris group would never be forgotten by me, not only because of the excitements in the research, but also because of the warm-hearted colleague in this group. The merit of being in a big group is that whenever I had questions, I could get help from members who belong to various departments. I would especially thank Vincent, Mark, Qiang and Xian. Without their generous help, I would have spent much longer struggling with machine maintenance and have broken the machines without knowing why. I would also be grateful to Junxian Fu, the other one of “Jun”-brothers, with whom we worked on the same machine for five years. We not only cooperated on maintenance of MBE system, but also frequently discussed a variety of topics. We built up a close friendship over the five years. I wish him a brilliant future after stepping into industry. I would also thank Kai, Seth, Homan, Hopil, Evan, and Thomas, who kept the MBE lab organized and always brought joyfulness to lab-members; thank Yu-Husan, who worked with me on growth of GaAs LEDs on Ge-on Si. I wish good luck to all MBE growers, especially Donghun, who is going to take over the job of taking care of the MBE system. I would also thank some non-growers in Harris group, especially Rafael, who helped us update the control system of MBE and relieved our work load. I also greatly appreciate Ke and Zhigang, who joined the Harris group at the same time as me and brought a lot fun in addition to the work life. I would thank all other Harris group members too, for keeping this group as a big family.

Of course, none of this work would have ever happened without the people that work to keep things running smoothly. Gail Chun-Creech deserves credit for keeping the Harris group organized despite all of our individual problems and our advisor’s busy schedule. I would also thank our departmental secretary, Stephanie, who maintained an organized record for me.

I would also specially thank all my friends, both in our department, Yoacheng, Gang, Liangliang, et al; and out of our department, Xin, Liqiang, et al. The list would be very long if I want to mention everyone. They gave me a lot of help, brought a lot of fun to me and made my life in Stanford so enjoyable.

In the end, I would dedicate this work to my family and Yue. My parents and my brother and sister in China always showed their strongest support and their selfless care, especially my parents, who worked very hard to support me financially untill college and made it possible for me to come to Stanford. I hope they are proud of my work. The last but not least, I would thank my love, Yue, who met me at Stanford. She always supported me, brought me happiness and made my life so wonderful. Without her care, my graduate life would be miserable.

Table of Contents

ABSTRACT	v
ACKNOWLEDGEMENTS	vii
Table of Contents	ix
List of Tables	xii
List of Illustrations	xiii
INTRODUCTION	1
1. 1 INFRARED SOURCES BASED ON NONLINEAR OPTICS (NLO)	1
1. 1. 1 <i>Applications of infrared sources</i>	1
1. 1. 2 <i>Advantages of NLO sources</i>	1
1. 2 NLO IN OPTICAL COMMUNICATIONS.....	3
1. 3 CANDIDATE MATERIALS FOR INFRARED NLO	4
1. 4 DISSERTATION OVERVIEW.....	6
Chapter 2 PHASEMATCHING IN SEMICONDUCTORS	7
2. 1 THEORY OF FREQUENCY CONVERSION	7
2. 1. 1 <i>Coupled equations</i>	8
2. 1. 2 <i>Conversion efficiency</i>	9
2. 1. 3 <i>Effect of propagation loss</i>	12
2. 2 PHASE MATCHING APPROACHES.....	13
2. 3 PHASEMATCHING IN III-V SEMICONDUCTORS	17
2. 3. 1 <i>BPM nonlinear waveguides</i>	17
2. 3. 2 <i>MPM nonlinear waveguides</i>	18
2. 3. 3 <i>QPM in III-V materials</i>	19
2. 4 GOAL OF THIS DISSERTATION WORK	22
Chapter 3 ALL-EPITAXIAL ORIENTATION-PATTERNED GaAs TEMPLATE	23
3. 1 MOLECULAR BEAM EPITAXY	23
3. 2 PROCESS FLOW OF OP-GAAS TEMPLATE	25
3. 3 GROWTH OF INVERTED-GAAS/Ge/GAAS HETERO-STRUCTURES.....	27
3. 3. 1 <i>Why use Ge?</i>	27
3. 3. 2 <i>Characteristics of GaAs growth on Ge</i>	27
3. 3. 3 <i>Requirements for single-phase GaAs growth on Ge</i>	28

3. 3. 4	<i>Phase control of GaAs on Ge</i>	32
3. 3. 5	<i>Inverted-GaAs/Ge/GaAs growth</i>	34
3. 4	DRAWBACKS OF PREVIOUS OP-GAAS TEMPLATE GROWTH.....	35
3. 4. 1	<i>Chemical etching</i>	35
3. 4. 2	<i>Template corrugation</i>	37
3. 5	LOW-CORRUGATION TEMPLATE	38
3. 5. 1	<i>Direct reduction of layer thickness</i>	38
3. 5. 2	<i>Approaches to reduce template-corrugation</i>	40
3. 5. 3	<i>Substrate smoothing</i>	40
3. 5. 4	<i>Thin GaAs growth on Ge</i>	43
3. 6	FURTHER INVESTIGATION OF GROWTH MECHANISMS	45
3. 6. 1	<i>Effects of flux ratio on APB planes</i>	45
3. 6. 2	<i>Effect of Ge surface anneal</i>	47
3. 6. 3	<i>Growth rate mismatch</i>	47
3. 7	OP-GAAS TEMPLATE REGROWTH AND APPLICATIONS	48
3. 7. 1	<i>OP-GaAs template regrowth results</i>	49
3. 7. 2	<i>Thick film results and devices results</i>	51
Chapter 4	LOW-CORRUGATION AlGaAs QPM WAVEGUIDES	53
4. 1	INTRODUCTION	53
4. 2	WAVEGUIDE STRUCTURE DESIGN.....	55
4. 3	ANALYSIS OF LOSS MECHANISMS	56
4. 3. 1	<i>Losses due to the periodic waveguide corrugations</i>	57
4. 3. 2	<i>Losses due to the sidewall roughness</i>	59
4. 3. 3	<i>Losses due to random interfacial roughness</i>	60
4. 3. 4	<i>Regrowth-induced corrugation—v-grooves</i>	61
4. 4	FORMATION OF V-GROOVES	62
4. 4. 1	<i>Growth temperatures and V/III flux ratio</i>	62
4. 4. 2	<i>Al composition</i>	67
4. 4. 3	<i>MEE growth</i>	67
4. 4. 4	<i>Discussions</i>	68
4. 5	WAVEGUIDE GROWTH RESULTS	68
4. 6	WAVEGUIDE FABRICATION	70
4. 6. 1	<i>Dry etching</i>	70
4. 6. 2	<i>Diffusion-limited etching</i>	71

4. 7 OPTICAL CHARACTERIZATION.....	72
4. 7. 1 <i>Loss measurement</i>	73
4. 7. 2 <i>Second harmonic generation (SHG) measurement</i>	79
4. 8 CONCLUSION	84
Chapter 5 GROWTH OF OP-GaP TEMPLATE	86
5. 1 INTRODUCTION.....	86
5. 2 REVIEW ON GAP GROWTH ON SI AND ITS CHALLENGES	87
5. 3 SINGE-PHASE GAP GROWTH ON SI.....	89
5. 3. 1 <i>GaP phase control</i>	89
5. 3. 2 <i>Surface roughness</i>	99
5. 4 OP-GAP TEMPLATE FABRICATION	103
5. 4. 1 <i>Process flow</i>	103
5. 4. 2 <i>Etching and cleaning</i>	104
5. 4. 3 <i>Two single-phase GaP growth</i>	105
5. 5 CONCLUSIONS	107
Chapter 6 SUMMARY AND FUTURE WORK	108
6. 1 ACCOMPLISHMENT	108
6. 1. 1 <i>Material growth</i>	108
6. 1. 2 <i>Device fabrication and optical characterization</i>	109
6. 2 FUTURE WORK.....	109
6. 2. 1 <i>Low-loss waveguides design and fabrication</i>	109
6. 2. 2 <i>High power DFG waveguide</i>	111
6. 2. 3 <i>OP-GaP thick film growth</i>	112
6. 3 CONCLUSIONS	113
BIBLIOGRAPHY	114

List of Tables

Table 1-1 Potential materials used for infrared nonlinear optics.....	5
Table 3-1 Orientations of GaAs on Ge under different growth conditions	33
Table 4-1 Stable facet angles vs growth temperatures and V/III flux ratios	66
Table 4-2 Coupling coefficient for the waveguides with various widths.....	82
Table 5-1 Orientations of GaP on Ge under different growth conditions	99
Table 5-2 Surface roughness of GaP.....	102
Table 6-1 Normalized conversion efficiency ($W^{-1}cm^{-2}$) vs. waveguide dimensions.....	111

List of Illustrations

Figure 1-1 Illustrations of frequency conversion	3
Figure 2-1 Mode confinement in (a) bulk devices (b) waveguides.....	11
Figure 2-2 SHG power in a function of length with various losses	13
Figure 2-3 Second harmonic output power in function of distance (a) ideal phasematching; (b) first order quasi-phasematching; (c) higher-order quasi-phasematching; (d) non-phasematched	14
Figure 2-4 Birefringent phasematching.....	15
Figure 2-5 Materials structure for QPM.....	16
Figure 2-6 Form birefringence phasematching in GaAs nonlinear waveguides	18
Figure 2-7 MPM phasematching techniques in GaAs/AlGaAs waveguides.....	18
Figure 2-8 GaAs structure with rotation about [001] axis by 90°	20
Figure 2-9 QPM structure by wafer bonding	20
Figure 2-10 QPM structure by regrowth on orientation-patterned template	21
Figure 3-1 Top view of a simple MBE chamber: showing the essential growth sources, shutters, beam flux detector and the RHEED system.....	24
Figure 3-2 All-epitaxial fabrication process of orientation-patterned GaAs.....	26
Figure 3-3 GaAs lattice inversion achieved by inserting a Ge intermediate layer	27
Figure 3-4 Atomic arrangements of Ge and GaAs/Ge structure projected in (110) plane (a) Ge surface with single-atomic-layer steps; (b) Ge surface double-atomic-layer steps; (c) mixed-oriented-GaAs grown on Ge with single-atomic-layer steps; (d) single-oriented-GaAs grown on Ge with double-atomic-layer steps.....	29
Figure 3-5 Single-phase GaAs on Ge through APD annihilations.....	31
Figure 3-6 $\beta(2\times 4)$ surface reconstruction of GaAs (001) surfaces and related RHEED pattern.....	32
Figure 3-7 Cross-sectional SEM image of the inverted-GaAs/Ge/GaAs structure	35
Figure 3-8 Double-etch-stop template structures and chemical etching processes.....	36
Figure 3-9 Topviews of the etch pits formed during chemical etching (a) OM image of the template after etching; (b) SEM image of the etch pits.....	37
Figure 3-10 AFM image of the pits in GaAs film grown on Ge thin layer.....	38
Figure 3-11 AFM images of the GaAs grown on Ge by MEE.....	39
Figure 3-12 Cross-sectional TEM images of the pits GaAs grown on Ge.....	40
Figure 3-13 AFM images of the GaAs growth on the substrates with different miscut angles	41

Figure 3-14 AFM image of template structure with ~20nm GaAs grown on Ge.....	44
Figure 3-15 HRTEM of the (110) cross-section of the low corrugation template	45
Figure 3-16 XTEM of the GaAs grown on Ge with APDs	46
Figure 3-17 Ga-adatoms diffusion on the GaAs surface with double domains.....	48
Figure 3-18 Corrugations on the domain boundaries after regrowth	49
Figure 3-19 Domain boundaries quality improvement	50
Figure 3-20 Morphologies of the OP-GaAs template after regrowth.....	51
Figure 3-21 Thick OP-GaAs film grown by HVPE	52
Figure 4-1 Waveguides structure and the optical mode at 1.55 μm	56
Figure 4-2 Scattering in QPM waveguides due to the template corrugations	58
Figure 4-3 Effect of the waveguide corrugations on the waveguide loss.....	58
Figure 4-4 Waveguide loss vs wavelenghts due to template corrugations.....	59
Figure 4-5 Morphologies of both patterned and unpatterned waveguides	60
Figure 4-6 Losses vs waveguide widths for both various waveguides.....	61
Figure 4-7 SEM images of the QPM waveguides growth on template with 45-nm template corrugation	62
Figure 4-8 Top views of the AlGaAs film growth on the patterned template.....	63
Figure 4-9 Top views of the AlGaAs film growth on the patterned template.....	63
Figure 4-10 Cross-sectional SEM image on the domain boundaries with constant growth conditions	64
Figure 4-11 Cross-sectional SEM image of the domain boundaries with changing growth temperatures	65
Figure 4-12 Illustration of the facet angles on the domain boundaries	66
Figure 4-13 Optical microscopy images of waveguide regrowth morphologies (a) On templates with 1000- \AA corrugation without optimized conditions; (b) On low-corrugation template with 200- \AA corrugation after optimization	69
Figure 4-14 SEM of the regrowth on the patterned templates (a) Top-view; (b) Cross- sectional view	70
Figure 4-15 SEM of the fabricated waveguides	72
Figure 4-16 Fabry-Perot method for loss measurement	73
Figure 4-17 Loss of the QPM waveguides and the unpatterned waveguide grown on the low corrugation template.....	75
Figure 4-18 Waveguides layout for measuring the losses at 775 nm for both the patterned and unpatterned waveguides	76

Figure 4-19 SHG conversion efficiency from the 2-mm-long QPM gratings at different locations in the plain waveguides.....	78
Figure 4-20 SHG conversion efficiency from the waveguides with five QPM periods. (a) SHG conversion efficiency vs input fundamental wavelength; (b) Logarithm plot of the SHG efficiency in a function of position.....	78
Figure 4-21 Optical setup for measuring loss and second harmonic generation.....	80
Figure 4-22 SHG tuning curve of an 8-mm long QPM waveguide.....	81
Figure 4-23 Relationship of SHG power and fundamental input power.....	82
Figure 4-24 Dependence of SHG conversion efficiency on sample length.....	84
Figure 5-1 Phasematching for 2 μm -pumped OPOs in zincblende semiconductors. The vertical extent of GaP indicates a nearly wavelength independent coherence length and very wide phasematching bandwidth.....	87
Figure 5-2 AFM images of GaP on Si without exposure control a: $T_g=510^\circ\text{C}$; b: $T_g=350^\circ\text{C}$	92
Figure 5-3 AFM images of GaP on Si vs P_2 -exposure temperature ---- P_2 -exposure occurs at the exposure temperatures.....	93
Figure 5-4 AFM images of GaP on Si vs P_2 -exposure temperature P_2 -exposure starts at high temperatures.....	94
Figure 5-5 RHEED patterns of GaP grown on Si a: Electron beam incident perpendicular to steps; b: Electron beam incident parallel to steps. (1): 575°C , one-step growth; (2) 350°C , two-step growth; (3) 350°C , one-step growth.....	95
Figure 5-6 SEM images of anisotropic etching V/III flux: (1) $3\times$; (2) $8\times$. Temperatures: (a) 550°C ; (b) 500°C ; (c) 450°C ; (d) 400°C	97
Figure 5-7 SEM images of anisotropic etching with various prelayers and growth temperatures : mesa parallel to steps; \perp : mesa perpendicular to steps.....	98
Figure 5-8 AFM images of GaP with four nucleation conditions.....	100
Figure 5-9 AFM images of GaP grown under different flux ratios 1: V/III=2.5; 2: V/III=8; a: $T_g=500^\circ\text{C}$; b: $T_g=450^\circ\text{C}$; c: $T_g=400^\circ\text{C}$	101
Figure 5-10 Fabrication process of OP-GaP template on Si substrates.....	104
Figure 5-11 SEM and AFM images of the OP-GaP template structure.....	106
Figure 5-12 Cross-sectional SEM of the OP-GaP template structure.....	107
Figure 6-1 Comparison of low-loss waveguide structures vs. current waveguide structures. a: Current waveguides; b: low corrugation waveguides.....	110
Figure 6-2 Expected SHG conversion efficiency of low-loss waveguides.....	111

INTRODUCTION

Light sources emitting at mid/far-infrared (IR) wavelengths are of a growing interest due to their potential applications in telecommunications, molecular spectroscopy and airborne countermeasures. These applications require mid-IR laser sources with rather demanding attributes, such as wide tunability, narrow linewidth, portability, room-temperature operation and high output power. A type of laser source is emerging that can meet all these needs, that is, laser sources produced by nonlinear optics (NLO).

1. 1 Infrared sources based on nonlinear optics (NLO)

1. 1. 1 *Applications of infrared sources*

In the mid- to far-IR region, a variety of applications exist[1]. One typical application is gas spectroscopy[2,3]. The wavelength region from 2 to 10 μm is favored for spectroscopic detection because it contains the most important fundamental adsorption band of the atmospheric trace gases, such as NO, CF₄, NH₃, and most hydrocarbons. A suitable IR source, tuned to one of the absorption lines of the molecule of interest, provides a sensitive method of determining concentrations by measuring how much light is absorbed by the sample. Such a device would be useful for pollution control and process monitoring. This application requires mid-IR laser sources with both broad tunability and narrow linewidth. It is also desirable to have compact, portable coherent sources with low cost and high output power that can be operated at room temperature for field deployment.

Other applications require very high output power. Typical examples are laser radar systems, remote sensing and airborne countermeasures. These systems could take advantage of the atmospheric windows at 3-5 μm and 8-12 μm and require mid-IR sources with very high output power, but still require portability and room temperature operation. High beam quality, compact size and robustness are also desirable.

1. 1. 2 *Advantages of NLO sources*

No current lasers can provide all the features required for above applications. Solid-state lasers operate over only limited wavelength ranges, typically in the 1-3 μm range. Gas lasers, such as CO₂ (10 μm) and chemical lasers, like HF, also provide laser sources only at specific mid-IR wavelengths. Lead salt diode lasers can access this range but with low output power levels and cryogenic cooling[4]. The quantum cascade lasers have great promise, having demonstrated

emission over much of the mid-IR region, but have limitations on power output, beam quality and frequently require cryogenic cooling[5-6].

On the other hand, near-IR laser diodes and diode-pumped solid-state lasers in the 1.0-2.0 μm wavelength range are not only well-developed, possessing all of these desirable attributes, but have demonstrated good reliability and long lifetime[7]. For this reason, mid-IR generation using nonlinear frequency conversion with these versatile near-IR pumps is a highly appealing strategy for many mid-IR applications. Such sources take advantage of the well developed solid-state laser diodes operating in the near-IR to generate radiation at longer wavelengths.

Current non-linear optical techniques are used with a wide variety of material and wavelength combinations [8]. Figure 1-1 illustrates three examples of the frequency conversion process. One example of the second order nonlinear optical interaction is Second Harmonic Generation (SHG)[9]. The input field at frequency ω , called the pump, generates an output at frequency 2ω . This technique has been used to generate green light (532 nm) from Nd:YAG lasers (1064 nm) and blue (488 nm) from diode lasers (976 nm) as well as testing performances of nonlinear devices.

A second, more complex example, is Difference Frequency Generation (DFG)[10]. Two input beams with frequency of ω_1 and ω_3 , called signal and pump, generate an output at frequency $\omega_2 = \omega_3 - \omega_1$, called idler. So, a pump at short wavelength in the near IR region with a proper signal can generate an idler in the mid- to far- IR region. This is one possible approach to generate intense, coherent beams of mid- to far-IR radiation. An array of such devices could be fabricated in parallel and the idler wave can be tuned over a wide range by scanning across the devices in the array. This type of device would be very useful for spectroscopic applications.

Another example is Optical Parametric Oscillation (OPO)[11]. One input beam at frequency ω_3 , called pump, generates two output frequencies at ω_1 and $\omega_3 - \omega_1$, called signal and idler respectively. Similar to DFG, in the OPO, a pump input in the near IR region can generate radiation in the mid- to far-IR region.

The most important advantage of nonlinear optical sources based on DFG and OPO is that the emission covers the whole wavelength from near to far-IR range with different combinations of pumping sources and nonlinear materials. In general, one single coherent source with broad tuning range up to hundreds of nanometers can be obtained simply by tuning the temperature and pumping wavelength. Under certain special combinations, one single source can generate an output spectrum covering a broad spectral range (4-11 μm)

without any tuning. In addition, nonlinear lasers have a narrow linewidth that mostly depends on the interaction length of the nonlinear materials. Nonlinear-optical sources can operate under different condition, such as high peak power or high average power, pulsed or continuous wave, but are still operated at room temperature. Thus, nonlinear sources meet all of the application requirements and are the best candidate for spectroscopy, airborne countermeasures, remote sensing, and laser radar system[12-15].

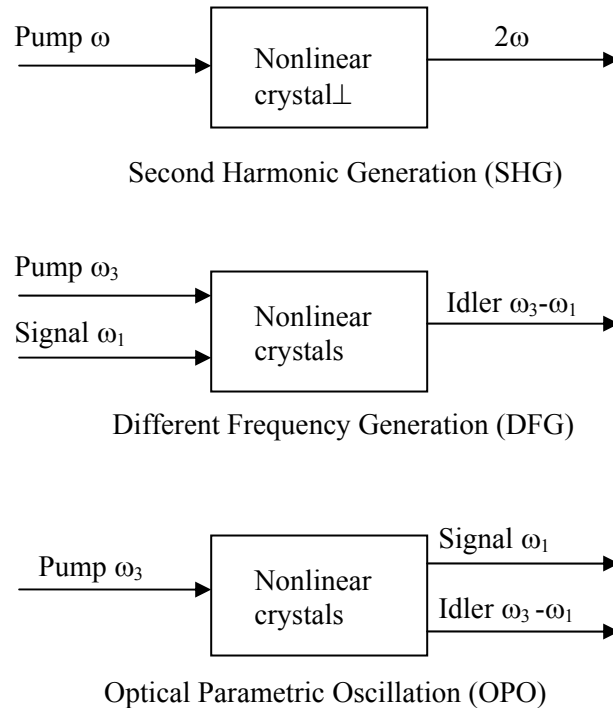


Figure 1-1 Illustrations of frequency conversion

1.2 NLO in optical communications

Another important application of nonlinear optics is for telecommunications, in which nonlinear wavelength conversion is used in wavelength division multiplexed (WDM) networks.

Telecommunications is currently undergoing a large-scale transformation. WDM techniques offer very effective utilization of the fiber bandwidth directly in the wavelength domain, rather than in the time domain. The number of wavelengths in WDM networks determines the number of independent wavelength paths. It is often not large enough to support the large number of nodes in the network. One method of overcoming this limitation is to convert signals from one wavelength to another.

Conventional switching today is achieved in an optical switch with or without signal regeneration. The optoelectronic wavelength conversion technology is mature and readily applicable to field deployment. However, the conversion process from optical to electrical and then back to optical is very slow and requires a lot of expensive laser diodes. It also creates latency or delay which has not been a problem for voice communications, but as the network traffic becomes increasingly digital and connections between computers, wavelength contention and latency are becoming a serious bottleneck.

All-optical frequency conversion provides a much better solution[16-17]. The nonlinear frequency conversion preserves both phase and amplitude information, and this is the only category of wavelength conversion that offers strict transparency. It is also the only method that allows simultaneous conversion of a set of multiple input wavelengths to another set of multiple output wavelengths. This method can potentially accommodate signals with extremely high bit-rates exceeding 100 Gbit/s, with nearly zero latency.

It is worth noting that good conversion efficiency is essential and can only be achieved in waveguide devices. This has already been demonstrated in PPLN-based DFG waveguides. It was also demonstrated by Yoo et al in an AlGaAs-based DFG waveguide, in which, a -6dB DFG conversion efficiency is obtained using a 2-cm-long waveguide and a 100-mW pump.

1.3 Candidate materials for infrared NLO

All these applications require nonlinear optical devices with very high conversion efficiency. In order to successfully implement these non-linear techniques, a suitable material must be found. First, it has to be non-centrosymmetric, since any centrosymmetric material will not have a second-order nonlinear response. Large second-order nonlinear response is desired, since it leads to the most efficient conversion processes. Second, the material must be transparent at all wavelengths of interest including the half wavelength of the high power pump to prevent two-photon absorption. Any attenuation of either input or output beams will seriously decrease the conversion efficiency. Accordingly, a few materials have emerged as choice candidates for different regions of the infrared. One of them is periodically-poled lithium niobate (PPLN)[18]. It has seen widespread use in many applications, from generation of blue-green light at 532 nm, to mid-IR generation and communication devices and commercial products based on lithium niobate LiNbO_3 are available. However, LiNbO_3 is not transparent beyond 4.5 μm , which limits its application in many interesting areas. Thus, other materials have to be developed to cover the mid- to far-IR spectrum.

The most common crystals for mid-IR frequency conversion are the chalcopyrite family,

including ZnGeP₂, AgGaSe₂, AgGaS₂, and CdGeAs₂[19,20], which are usually available in bulk crystals, with centimeter dimensions. Frequency conversion in these materials has already been successfully demonstrated. ZnGeP₂, for instance, has been used to build widely tunable OPOs covering the region from over 3 to 12 μm. However, it suffers from absorption at both short wavelengths (<2 μm) and phonon-related absorption at long wavelengths (>9 μm), as well as point-defect-generated absorption. These are also substantial difficulties in growing large high-quality crystals.

Thus, it is necessary to look for alternate materials that meet all the application requirements. We are interested to find materials with better intrinsic properties (such as high nonlinear coefficients, high thermal conductivity, and low absorption), as well as with mature and convenient materials with known growth and processing techniques. Zinc-blende semiconductors (III-V and II-VI semiconductors) offer all the properties we need[21-27].

Table 1-1 shows the properties of the candidate materials for infrared NLO. As is visible in this table, all three materials (ZnSe, GaAs and GaP) have major advantages over the current materials of choice. For instance, they offer transparency in the mid-IR and larger effective nonlinear coefficients than LiNbO₃. A typical example is GaAs, whose second order nonlinear coefficient is about 5 times higher than LiNbO₃. In addition to their high nonlinear coefficients, they also have much higher thermal conductivity than LiNbO₃ and chalcopyrite materials. Besides their intrinsic properties, these semiconductor materials also benefit from their mature materials growth methods and well-developed processing techniques, with GaAs as a typical example. Because of these properties, the zinc-blende semiconductors have attracted more and more research interest.

Table 1-1 Potential materials used for infrared nonlinear optics

Materials	d_{ij} (pm/V)	Transparency range (μm)	Thermal conductivity (W/m-K)
GaAs	90	1.0- >12	46
GaP	40	0.6-11	110
ZnSe	60	0.5-20	18
ZnGeP₂	70	2.0- >9.0	35
AgGaSe₂	33	0.8-18	1
LiNbO₃	35	0.5-4.5	7.6

Nonlinear optical devices based on GaAs have been fabricated by various research groups. They demonstrated almost all the different forms of nonlinear optical generation process, such as SHG, DFG, OPO, etc[28-33]. High conversion efficiency and high damage threshold have been demonstrated. However, due to its optical isotropy, conventional birefringent phasematching is not possible with GaAs, but instead, quasi-phasematching is required. An orientation-patterning approach has to be used. At the outset of this research, a few problems still need to be solved in order to fabricate highly performing waveguides out of this structure, which are mostly related with materials growth.

Compared with GaAs, ZnSe and GaP are less developed. ZnSe offers the widest transparency range and allows pumping at very short wavelengths that are commonly available, where GaAs suffers from two-photon absorption. However, the research on ZnSe is still at the stage of material development, such as obtaining epitaxial ZnSe growth on orientation-patterned GaAs templates.

The nonlinear coefficient of GaP is less than GaAs and ZnSe, but it has much higher thermal conductivity and a wider transparency range. It is a desirable material for nonlinear optical devices with high power operation and high pump power. Compared with ZnSe, GaP has more mature epitaxial growth techniques, and it is another highly promising material system.

1.4 Dissertation overview

This dissertation will be organized as follows: In Chapter 2, we introduce the theories of frequency conversion and point out the phasematching requirement for the nonlinear generation process and the phasematching approaches in III-V materials. In Chapter 3, we investigate the growth mechanisms and growth techniques of GaAs on Ge and minimize the template corrugations that limit our device performance. In Chapter 4, we describe the growth conditions and fabrication process for low-corrugation nonlinear waveguides and carry out optical characterization. In Chapter 5, we study the growth of single-phase GaP, which leads to the fabrication of orientation-patterned GaP (OP-GaP) templates. In Chapter 6, we provide a summary of this dissertation and introduce possible devices and structures that will lead better performance and wider applicability in the future.

Chapter 2 PHASEMATCHING IN SEMICONDUCTORS

In this chapter, we introduce the theoretical background necessary to understand the results presented in the rest of this dissertation; details of relevant nonlinear optical theories have been covered in literatures[34-37]. We will focus on second-order nonlinear interactions, which are the types of interactions we are testing in this dissertation work. The techniques to obtain III-V nonlinear optical devices are introduced, which are the focus of this dissertation.

2.1 Theory of frequency conversion

Before the invention of lasers, it was usually assumed that the polarization induced in a material is proportional to the exciting electric field. Since the invention of lasers, the nonlinear response of a material under an intense electric field has attracted much research interest. Thus, higher order terms appear in the polarization equation as shown in Equation 2.1. Equation 2.1 shows the induced polarization in a medium, written as a Taylor series expansion:

$$P_i = \sum_j \epsilon_0 \chi_{ij}^{(1)} E_j + \sum_{j,k} \epsilon_0 \chi_{ijk}^{(2)} E_j E_k + \sum_{j,k,l} \epsilon_0 \chi_{ijkl}^{(3)} E_j E_k E_l \dots \quad 2.1$$

where P_i is i -th Cartesian component of the induced polarization, $\chi^{(2)}$ (or $\chi^{(3)}$) are the 2nd (or 3rd) order non-linear optical susceptibilities, and E_i is the i -th component of the electric field. In this equation, the first term is responsible for the linear response while the higher order terms are responsible for generation of various frequencies. In general, the E_j and E_k can have different frequencies, so that the higher order terms of the polarization contain various combinatorial frequencies. For example, if only 2nd order effects are considered, in which we are mostly interested, the input light has two frequencies ω_1 and ω_2 , the polarization will contain multiple frequencies, including $2\omega_1$, $2\omega_2$, $\omega_1 + \omega_2$ and $\omega_1 - \omega_2$. This polarization will act as an electromagnetic radiation source at those frequencies, and thus the material emits at those frequencies. The light generation process of $2\omega_1$ and $2\omega_2$ are SHG, generation of $\omega_1 + \omega_2$ is sum frequency generation (SFG), and generation of $\omega_1 - \omega_2$ is DFG.

From the physical point of view, non-linear interactions can be explained considering the material as a collection of harmonic oscillators. At low applied fields, electrons oscillate at the

applied frequency in a potential that can be approximated by a parabola. At intense fields the parabolic approximation is no longer valid and more terms need to be added to the potential. Thus non-linear effects occur and components at higher harmonics appear. If more than one frequency is applied, mixing of these frequencies will result in polarization components at sum/difference-frequencies. Obtaining these new frequencies is usually the goal of non-linear optics.

2. 1. 1 Coupled equations

The nonlinear optical generation processes can be described by a series of coupling equations. The derivation begins with the plane wave equation in a material. A plane wave propagating in a dielectric isotropic media can be derived from Maxwell's equations as follows:

$$\nabla^2 \vec{E} - \vec{\nabla}(\vec{\nabla} \cdot \vec{E}) \frac{1}{c^2} \frac{\partial^2 \vec{E}}{\partial t^2} = \mu_0 \frac{\partial^2 \vec{P}}{\partial t^2} \quad 2.2$$

where E is the electric field, c is the light speed in the media, and P is the total polarization defined in Equation 2.1. By splitting the linear and higher order polarization terms, the nonlinear wave equations can be described as:

$$\nabla^2 \vec{E} - \frac{\epsilon_0}{c^2} \frac{\partial^2 \vec{E}}{\partial t^2} = \mu_0 \frac{\partial^2 \vec{P}_{NL}}{\partial t^2} \quad 2.3$$

This is a partial differential equation of electrical field and polarization in the media. Let us assume that the light is propagation along the z direction, and the electric field is a superposition of three waves with different frequencies. The Fourier amplitude at frequency ω_n can be written as

$$E_n(z) = E_n \exp(-ik_n z) \quad 2.4$$

where k_n is the wave vector and E_n is the amplitude.

Assuming the amplitude varies slowly, and the coupled equation becomes

$$\frac{dE_n}{dz} = i \frac{\omega_n^2 \mu_0}{2k_n} P_{NL} \exp(ik_n z) \quad 2.5$$

We will consider only the 2nd order terms, and from Equation 2.1, the 2nd order polarization is simplified as

$$P_{NL}(\omega_i) = 2\epsilon_0 d_{eff} E_j E_k \quad 2.6$$

here, d_{eff} (usually called as nonlinear coefficient) is the effective nonlinear susceptibility after

considering the crystal symmetry and it is commonly used to substitute for $\chi_{ijk}^{(2)}$.

Combining Equation 2.5 and 2.6, we can derive a series of coupled equations for three waves.

$$\begin{aligned}\frac{dE_1}{dz} &= i \frac{\omega_1 d_{eff}}{n_1 c} E_3 E_2^* \exp(-i\Delta k z) \\ \frac{dE_2}{dz} &= i \frac{\omega_2 d_{eff}}{n_2 c} E_3 E_1^* \exp(-i\Delta k z) \\ \frac{dE_3}{dz} &= i \frac{\omega_3 d_{eff}}{n_3 c} E_1 E_2 \exp(i\Delta k z)\end{aligned}\tag{2.7}$$

where the wave vector mismatch is defined as

$$\Delta k = 2k_3 - (k_2 + k_1) = 2\pi \left(\frac{n_3}{\lambda_3} - \frac{n_2}{\lambda_2} - \frac{n_1}{\lambda_1} \right)\tag{2.8}$$

and the n_i is the refractive index at frequency ω_i , λ_i is the free space wavelength and E_i^* is the complex conjugate of E_i .

It is clear from the coupled equations, the derivative of the electrical field will oscillate in phase with z if Δk is not zero. The amplitude change at the output wave is achieved by integration of the coupled equations, and the change is negligible if Δk is not zero, which indicates that no nonlinear conversion occurs.

Thus, to achieve high nonlinear optical conversion efficiency, Δk has to be compensated using some approach associated with the nonlinear material.

2. 1. 2 Conversion efficiency

From the coupled equation, we can derive the nonlinear conversion efficiency. Take SHG as a simple example, the coupled equations can be expressed as one simple equation:

$$\frac{dE_{2\omega}}{dz} = i \frac{2\omega d_{eff}}{n_{2\omega} c} E_{\omega}^2 \exp(-i\Delta k z)\tag{2.9}$$

By integrating both sides of Equation 2.9, we can obtain the intensity of the SH wave expressed as a function of the intensity of the fundamental wave as,

$$I_{2\omega} = \frac{32\pi^2 d_{eff}^2}{n_{2\omega} n_{\omega}^2 c \lambda_{\omega}^2} I_{\omega}^2 \text{sinc}^2 \left[\frac{\Delta k L}{2} \right] L^2\tag{2.10}$$

where sinc^2 is obtained after integration of the exponential term; L is the sample length,

$I_{2\omega}$ the intensity of SH wave, I_{ω} the intensity of fundamental wave, $n_{2\omega}$ and n_{ω} are the refractive indices, and λ_{ω} the fundamental wavelength.

This derivation is based upon the plane-wave approximation. In a real case, the spatial overlap of the polarization of the interacting waves must be taken into account to calculate the conversion efficiency.

In bulk devices with loosely focused beams, we can take the interacting fields to be Gaussian beams, the interacting waves are Gaussian beams characterized by an effective beam size as

$$A_i = \frac{\pi w_i^2}{2}$$

where w_i is the beam waist of Gaussian beam. The power is expressed as $P_i = I_i A_i$. Thus, the spatial overlap can be obtained by the spatial integration of the interacting electrical field, and we obtain the power at SH wavelength as

$$P_{2\omega} = \eta_{norm} P_{\omega}^2 L^2 \text{sinc}^2 \left[\frac{\Delta k L}{2} \right] \quad 2.11$$

where η is the normalized SHG conversion efficiency with the unit of Watts/cm², and it can be expressed as

$$\eta_{norm} = \frac{32\pi^2 d_{eff}^2}{n_{2\omega} n_{\omega}^2 c \lambda_{\omega}^2} \frac{1}{A_{eff}} \quad 2.12$$

where A_{eff} is the effective interacting area, and is $\frac{\pi (w_{\omega}^2 + w_{2\omega}^2)}{2}$.

The normalized conversion efficiency gives a good comparison for different devices if the losses are ignored, and the absolute conversion efficiency $\eta = \frac{P_{2\omega}}{P_{\omega}^2}$ is proportional to the square of the sample length.

As expressed in Equations 2.11 and 2.12, the conversion efficiency is governed by several factors. The first is the effective nonlinear susceptibility. Definitely higher nonlinear susceptibility produces higher conversion efficiency. Thus, the search for materials with high nonlinear susceptibility is really important.

The second factor is the phase matching condition, as expressed in the sinc^2 function. If

the phases of interacting waves are not matched and Δk is not zero, the term $\text{sinc}^2\left[\frac{\Delta k L}{2}\right]$ is oscillating between zero and local maximum value and approaches zero when L is large. Thus, the absolute conversion efficiency is very small though the normalized conversion efficiency can be very high. To obtain any useful conversion efficiency, the phasematching problem MUST be solved.

The third factor is the effective interacting area. If the light intensity is tightly confined, the effective interacting area can be very small, and much higher conversion efficiency can be obtained. In bulk materials, diffraction limits the useful focusing to looser than the "confocal condition", for which the diffraction length of the Gaussian beam equals the length of the crystal and the overlap area is large. As shown in Figure 2-1, the beam waist (the smallest beam size) is much larger than the mode dimension that can be achieved in waveguides. In addition, due to diffraction, the light is only focused at a very specific location and a larger beam size occurs along the beam propagation path. The overlap intensity between the interacting waves is thus much smaller [38].

In waveguide devices, as shown in Figure 2-1, the electric field is confined in the waveguide core and the effective beam size can be estimated by the mode size. The effective interaction area is calculated as

$$A_{eff} = \left| \iint \tilde{E}_\omega^2(x, y) \tilde{E}_{2\omega}^*(x, y) dx dy \right|^{-2} \quad 2.13$$

where the modal fields are normalized to carry unit power. This effective area is much smaller than can be obtained in interactions in bulk materials. Thus, waveguide devices are potentially able to provide much higher conversion efficiency. For example, the conversion efficiency of a LiNbO₃ waveguide can be as high as 1000%/W, while the conversion efficiency in bulk devices is well below 100%/W.

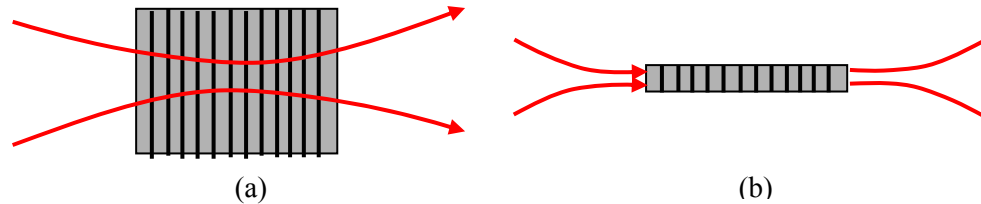


Figure 2-1 Mode confinement in (a) bulk devices (b) waveguides

The fourth factor is the sample length. Under phasematching conditions and a zero-loss

assumption, the conversion efficiency increases quadratically with sample length. Thus, extraordinarily high conversion efficiency is possible with very long devices.

2. 1. 3 Effect of propagation loss

Unfortunately, material or waveguide losses have a great impact on the conversion efficiency. Minimal loss is crucial for high nonlinear optical conversion efficiency. Again, we take an example of the SHG case. Without loss, the SHG power can be derived based on the coupled equations and the power increases quadratically with the crystal length as expressed by Equation 2.11. If we assume attenuation at both wavelengths, we can find the efficiency reduction due to losses at the phase matching condition, as characterized by a revised coupled equation.

$$\frac{dE_{2\omega}}{dz} + \alpha_{2\omega} E_{2\omega} = i \frac{2\omega d_{eff}}{n_{2\omega} c} E_{\omega}^2 \exp(-i\Delta k z) \quad 2.14$$

where $E_{\omega} = E_{\omega}(0) \exp(-\alpha_{\omega} z)$, α_{ω} is the loss at the fundamental wavelength, and $\alpha_{2\omega}$ is the loss at the SH wavelength.

By solving equation 2.14, we obtain a solution as,

$$E_{2\omega} = i \frac{2\omega d_{eff}}{n_{2\omega} c} E_{\omega}^2 \frac{e^{(i\Delta k - 2\alpha_{\omega})z} - e^{-\alpha_{2\omega}z}}{i\Delta k - (2\alpha_{\omega} - \alpha_{2\omega})} \quad 2.15$$

Assuming the phase matching condition, where $\Delta k = 0$, we obtain

$$\frac{P_{2\omega-loss}}{P_{2\omega-lossless}} = \left(\frac{e^{-\alpha_{\omega}L} - e^{-\alpha_{2\omega}L/2}}{\alpha_{\omega}L - \alpha_{2\omega}L/2} \right)^2 \quad 2.16$$

Equation 2.16 shows that the SH power under loss is dramatically reduced compared with the lossless conditions because the losses appear in exponential terms.

We can plot the power under three conditions in one graph as shown in Figure 2-2. In the lossless case, the power keeps growing without limit. If there is a loss at one wavelength, the power will saturate at one level and will not increase any further. If there are losses at both wavelengths, the power reaches a maximum at a certain length and decreases thereafter.

In our previous work, huge losses existed in the nonlinear AlGaAs waveguide devices, greater than 40 dB/cm at 1550 nm and even higher at the second harmonic wavelength. Thus, the conversion efficiency was very low, severely limiting the application of AlGaAs nonlinear waveguides.

The loss in bulk materials is relatively small, thus very long device length can be used.

While the losses are lower, the normalized conversion efficiency is not as high as waveguide devices because of the magnitude of the electric field and dispersion. In waveguide devices, the loss is generally high, especially for AlGaAs/GaAs nonlinear waveguides. With high losses at both wavelengths, the maximum SHG power can only be achieved with relatively short optimal sample length. In previous work of AlGaAs/GaAs nonlinear waveguides, the optimal device length was around 2 mm. In chapter 4, the fabrication of low-loss waveguides will be introduced which dramatically increases the conversion efficiency.

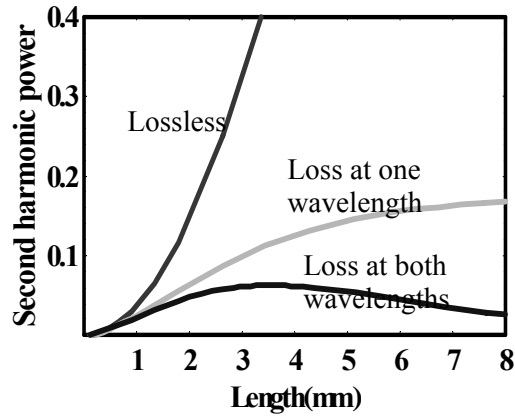


Figure 2-2 SHG power in a function of length with various losses

2. 2 Phase matching approaches

As mentioned above, phasematching has to be fulfilled for the nonlinear generation process to be useful. Equation 2.9 already illustrates the critical effect of phasematching. According to this equation, the interacting waves are required to be in phase so that the newly generated electric field will always constructively superpose with the previously generated electric fields; otherwise, the interacting waves walk out of phase and the newly generated field will cancel previously generated fields.

The phase matching condition is expressed by Equation 2.8, and simplified as equation 2.17 for SHG process.

$$\Delta k = k_{2\omega} - 2k_{\omega} = \frac{2\pi}{\lambda_{\omega}}(n_{2\omega} - n_{\omega}) \quad 2.17$$

The coherence length is thus defined as $L_c = \frac{\pi}{\Delta k}$, after which, the interacting waves will walk out of phase. The SHG power as a function of the interacting length under various phasematching conditions is plotted in Figure 2-3. When $\Delta k = 0$, as in this case, the

interaction is said to be phasematched, the sinc^2 term in Equation 2.10 is equal to 1 and the conversion efficiency is maximum. In addition, the non-linear output power increases quadratically with the interaction length.

However, due to the dispersion in a real material, if no particular care is taken, we will still have $\Delta k \neq 0$ under most of the conditions. The interaction is then called non-phasematched and the non-linear power depends sinusoidally on the length of interaction length L . From the physical point of view, the two waves are traveling at different speeds because of the material dispersion, and accumulate a difference of phase. After one coherence length, the power starts to flow from the SHG wave back to the fundamental wave, resulting in oscillatory behavior.

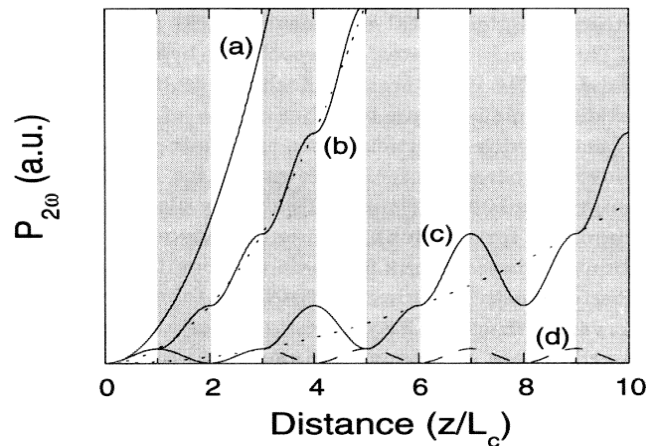


Figure 2-3 Second harmonic output power in function of distance
(a) ideal phasematching; (b) first order quasi-phasematching;
(c) higher-order quasi-phasematching; (d) non-phasematched

Particular care has to be taken to meet the phasematching condition. In materials with optical birefringence, the phase matching is met by aligning the polarization direction of the fundamental wave and SH wave along different optical axes. As shown in Figure 2-4, the polarization of the SH wave ($\lambda/2$) is along the ordinary optical axis, while the polarization of the fundamental wave (λ) is along the extraordinary optical axis. Under certain conditions, the refractive indices for the interacting waves are identical. This phasematching condition is called birefringent phasematching.

Unfortunately a few drawbacks come along with this solution: birefringent walk-off between the pump and signal beams can occur when the Poynting vector \mathbf{S} and the propagation vector \mathbf{k} are not parallel, thus reducing the efficiency. Many materials are not

birefringent (such as GaAs) or the 2nd order susceptibility $\chi_{ijk}^{(2)}$ may not allow efficient conversion with the polarizations involved.

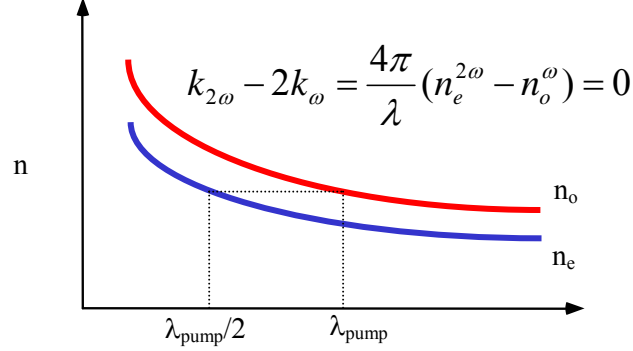


Figure 2-4 Birefringent phasematching

In order to utilize these materials, another solution is used, known as quasi-phasematching (QPM). As shown in Figure 2-3(b), after each coherence length, the power will start flow back into the fundamental wave. If we can reverse the power flow direction by adding a π -phase between the second-harmonic wave and the nonlinear polarization, the power will continue flowing into the SH wave. Thus the power will continue increasing quasi-quadratically with the nonlinear interaction length and high output power is possible.

This condition can be achieved by fabricating crystals with the structure shown as Figure 2-5, where the domains are periodically switched after each coherence length. The adjacent domains have opposite sign of 2nd order susceptibility or d_{eff} , which is shown by the “+” or “-” signs. The domain periods or QPM periods are twice the coherence lengths. If the sign of 2nd order susceptibility is switched every three coherence lengths, the power increases more slowly because the power will still oscillate between interacting waves within every $\frac{1}{2}$ -periods. It is obvious that the switching the sign of the nonlinear coefficient every odd times of coherence length is required for QPM, otherwise, the power will completely flow back to the pumping waves at the end of every $\frac{1}{2}$ -period.

The effective 2nd order nonlinear coefficient of the QPM structure can be expressed as

$$d_{eff}(z) = d_{max} \sum_m \frac{2}{\pi m} \sin\left(\frac{2\pi m z}{\Lambda_g}\right) \quad 2.17$$

Substitute 2.17 into the coupled equation 2.9, and integrate over z , we can obtain,

$$E_{2\omega}(z=L) = \sum_m \left(\frac{i\omega d_{QPM}^m}{n_{2\omega} c} \right) E_{\omega}^2 L \operatorname{sinc} \left(\frac{(\Delta k - K_m)L}{2} \right) \quad 2.18$$

where $K_m = 2\pi m / \Lambda_g$ and $d_{QPM}^m = 2d_{eff} / \pi m$. If $\Delta k - K_m = 0$ (m is an odd integer), only the m^{th} term in Equation 2.18 is non-zero at large L , thus the SH power becomes

$$P_{2\omega} = \left(\frac{2\omega d_{\max}}{n_{2\omega} c \pi m} \right)^2 \frac{P_{\omega}^2 L^2}{A_{\text{eff}}} \operatorname{sinc}^2 \left(\frac{(\Delta k - K_m)L}{2} \right) \quad 2.19$$

where $\operatorname{sinc}^2 \left(\frac{(\Delta k - K_m)L}{2} \right) = 1$ and $\Lambda_g = 2m \frac{\pi}{\Delta k} = 2mL_c = \frac{m\lambda_{\omega}}{2(n_{2\omega} - n_{\omega})}$.

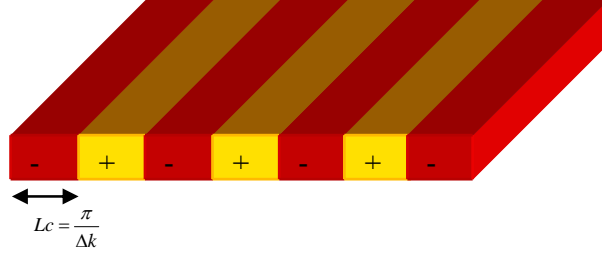


Figure 2-5 Materials structure for QPM

Compared with the ideal phasematching conditions, the SHG power obtained in this QPM approach is reduced by a factor of $\frac{4}{\pi^2 m^2}$. Obviously $m=1$ is preferred, since in this case the sign of the non-linear coefficient is changed every coherence length and the output power continues to increase quadratically, whereas for $m>1$ the field undergoes some oscillatory behavior and the power increases slowly. However, $m=1$ implies a very short modulation period or QPM period ($\Lambda_g = \frac{\lambda_{\omega}}{2(n_{2\omega} - n_{\omega})}$), especially at short wavelengths. This is usually difficult to obtain in materials with a QPM structure used for short wavelength generation.

QPM has been successfully used to fabricate nonlinear devices, with periodically-poled lithium niobate (PPLN) [14-15] as a typical example, which has been extensively investigated and now employed in many applications.

2.3 Phasematching in III-V semiconductors

As described in the previous chapter, semiconductors with the zinc-blende structure have very high nonlinear efficiency, much higher than that of LiNbO_3 . In addition, their mature process technology, well-developed material growth techniques and integration with active sources make them far more desirable for nonlinear optics. Unfortunately, they are optically isotropic, i.e., no birefringence phasematching is available. Thus various phasematching techniques must be used, such as QPM in bulk materials, and form-birefringence phasematching (BPM) or modal phasematching (MPM) in waveguides. In this section, we review these phasematching methods in semiconductor materials, mostly focused on how to fabricate material with artificial structures to achieve quasi-phasematching.

2.3.1 BPM nonlinear waveguides

Compared with nonlinear optical devices fabricated on bulk materials, in which only the QPM approach can be used to obtain phasematching, more versatile phasematching approaches can be used in waveguide devices. A typical example is form-birefringence[39-43]. As shown in Figure 2-6, the waveguide core is composed by GaAs/ AlO_x multi-layers which break the crystal symmetry. The guided mode has an effective refractive index depending on the polarization direction of the electrical field, thus the transverse electric field (TE) mode and transverse magnetic field (TM) mode have different dispersion relationships, as shown in figure 2-6(b). Phasematching can be achieved by aligning the polarizations of pump wave and signal wave along different directions. The index difference between two modes must be large enough for phasematching specific nonlinear generation process. Thus a large index contrast of the adjacent layers in multi-layers is required to cause a large asymmetry along the wafer normal direction. Thus, AlO_x is used in the multi-layers, which has a refractive index close to 1.7, far from that of GaAs (~3.3).

However, nonlinear waveguide devices fabricated based on this method have low-conversion efficiency, largely because of the high waveguide loss at short wavelengths. The absorption length is estimated to be a few tens of microns at 0.8- μm wavelength. This is possibly attributed to absorption of the deep levels formed during the oxidation process, in which, AlAs in AlAs/GaAs multi-layers is oxidized to obtain AlO_x/GaAs multi-layers. The oxidation process potentially produces excess As which incorporates into the lattice of GaAs as anti-site defects.

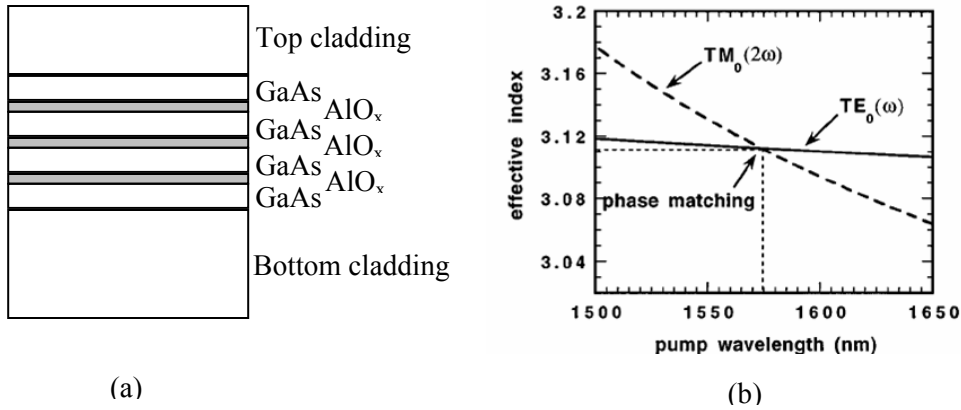


Figure 2-6 Form birefringence phasematching in GaAs nonlinear waveguides

2.3.2 MPM nonlinear waveguides

Another approach is to phase-match the 1st or 2nd order guided mode at the fundamental wavelength with higher order guided modes at the SH wavelength. However, the overlap between those two modes is low and a special waveguide structure has to be designed to maximize the overlap[44,45]. As shown in Figure 2-7, an M-type of waveguide is fabricated to maximize the overlap between the TE_2 mode (3rd order) at the SH frequency and the TM_0 or TE_0 mode at the fundamental frequency. Unfortunately, the overlap efficiency is still not as high as phasematching the 1st or 2nd guided mode (TE_0 and TM_0) and it is inherently inefficient. In addition, high losses are also observed in these kind of waveguides, and no practical improvement has ever been achieved using this approaches. BPM waveguides or QPM waveguides (to be described later in this dissertation work) have obvious advantages over MPM waveguide.

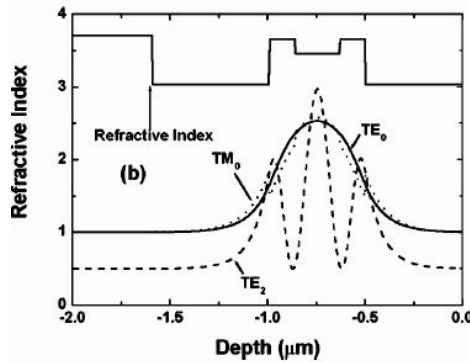


Figure 2-7 MPM phasematching techniques in GaAs/AlGaAs waveguides

2. 3. 3 QPM in III-V materials

There are a several approaches to create QPM in AlGaAs or GaAs waveguides. One type of QPM is obtained by modulating the magnitude instead of the sign of the nonlinear coefficient. The final structure is similar as Figure 2-5, and the 2nd order effective nonlinear coefficient can be expressed as

$$d_{eff}(z) = \frac{d_1 + d_2}{2} + \frac{d_1 - d_2}{2} \sum_m \frac{2}{\pi m} \sin\left(\frac{2\pi m z}{\Lambda_g}\right) \quad 2.20$$

The first term cannot contribute to quasi-phasematched nonlinear generation. Thus, the SH conversion efficiency is determined only by the 2nd term, and the effective nonlinear coefficient for the mth-order QPM is $d_{QPM}^m = (d_1 - d_2) / \pi m$. It is obvious that only modulating the value is much less efficient than modulating the sign of nonlinear conversion efficiency.

One approach to modulate the value of the nonlinear coefficient by ion-implantation assisted quantum well intermixing after the asymmetric quantum well growth[46,47]. However, the modulation magnitude is small and the ion-beam implantation induces a high concentration of defects, leading to high optical loss. Another approach is to use the patterned regrowth, in which the GaAs is patterned and etched after growth and then the AlGaAs is regrown on the etched region[48]. However, the QPM domains are composed of different materials with different refractive indexes. Fresnel reflection at each domain boundaries causes huge losses. In addition, the magnitude of the nonlinear coefficient for AlGaAs and GaAs is not very different and low high effective nonlinear coefficient can be expected.

In this sense, only the QPM structure with modulation of the sign of the nonlinear coefficient is a promising approach for high conversion efficiency. Two approaches are used to fabricate this type of QPM structure. The first one was a wafer bonded technique[49], and the second utilizes regrowth on an orientation-patterned template[50-57]. The first approach can only be used for fabricating bulk nonlinear optical devices with very high power because the period is dictated by the wafer thickness. The second approach can be used for both waveguide devices and bulk devices because the period is dictated by lithography and epitaxy. Both approaches are using the fact that sign of 2nd order susceptibility will change the sign after a 90° rotation about <001> axis because of the $\bar{F}43m$ symmetry of zinc-blende structure. As shown in Figure 2-8, the rotation of GaAs about [001] with 90° is equivalent to that of the Ga and As atoms exchanging their sublattice location, or inverting the As-Ga bonds. It is convenient to name them with phase+ and phase- following the reference

convention (they are indeed exactly the same phase, just with different orientations). The sign of the 2nd order nonlinear coefficient is of opposite for these two phases.

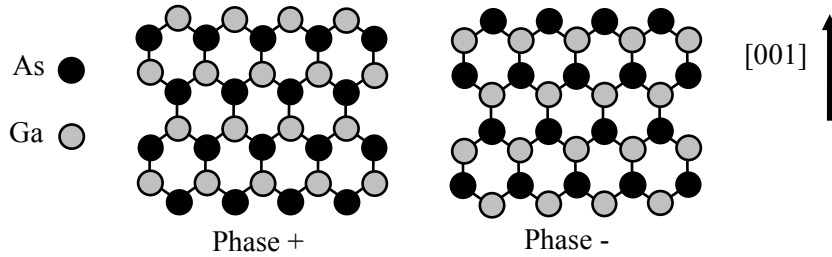


Figure 2-8 GaAs structure with rotation about [001] axis by 90°

2. 3. 3. 1 Wafer-bonded stacks

Figure 2-9 illustrates the fabrication process of QPM structure by bonding a series of GaAs wafers. Every two adjacent wafers have a 90° rotation about [001] axis (or along the normal of wafers). Practical devices have been fabricated using this technique. Using such structures, our group at Stanford and another group at Thomson-CSF were able to demonstrate SHG, DFG, and even an OPO[49]. However, the devices based on this approach are too lossy. In addition, the thickness of plates cannot be thin enough for the nonlinear generation at short wavelengths, and stacking too many plates together is extremely difficult, thus the device length is not long enough to obtain high conversion efficiency.

If the interfacial quality is acceptable the bonded wafer stacks can be used for THz generation with short wavelength pumping, since the QPM period is typically hundreds of microns and long devices can be fabricated without stacking too many wafers. For shorter wavelength IR applications, this is not a convenient approach.

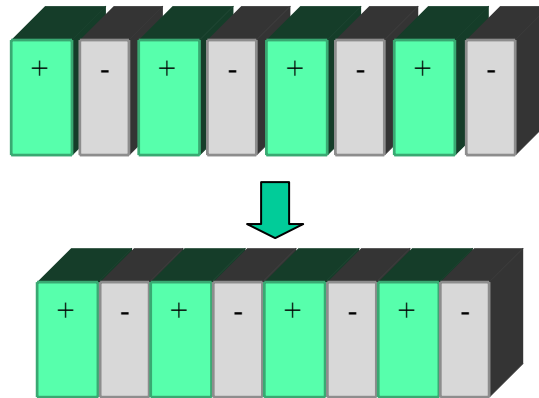


Figure 2-9 QPM structure by wafer bonding

2. 3. 3. 2 Orientation-patterned template

A far better solution to fabricate QPM GaAs structures is to grow orientation-patterned GaAs (OP-GaAs) materials. Figure 2-10 illustrates the fabrication process. The left image of Figure 2-10 shows the orientation-patterned template, where, the surfaces of GaAs with two orientations are exposed alternatively by etching through the top GaAs layer. A thick GaAs layer is epitaxially grown on the template and both domains grow vertically, forming a QPM structure. This approach enables very small QPM periods (10-100 times smaller than the wafer-bonded approach), and the periods are precisely controlled by lithography. Obviously this approach provides a flexibility to fabricate nonlinear devices for wavelength generation over the entire transparency region. In addition, the active device region is epitaxially grown, thus the domain boundary quality is free from contamination. In the ideal case, light scattering at the domain boundaries is negligible if the regrowth conditions are optimized to obtain high quality domain boundaries.

Two approaches have been used to obtain OP-GaAs templates. The first one was to use wafer-bonded technique[50], in which two wafers have a 90° rotation with respect to each other and are bonded together. In one wafer, the substrate is thinned, leaving a thin GaAs epi-layer which has an opposite orientation compared to the other wafer. In the end, the remaining GaAs epi-layer is patterned and etched to expose the surface of GaAs with alternate orientations. Frequency conversion in waveguides has been demonstrated using this approach. The most successful result was obtained by Yoo, et al [50]. They demonstrated previously the highest SHG conversion efficiency in AlGaAs nonlinear waveguides, and they also demonstrated DFG in similar waveguide devices.

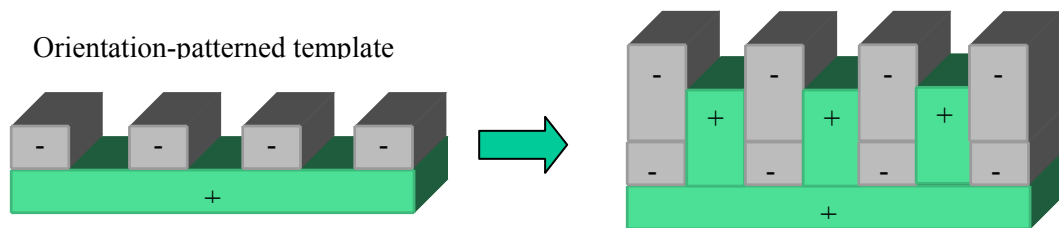


Figure 2-10 QPM structure by regrowth on orientation-patterned template

However, the remaining GaAs epi-layer thickness is very large and the quality of the interface between the bonded wafers is not satisfactory. Both factors add up to the regrowth difficulties and lead to poor regrowth quality and high waveguide loss.

This second approach to fabricate OP-GaAs templates was invented independently by our

group at Stanford University and by a group at the University of Tokyo, that has all-epitaxial OP-GaAs templates[51-57]. The essence of this approach is to utilize the properties of polaron-nonpolar growth, obtaining inverted-GaAs/Ge/GaAs heterostructures rather than bonding two GaAs plates together. This approach is by far the best solution to fabricate GaAs QPM structures. Frequency conversion has been successfully demonstrated with devices fabricated via this approach, including SHG, DFG, OPO, etc. which are described later in this dissertation.

2. 4 Goal of this dissertation work

Although all-epitaxially fabricated OP-GaAs templates have been successfully demonstrated, many issues still remain. First, the quality of the domain boundaries is not good enough, particularly for short QPM periods. This obviously limits the application of nonlinear optical generation at short wavelengths. Second, a high template corrugation existed in our previous template structures, which lead to intense light scattering and reduces the nonlinear conversion efficiency, particularly for waveguide devices. More importantly, the waveguide devices based on this approach were extremely lossy, and the conversion efficiency was very small, and was far from our expectation. We must improve the MBE growth conditions and study the fundamental growth mechanisms in order to fabricate practical nonlinear waveguide devices with high conversion efficiency.

Thus, our first goal was to improve the previous materials growth techniques and device fabrication process in order to obtain AlGaAs/GaAs nonlinear optical waveguide devices with low propagation loss and high conversion efficiency.

In this sense, we will study the growth mechanisms of GaAs/Ge/GaAs and investigate the optimal growth conditions to obtain high quality OP-GaAs templates, which is focused on antiphase-free GaAs growth on Ge. We will also investigate the regrowth on the orientation-patterned substrates and study the particular material growth phenomenon. We find the growth techniques to obtain high domain-boundary quality, especially for nonlinear waveguide devices with a narrow QPM period and eventually demonstrate high conversion efficiency in waveguide devices.

Our second goal is to develop OP-GaP templates for high power nonlinear devices. We studied the growth conditions of single-phase GaP on Si and investigated the fabrication techniques of OP-GaP templates. Hopefully we can transfer all the knowledge we obtained from OP-GaAs growth to OP-GaP growth.

Chapter 3 ALL-EPITAXIAL ORIENTATION-PATTERNED GaAs TEMPLATE

After describing the concepts for quasi-phase-matching (QPM) in semiconductors and orientation-patterned III-V structures in the previous chapter, we now describe the details of the fabrication process in this chapter. We start with a brief introduction to the orientation inversion process of OP-GaAs and then describe the growth conditions leading to the inverted-GaAs/Ge/GaAs. Next we introduce the concept of template corrugation and investigate the growth conditions that minimize the template corrugation, which is important for waveguides. Since all the materials are grown by molecular beam epitaxy (MBE), I first describe the MBE machine and the necessary characterization tools used during and following the growth.

3.1 Molecular beam epitaxy

Epitaxial growth is a process in which layers of materials are deposited on a substrate while conserving the substrate's crystalline structure. The development of epitaxial techniques, in semiconductors in particular, has been one of the most important advancements for the advancement of electronics and optoelectronics. While there exist many types of epitaxial growth techniques for III-V semiconductors, ranging from liquid-phase epitaxy (LPE) to vapor-phase such as metal-organic vapor-phase epitaxy (MOVPE) and hydride vapor-phase epitaxy (HVPE), we have utilized molecular beam epitaxy (MBE), mostly because it is the epitaxial technique which is farthest from thermal equilibrium and allows the greatest range of growth conditions. MBE is a process for growing thin epitaxial films of a wide variety of materials, ranging from oxides to semiconductors to metals[58]. It was first applied to the growth of compound semiconductors. In this process beams of atoms or molecules in an ultra-high vacuum environment are incident upon a heated substrate crystal that has previously been processed to produce a nearly atomically clean surface. The arriving constituent atoms form a crystalline layer in registry with the substrate, i.e., an epitaxial film. Because of the non-equilibrium growth conditions, the composition can be rapidly changed, producing crystalline interfaces that are almost atomically abrupt. Thus, it has been possible to produce a large range of unique structures by MBE, including quantum well devices, superlattices, lasers, etc., all of which benefit from the precise control of composition and preservation of interfaces during growth. Because of the cleanliness of the growth environment and because of the

precise control over composition, MBE structures very closely approximate the idealized models used in early treatments (before computers) of solid state theory.

Figure 3-1 shows a schematic top view of a basic MBE growth chamber. The main component of an MBE system is an Ultra-High Vacuum (UHV) chamber, where background pressure can be as low as 10^{-11} torr. This chamber is pumped down to such low pressures by using multiple vacuum pumps, including a cryo pump, an ion pump, and cryo-shrouds filled with liquid nitrogen. In addition, the source ovens and the substrates are surrounded by the chilled walls, thus, the beams make essentially a single pass through the chamber before hitting the substrate or condensing on the cold chamber walls. This preserves the purity of the growing film and eliminates any memory effect of what was previously grown. A thin, crystalline substrate wafer is mounted on a heater such that it can be brought to face the source ovens used to evaporate the constituent atoms or molecules.

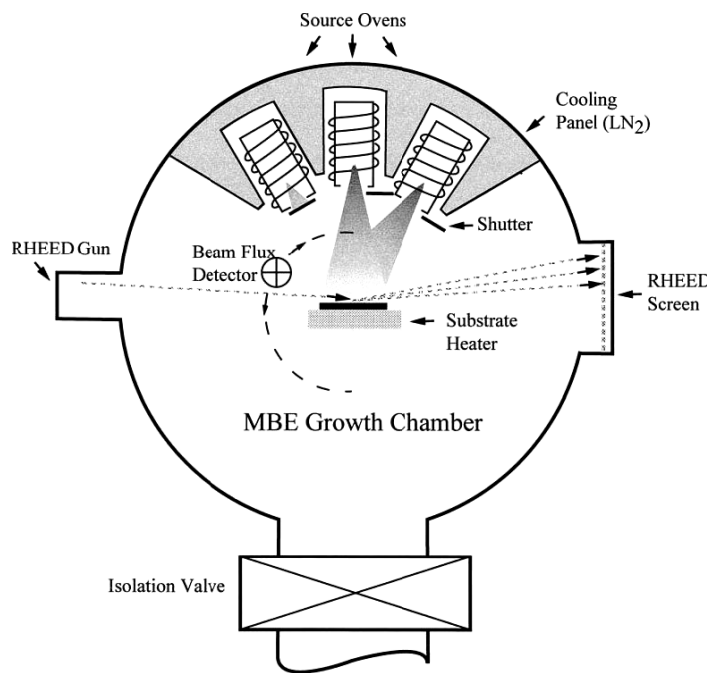


Figure 3-1 Top view of a simple MBE chamber: showing the essential growth sources, shutters, beam flux detector and the RHEED system

Atomic or molecular beams are generated by heating the materials in various individual cells. The types of cells are determined by the specific materials. Effusion cells are used for Ga, Al and Ge and the flux is controlled by the cell temperatures. Mechanical shutters driven from outside the vacuum chamber, are used to switch the beams on and off, enabling monolayer film deposition for each element. A valved-cracker is used to supply As₂ flux,

which includes two heating zones: a sublimator generates arsenic vapor under equilibrium pressure followed by a cracking heater which controls the composition of species, such as As_2 or As_4 . The overall flux of As_2 (or As_4) is controlled by a valve placed after the cracking zone that allows precise arsenic pressure control and also allows instant flux on/off switching, which is important for GaAs growth on Ge. Phosphorus flux is supplied by a GaP-decomposition cell, including, an effusion cell that generates Ga and P_2 flux; and a filter that traps the Ga atoms, producing a P_2 flux only. The P_2 flux is determined by the temperature but the flux on/off is controlled only by a mechanical shutter only, which induces a flux-on/off ratio only $\sim 5\text{-}8\times$. This creates additional growth difficulties for GaP growth on Si. In our MBE machines, all the effusion cell temperatures and shutters are controlled by computers and can be readily programmed to produce quite complex multilayers, superlattices and heterjunction structures.

At typical growth temperatures, the sticking coefficient of As is much less than unity and the As does not incorporate itself, so that the growth rate is entirely determined by the arrival of the group III elements. We thus usually grow with a considerable As overpressure. Typically, a $15\times$ V/III beam-flux-equivalent-pressure (BEP) ratio is used during the growth. The growth rate is usually directly proportional to the group III beam flux for a given material, depending mostly on the geometry of the system. Once the individual growth rate vs. temperature relationships have been calibrated, it is easy to grow any desired composition, for instance any AlGaAs composition, knowing that the total growth rate is the sum of the Al and Ga growth rates, and the composition is found by the ratios of growth rates.

The UHV chamber enables the incorporation of several in-situ characterization techniques, including the reflection high energy electron diffraction (RHEED). The RHEED system provides a diffraction pattern on a phosphor-coated window that is indicative of the ordering of the substrate surface[59]. Thus we can immediately see the effect on film crystallinity due to changes in the growth conditions. RHEED is also an in-situ tool to check the lattice orientation, which allows us to control growth conditions to obtain the correct GaAs phase on Ge.

3. 2 Process flow of OP-GaAs template

Figure 3-2 describes the fabrication process of the orientation-patterned GaAs (OP-GaAs). The growth is initiated on a (001) GaAs substrate oriented with 4° offcut towards (111)B. After an AlAs/GaAs superlattice buffer growth to smooth the substrate, the inverted-GaAs/Ge/GaAs heterostructure is grown.

The GaAs and Ge growth are carried out in two separate MBE chambers that are connected via a UHV transfer tube. One machine is dedicated for III-V growth, and the other is used mainly for Si and Ge growth. Compared with the GaAs growth on Ge, the Ge growth on GaAs is relatively straightforward. No antiphase disorder can occur for the nonpolar growth on the polar substrates. However, as already mentioned, the growth temperature of Ge growth on GaAs is important especially for a thin Ge film. Clustering of Ge occurs at a high growth temperature, as well as the out-diffusion of As through the Ge film. In general, a low growth temperature of ~ 350 °C is desired. We achieved a continuous Ge layer growth as thin as 20Å, observed from cross-sectional TEM images.

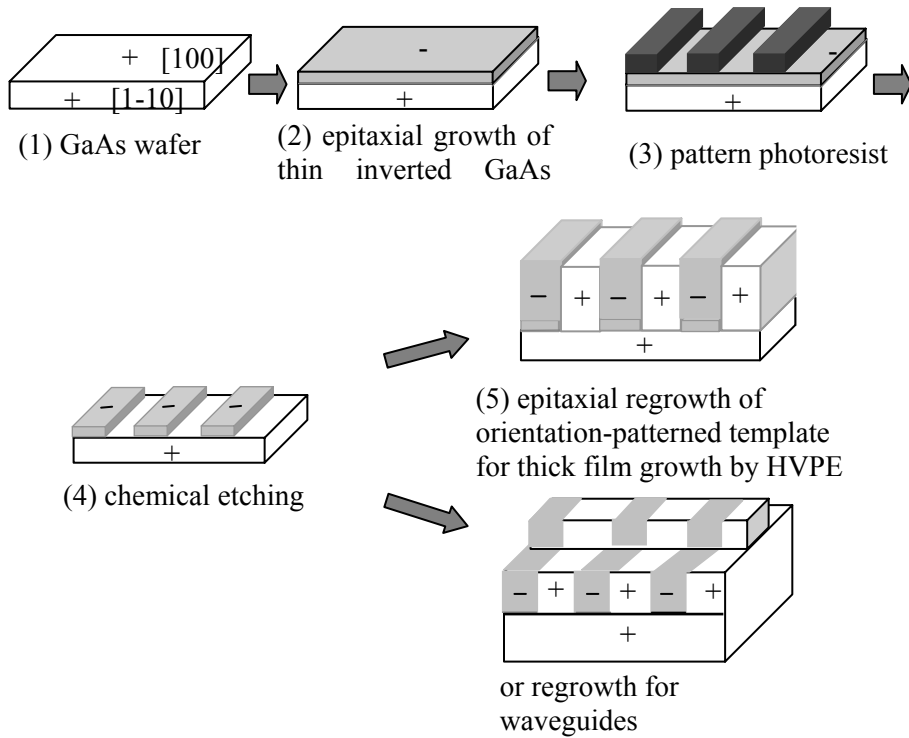


Figure 3-2 All-epitaxial fabrication process of orientation-patterned GaAs

The wafer is then taken out of the MBE system and patterned with the appropriate QPM gratings. After patterning, we use a series of selective chemical etching steps to expose the GaAs surface with different orientations. After chemical etching, the wafer is reloaded into the MBE chamber for regrowth, in which, a thicker layer of GaAs is grown. Hopefully the growth will conserve the orientation patterns. During the regrowth, a thick film (~ 3 μm) is grown to produce an OP-GaAs template and then the templates are taken out as a seed for the thick film regrowth by HVPE. We can also grow an AlGaAs waveguide structure by MBE on the above patterned substrates and then fabricate waveguide devices.

3.3 Growth of inverted-GaAs/Ge/GaAs heterostructures

We fabricated the OP-GaAs GaAs template by first growing GaAs/Ge/GaAs heterostructures. In this section, I first introduce the growth of GaAs on Ge, and also give answers to possible questions, such as why Ge is used in our process and what challenges Ge causes and how to deal with them.

3.3.1 Why use Ge?

The first question raised might be why is Ge used here. The goal of the fabrication process is to control the exchange of the Ga and As sublattices. By accomplishing this, we reverse the direction of As-Ga bonds, thus effectively changing the sign of the nonlinear optical coefficient. However, it is rather clear that epitaxial growth clearly precludes this from happening spontaneously, since it inserts a double plane of Ga or As, as shown in Figure 3-3.

The solution to this issue is to use the properties of the growth of GaAs on Ge to control the orientation. As shown in Figure 3-3, using Ge as a thin intermediate layer, allows one to decouple the orientations of the bottom and top GaAs layers, since Ge has a nonpolar structure. In addition, Ge is almost perfectly lattice matched to GaAs, which makes the growth less difficult.

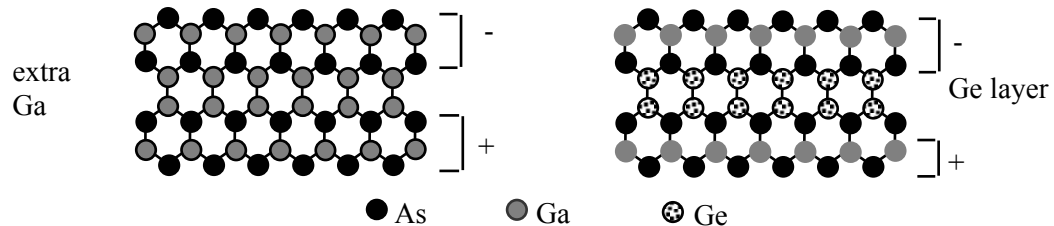


Figure 3-3 GaAs lattice inversion achieved by inserting a Ge intermediate layer

3.3.2 Characteristics of GaAs growth on Ge

The second question is what growth issues are raised by the Ge. A unique problem appears for GaAs growth on Ge. Ge has a diamond structure and GaAs has a zincblende structure. Two possible sublattice allocations are thus possible for GaAs structures, as we already described. In one allocation, Ga atoms occupy the FCC sublattice containing the cubic corners, and in the other allocation, As atoms occupy this FCC sublattice. We usually call these two different sublattice allocations different phases, although they have exactly the same crystal structure. However, for Ge, these two sublattice allocations are exactly the same.

When GaAs is grown on Ge, both phases can start from a Ge substrate, creating significant problems when the different phases join in the active region of the epitaxial layer.

If the Ge surface is perfectly flat, the final structure depends only on the first layer species. If the first layer deposited is not deliberately controlled, containing both Ga and As atoms, the final structure will contain both phases and random antiphase domains (APD) exist. Thus, a single-phase growth can be achieved only by controlling the first layer deposited, usually called a prelayer. Under most conditions, As prelayers are preferred because a monolayer-As is possible, while Ga tends to aggregate.

Unfortunately, Ge surfaces usually contain terraces that are separated by atomic layer surface steps, no matter what kind of Ge substrates are used. There are two types of steps that exist on Ge surfaces, one is monolayer steps and the other is double-layer steps. Figure 3-4 shows the atomic arrangement projected on the (110) planes: (a) shows the Ge surface that contains single-layer steps; (b) shows the Ge surface that contains double-layer steps. During the growth, an As-prelayer is used to deposit the first layer, followed by the codeposition of GaAs. If the surface steps only contain double-layer steps, as indicated in Figure 3-4 (d), the final GaAs is singly-oriented without antiphase defects. On the other hand, if single-layer steps exist, the GaAs grown on the upper terrace has a different atomic stacking sequence from the GaAs grown on the lower terrace and APDs exist, as show in Figure 3-4(c). The generation of APD defects is a characteristic of all polar-on-nonpolar heteroepitaxial growth[61-65].

Besides APD defects, there are other growth difficulties for the GaAs growth on Ge, such as thermal expansion mismatch and lattice mismatch (less than 0.1%). These two factors remain as problems if we grow several microns GaAs on Ge bulk substrates, for example, the thermal coefficient mismatch will cause wafer bending when growing thick light emitting diode (LED) devices on bulk Ge substrates. However, in our process, only a thin Ge (20-100 Å) layer is grown on the GaAs/Ge/GaAs heterostructures and the effect of thermal coefficient and small lattice mismatch will not affect the growth, thus I ignore any further discussion on this topic.

3. 3. 3 Requirements for single-phase GaAs growth on Ge

Based on the discussion of previous sections, the first applicable approach to grow single-phase GaAs on Ge is to create double-layer steps on Ge (001) surfaces. In order to achieve this goal, we have to first investigate the possibilities of surface reconfiguration of Ge surfaces. The study of Ge surface reconfiguration is relatively meager compared with the

study of Si (001) surface reconfiguration, containing only a few experimental results. It is thus instructive to first examine the studies of Si surface reconfiguration. The general conclusions of Si surface reconfiguration in high vacuum are as follows:

(1) The surface steps are dominated by single-layer steps on a clean Si surface without any high temperature anneal.

(2) When Si is annealed at a high temperature (~ 1000 °C), surface terraces reconstruct to form the most stable step configurations[66]. According to the total-energy calculation by D J Chad[67], single-layer steps with a dimerization direction perpendicular to step edges have the lowest formation energy. We note this type of steps as “ S_A ”, where “S” means single-layer steps and the subscript “A” means a dimerization direction perpendicular to the step edges. Accordingly, we represent “D” as double-layer steps and “B” as the dimerization direction parallel to the step edges. The surfaces contain both A-type steps and B-type steps and S_A -steps and S_B -steps usually exist as S_A+S_B pairs. Although the S_A -steps have the lowest formation energy, the energy of a D_B -step is lower than the energy of a S_A+S_B pair. Thus, the most stable step-structure is double-layer steps with the Si dimerization direction parallel to the step edges. The step-doubling has been observed during high temperature anneal of Si surfaces under an As-free environment, which is in agreement with theoretical results.

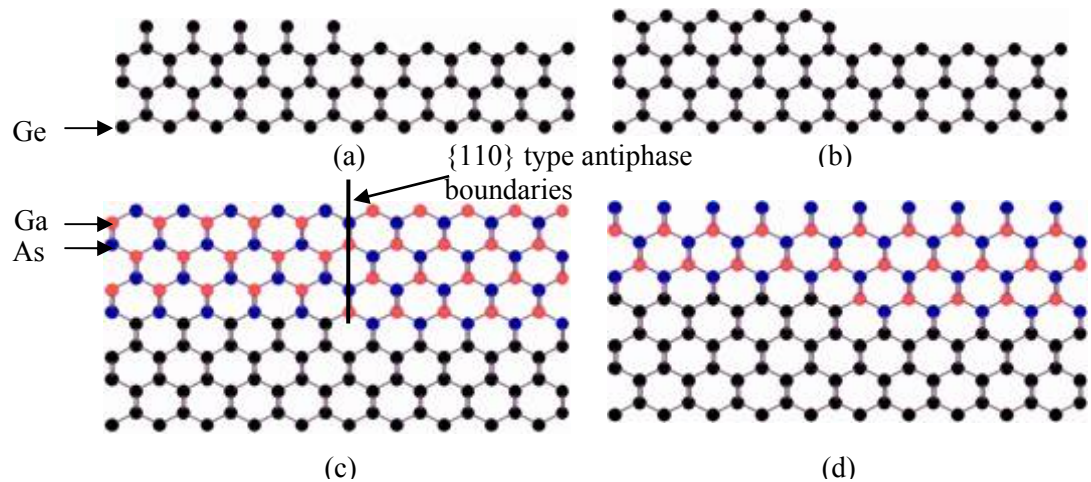


Figure 3-4 Atomic arrangements of Ge and GaAs/Ge structure projected in (110) plane
(a) Ge surface with single-atomic-layer steps;
(b) Ge surface double-atomic-layer steps;
(c) mixed-oriented-GaAs grown on Ge with single-atomic-layer steps;
(d) single-oriented-GaAs grown on Ge with double-atomic-layer steps.

(3) Vicinal substrates are required to facilitate the step-doubling reconfiguration. All the steps are along one direction if the misorientation is toward either the [110] or [1-10]

directions on the (001) plane, otherwise, the steps are along both of the [110] and [1-10] orientations.

(4) The surface reconfiguration of Si surfaces is affected by the existence of As atoms on the surfaces. The interaction of As with the Si surface shows different behavior at different temperatures. Under most cases, the surface under As-exposure results in single-layer steps that are mixed with S_A and S_B .

In our experiments, we also observed similar behavior on the Ge surface, step-doubling on the (001) surfaces of the bulk Ge substrates under As-free environment. However, we never observed the step-doubling on Ge surfaces in the Ge/GaAs structures. Obviously the background As-pressure is not negligible during the surface anneal. The Ge surface reconstruction is possibly affected by As background pressure which comes from As-desorption of GaAs substrates and As out-diffusion during the Ge growth and anneal. Anyway, under all circumstances, the nucleation of APDs seems inevitable for GaAs growth on Ge in the GaAs/Ge/GaAs heterostructures if we rely on the step-doubling mechanism.

A second approach to obtain single-phase GaAs is the self-annihilation of APDs [57, 68-70]. Figure 3-4(c) shows one configuration of the antiphase domain boundaries (APB), in which the APBs grow vertically, forming the {110} type APBs. The APDs will thus propagate throughout the growth and we cannot obtain single-orientation GaAs under such growth conditions. In general, under equilibrium conditions, the {110} types of APBs are the most stable APBs in that they contain equal number of Ga-Ga bonds and As-As bonds and they are neutral in charge state.

However, MBE growth is far away from the thermal equilibrium state. It is possible to find certain growth conditions such that the APBs prefer to adopt different types of APB planes. Figure 3-5(a) shows the case where (111)As ({111} planes containing As-dangling-bonds only) type of APBs are favored. Under this growth condition, two adjacent (111)As APBs will eventually encounter each other and stop at the intersection after a thick GaAs layer is deposited. The domains enclosed inside the APBs will be buried by the domains outside, thus the domains outside become the dominant phase. On the other hand, if the (111)Ga type of APBs are favored, a different phase is achieved, as shown in Figure 3-5(b). Obviously, both (111)As and (111)Ga APBs are not energetically favored under equilibrium conditions in that only As-As or Ga-Ga bonds exist. We need to find the growth conditions to achieve single-phase growth, but it is definitely a more robust approach to get single-phase growth and bury APD domains at the initial growth stages if step-doubling is not possible.

According to the APD annihilation mechanisms, a few conditions are required to achieve

single-phase GaAs growth. The first requirement is to use a misoriented substrate. As discussed above, (001) Ge substrates offcut towards either the [110] direction or the [1-10] direction will produce a surface with all steps along one single direction. During the growth, every two adjacent APBs annihilate each other and one single domain is left in the end. On the other hand, on an exact (001) Ge surface, the steps are randomly distributed along both directions. Thus, there are four APB planes around one APD. If the (111)As type of APBs are favored, one pair of APBs in one direction will annihilate with each other while the other pair of APBs along the perpendicular direction will not annihilate with each other. The APD can never be buried after a thick epitaxial layer growth.

Figure 3-5 also shows that the APD size depends on the step spacing. A high offcut-angle reduces the step spacing, and possibly reduces the sizes of APDs. Thus, a large offcut-angle is generally favored, while a low offcut-angle increases the APD sizes and causes the growth to be more difficult. The typical offcut-angle used by most growers is 4°.

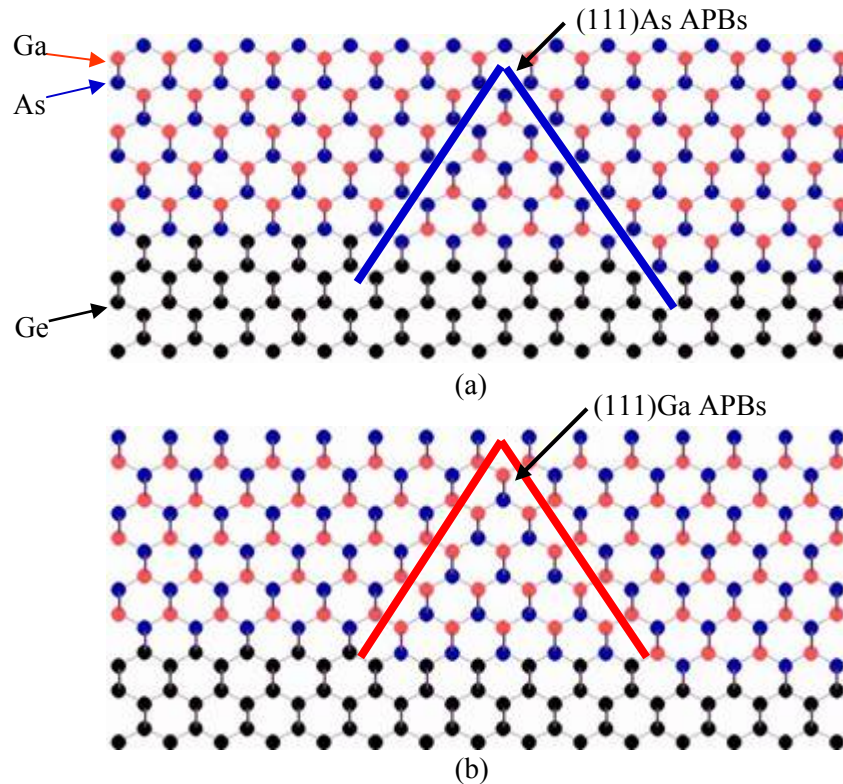


Figure 3-5 Single-phase GaAs on Ge through APD annihilations

The second requirement is the smoothness of the Ge surface. On a smooth Ge surface, the APD size is determined only by the spacing between adjacent steps, and the APD defects can be annihilated after a thin GaAs growth. Large APDs occurs if the Ge surface is rough,

because the arrangement of the surface steps is disordered locally due to the roughness and the growth is away from the ideal case.

In reality, the substrate is never perfectly flat, thus the APD size can be an order of magnitude larger than the spacing of the adjacent steps. This leads to the third requirement for single-phase GaAs growth: a thick GaAs layer on Ge. In general, the GaAs thickness needs to be >100 nm, or even up $1\ \mu\text{m}$ to obtain single-phase growth, which causes severe problems for our template fabrication.

3.3.4 Phase control of GaAs on Ge

Based on the above discussion, we need to find the right growth conditions to make APD annihilation possible in order to control the phase of GaAs. Before discussing the growth, we will first introduce the techniques we used to characterize the phase of GaAs. During the growth, we use the RHEED pattern to examine the phases of both the GaAs substrate and the GaAs on Ge. Figure 3-6 shows the RHEED pattern for single-phase GaAs.

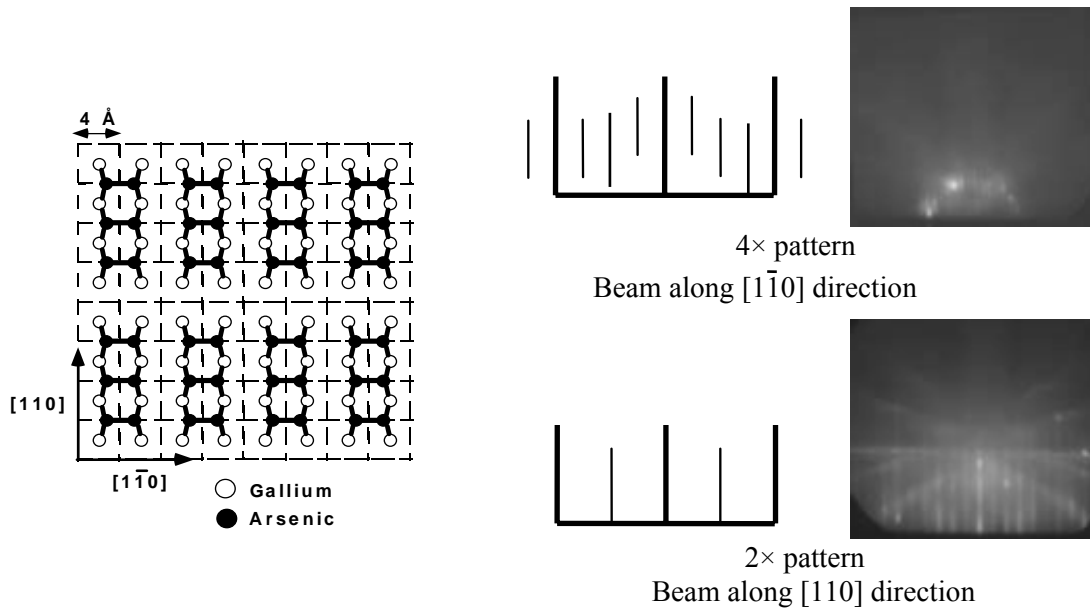


Figure 3-6 $\beta(2\times 4)$ surface reconstruction of GaAs (001) surfaces and related RHEED pattern

As shown in Figure 3-6, under As rich conditions, the $\beta(2\times 4)$ reconstruction is the typical surface atomic arrangement, where all the As-dimers are along $[1-10]$ direction[71-74]. A (2×4) RHEED pattern is observed on this kind of GaAs surface, where $4\times$ is observed when

the electron beam is along the [1-10] direction and $2\times$ is observed when the electron beam is along the [110] direction. Thus, the RHEED pattern can be utilized as an in-situ phase characterization tool.

Previous results by Eyres and Ebert show that the phase of GaAs on Ge in GaAs/Ge/GaAs structures is determined by the growth parameters, such as GaAs nucleation temperature and prelayers[51,56]. We also observed that the thickness of Ge in the GaAs/Ge/GaAs structure affects the GaAs phase on Ge. Both their and our results are listed in Table 3-1, which gives a complete view of GaAs phase control.

Table 3-1 Orientations of GaAs on Ge under different growth conditions

Structure	Ge thickness	Nucleation temperatures	RHEED of GaAs buffer	Prelayers	GaAs on Ge	
					RHEED	Phase
GaAs/Ge/GaAs	10nm	350°C	2×4 or 4×2	As	2×4	$4^\circ \rightarrow 111B$
		550°C	2×4 or 4×2	As	4×2	$4^\circ \rightarrow 111A$
GaAs/Ge/GaAs	2-4nm	300°C	2×4 or 4×2	As	4×2	$4^\circ \rightarrow 111A$
		550°C	2×4 or 4×2	As	4×2	$4^\circ \rightarrow 111A$
GaAs/ Bulk-Ge	500um	400°C	--	As	2×4	$4^\circ \rightarrow 111B$
		550°C	--	As	4×2	$4^\circ \rightarrow 111A$
GaAs/Ge/GaAs	<2nm	580°C	2×4	As	2×4	$4^\circ \rightarrow 111B$
			4×2	As	4×2	$4^\circ \rightarrow 111A$

The results of GaAs/Ge/GaAs with 10-nm Ge were achieved previously by Eyres and Ebert. The RHEED pattern of the GaAs buffer before the deposition of Ge showed the surface reconstruction of the GaAs substrates. The substrates have an orientation of 4° off towards (111)A or (111)B, which are indicated by the different RHEED patterns--- 2×4 or 4×2 . The Ge surface is annealed at 650 °C before the growth of GaAs. Hopefully the annealing induces the double-step-dominated Ge surface. However, single-steps usually exist, which is indicated by the 2×2 RHEED pattern (mixed 1×2 and 2×1). The GaAs growth on Ge starts with As-prelayers and about 30 Å of GaAs is deposited at various nucleation temperatures. After the thin GaAs nucleation layer, a thick GaAs layer is deposited at 550 °C. Finally, the RHEED pattern is recorded to examine the orientation achieved. Their results show that a high nucleation temperature (550C) results in a GaAs phase in which the [110] direction is perpendicular to the steps (4° off towards (111)A), while a low nucleation temperature results in the [110] direction being parallel to the steps (4° off towards (111)B).

Clearly, the orientation of GaAs on Ge depends on the growth condition, regardless of the substrates.

In our growth experiments, we further investigated the effect of Ge-layer thickness in that a thinner Ge layer is desired to reduce the template corrugation, which is one key element to fabricate low-loss QPM waveguides and will be discussed in the next session. We found that the growth is noticeably different from previous results. Under all circumstances, only one GaAs phase is observed if the thickness of Ge is around 30Å, regardless of the nucleation temperatures, prelayers and the substrate orientation; the phase is 4° off towards (111)A. On the other hand, we are able to obtain single-phase GaAs with two possible orientations on bulk Ge substrates, which is exactly the same as Ebert's result[51]. Our observations indicate that certain diffusion or atom exchange processes occurs during Ge growth on GaAs. We are not certain which is the dominant factor, but the latter one is preferred in that the Ge growth is carried out at relatively low temperatures, ~350°C.

In addition, similar results have also been reported by Koh, et al[57], where the Ge thickness is even thinner. Under this condition, the orientation of GaAs on Ge depends mostly on the substrate orientation, as indicated in table 3-1. Thus, the minimum Ge thickness is ~20 Å if we want to grow inverted GaAs on Ge-on-GaAs substrates.

3. 3. 5 Inverted-GaAs/Ge/GaAs growth

Our inverted-GaAs/Ge/GaAs growth recipe is based on the results shown in Table 3-1. The substrate used is 4° offcut towards (111)B. The AlAs/GaAs superlattice buffer is used to smooth the substrates before the growth, hopefully to provide a very smooth substrate and thus get a smoother Ge layer. ~30-Å Ge is then grown. The inverted GaAs is grown with As-prelayers and the growth temperature is at 550°C.

The SEM image shown in Figure 3-7 is a (110) cross-section of the inverted-GaAs/Ge/GaAs structure grown under these growth conditions. The sidewall is etched using an anisotropic chemical etch (NH₄OH:H₂O₂:H₂O=1:1:10) so that the end planes are close to (111)As planes. Obviously the sidewall shapes are different for the GaAs above or below the Ge layer, indicating the orientation is inverted above and below the Ge layer.

We have used this recipe to prepare templates for thick HVPE GaAs film growth. However, there are drawbacks for this recipe, since very thick GaAs, ~1000 Å, is required to get single-phase GaAs growth.

3. 4 Drawbacks of previous OP-GaAs template growth

OP-GaAs templates are fabricated based on the growth recipe of the inverted-GaAs/Ge/GaAs heterostructures and they have been used as a seed for the thick-film HVPE growth. However, there is one drawback of this approach that limits the performance of nonlinear waveguides, which is the template corrugation formed after chemical etching.

3. 4. 1 Chemical etching

During the template growth, a more complicated structure, other than a simple GaAs/Ge/GaAs heterostructure, is grown for etching control. Since the chemical etching depth cannot be accurately controlled with the unavoidable variation of hundreds angstroms per second, etch-stop layers are required. In addition, we want keep the final growth surface away from contamination by photoresist, which will contaminate the MBE chamber and induce defects in MBE-grown films. Thus, a double-etch-stop structure is used to control the chemical etching processes [56]. Figure 3-8 shows the double-etch-stop template structure and the chemical etching procedures. Beside the inverted-GaAs/Ge/GaAs heterostructure, two 200-Å-AlGaAs layers are deposited to control the etching process, with an Al-composition >70%. Finally a 200Å-GaAs capping layer covers the whole structure. Two chemicals were used to preferentially etch the layers: a mixture of citric acid and hydrogen peroxide with 4:1 ratio etches GaAs and Ge but stops at the AlGaAs layer; a mixture of hydrochloric acid and water with 1:1 ratio etches AlGaAs but stops at GaAs.

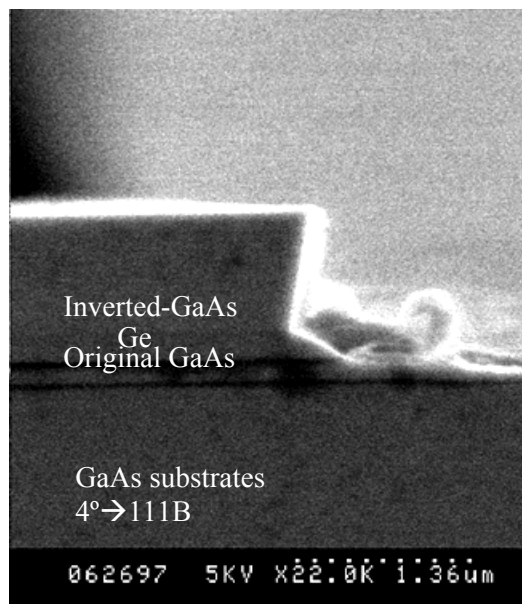


Figure 3-7 Cross-sectional SEM image of the inverted-GaAs/Ge/GaAs structure

After lithographic patterning, the GaAs capping layer is etched and the etch stops at the top AlGaAs layer (step #2), which is subsequently etched (step #3). After removing the photoresist, the inverted-GaAs/Ge/GaAs heterostructure is etched through, and simultaneously, the top GaAs capping layer is removed on the region previously protected by the photoresist (step #4). In the end, the AlGaAs layers are removed to expose clean GaAs surfaces with different orientations.

To ensure the correct etching results, all layers have to be thick enough to protect the layers underneath from being over-etched, otherwise, etching failures, such as etch-pits, will occur. Figure 3-9 shows the top-view of etch-pits taken using the optical microscopy (OM) and SEM. There are several causes for this type of etch pits. One is the roughness of the films. If the layers are too rough and any layer is not thick enough, the chemical etching will penetrate this layer instead of stopping at this layer, thus forming the etch pits. Successive etching will magnify the size of these etch pits. Another reason is that etching can possibly proceed along the antiphase boundaries, regardless of the existence of etch-stop layers.

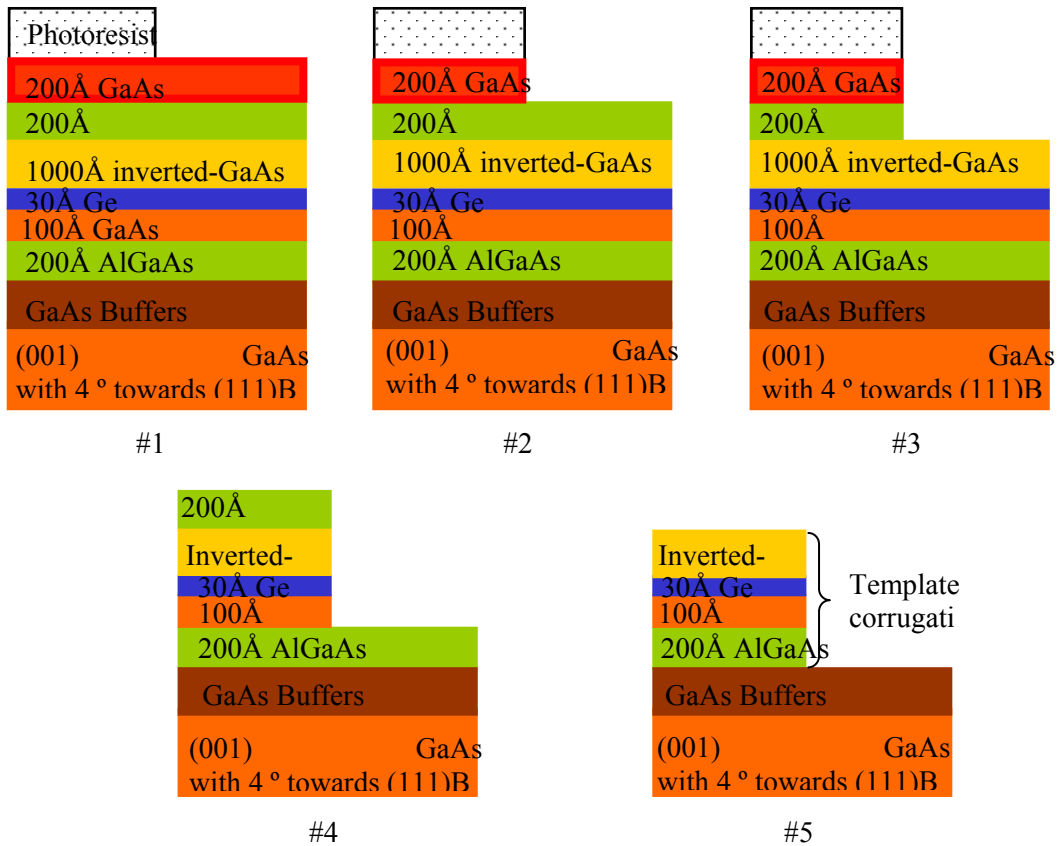


Figure 3-8 Double-etch-stop template structures and chemical etching processes

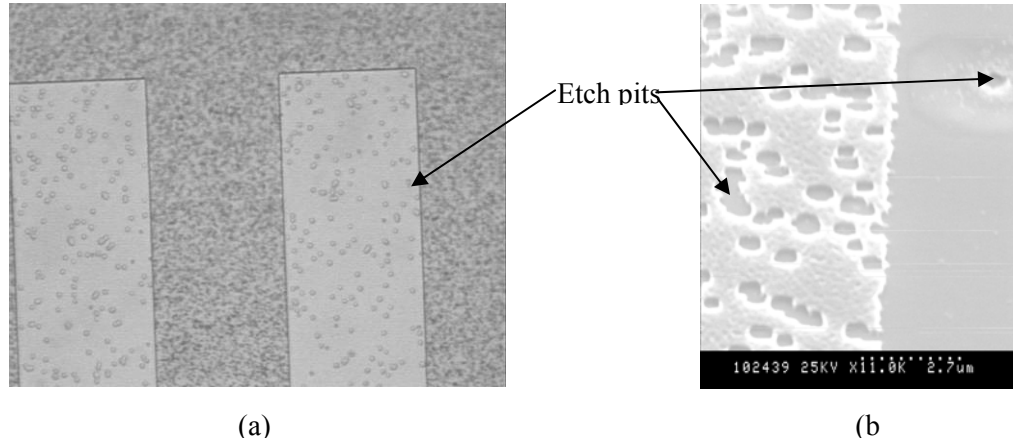


Figure 3-9 Topviews of the etch pits formed during chemical etching
(a) OM image of the template after etching; (b) SEM image of the etch pits.

The etch-pits cause several problems. During the regrowth, the domains grown above the etch pits have the same orientation of the substrates, thus, the domains, which are supposed to be the inverted-GaAs, are not single-phase. Another problem is that the etch-pits result in a rough regrown interface, which induces light scattering in waveguide devices, even for the unpatterned waveguides. Thus, all the layer thicknesses should be thick enough to prevent the formation of etch pits. However, this solution results in large template corrugation.

3. 4. 2 Template corrugation

As shown in figure 3-8, after step#5, the height difference between the inverted GaAs and the original GaAs is $\sim 1330 \text{ \AA}$. This difference is conserved during the regrowth and contributes to the final corrugation of the template, so-called template corrugations. Obviously, the thickness of the inverted-GaAs layer composes the majority of the template corrugation and the thicknesses of AlGaAs and GaAs below the Ge and the Ge-layer itself thickness all contribute only a minor part.

The OP-GaAs template corrugation is negligible for thick-film growth, in which up to 1-mm OP-GaAs is grown and the optical fields are far from the interfaces. However, these corrugations impose great difficulty in the fabrication of low-loss nonlinear waveguides. Under proper regrowth conditions, all the domains grow vertically, and the template corrugation is maintained during the growth. This periodic corrugation causes intense light scattering. Theoretical calculations by Scaccabarozzi[75] and Eyres[56] both show that the waveguide loss is proportional to the square of the template corrugation height. With a 1000- \AA corrugation, the loss can be as high as 40dB/cm at 1550-nm wavelength. As we will see in

the next chapter, this loss value seriously limits the application of AlGaAs QPM waveguides. Thus, our current 1330-Å waveguide corrugation is not tolerable. In addition, a large template corrugation might increase difficulties in OP-GaAs template regrowth. A high template corrugation is not acceptable. We need to find solutions to reduce the template corrugation.

3. 5 Low-corrugation template

3. 5. 1 *Direct reduction of layer thickness*

The template corrugation can be reduced by directly reducing each layer thickness. However, if we simply reduce the layer thicknesses, etch pits as shown in previous section appear. In addition to the pits after chemical etching, we observed pit formation right after GaAs/Ge/GaAs growth without any chemical etching. Figure 3-10 shows typical AFM images with a thin (~300 Å) GaAs grown on Ge. The surface is not continuous after a 300-Å-layer deposition, with dense pits inside the film. AFM shows the maximum depth of the pits is about 15-20 nm. These pits directly evolve into full etch-pits during chemical etching.

We first attribute the pits to insufficient diffusion of adatoms because the structure is grown at a temperature much lower than the normal growth conditions and the Ga-adatom diffusion is not active. Discontinuous layers can form because of this lower diffusion rate. Thus, enhancing the diffusion of Ga-adatoms would help smooth the layer, suggesting the use of migration enhanced epitaxy (MEE)[76,77].

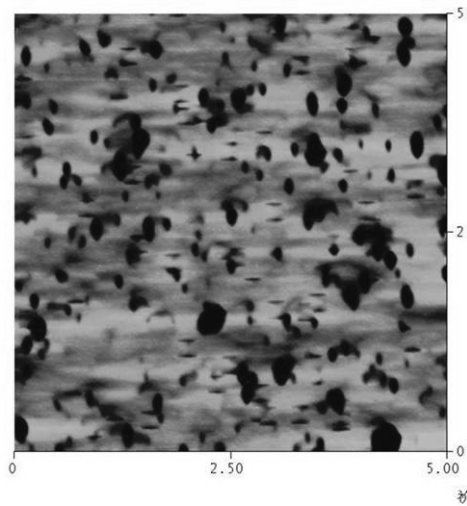


Figure 3-10 AFM image of the pits in GaAs film grown on Ge thin layer

During the normal GaAs growth, the Ga and As fluxes are supplied at the same time, but in MEE growth, the two species are supplied alternately, allowing the adatoms to diffuse

freely until they finally incorporate into the lattice. This growth method increases the migration distance of the adatoms. During each MEE cycle, 1 ML of Ga atoms are supplied with the As shutter closed, and after the Ga flux is shuttered, and following a several-second wait, the As flux is supplied to finish one growth cycle. The Ga-adatoms can move freely when the As shutter is closed. The Ga adatom diffusion time can be adjusted by varying the time used for the monolayer deposition and the waiting time.

Figure 3-11 shows AFM images of GaAs grown on Ge by the MEE growth method. The growth rate of Ga during MEE growth varies between 0.25-0.5 Å/s, with a 3-second waiting time. 200 Å of GaAs is grown by MEE. As indicated by the AFM images, the pits remain when the growth rate is higher than 0.37 Å/s, although the size of the pits is reduced at a lower Ga-growth rate. When the growth rate is further reduced, the pits disappear, but unfortunately, the surface becomes extremely rough. This roughness is attributed to the existence of GaAs antiphase domains. This comparison illustrates that the pits are not caused by insufficient diffusion of Ga-adatoms; otherwise, MEE would have also improved the surface roughness.

We must further investigate how the pits form and what causes these pits. Transmission electron microscopy (TEM) is a useful tool to explore this type of defect.

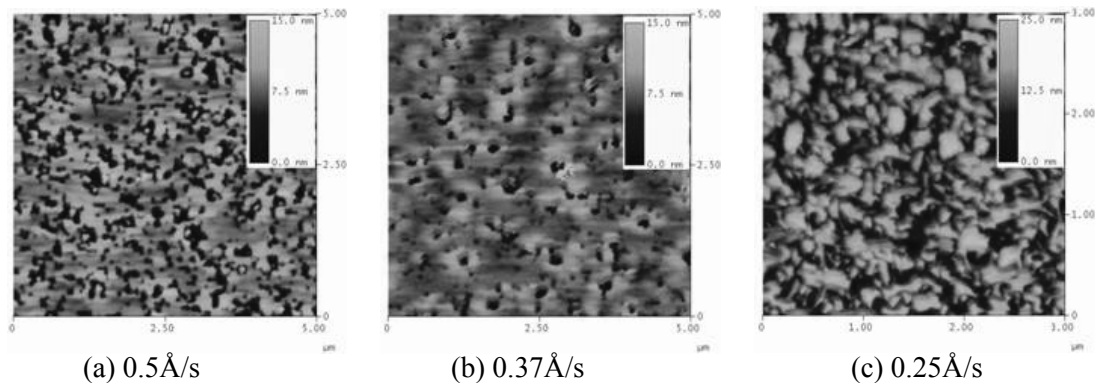


Figure 3-11 AFM images of the GaAs grown on Ge by MEE

Figure 3-12 shows the cross-sectional TEM image of a typical GaAs/Ge/GaAs structure in which pits exist. The bright field (BF) image is taken using the 002 diffraction, which can differentiate GaAs with different orientations[78-80]. It clearly shows that APD defects exist in the film, as indicated by the arrow. The APD is buried inside the film after a thick layer is deposited. However, the layer is much thinner in the area with APDs. Obviously, the pits formed because of the smaller layer thickness are associated with APDs. More observations show that the pit size also depends on the size of APD defects; a large APD defect results in a large pit.

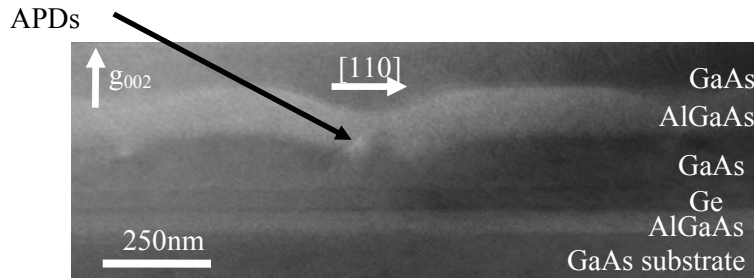


Figure 3-12 Cross-sectional TEM images of the pits GaAs grown on Ge

In this sense, we might speculate that the growth rates of the phases are different; one phase is much faster than the other phase, which leads to these defects. Thus, the surface can only be smoothed by annihilating the APDs as early as possible.

3. 5. 2 Approaches to reduce template-corrugation

Based upon the above APD annihilation model, we concluded that large APDs form most probably because of roughness of the Ge surface. We have observed extremely rough growth just because the substrate is 4° misoriented towards (111)B. The root-mean-square (RMS) surface roughness is 2.8 nm measured by AFM, as shown in Figure 3-13. The peak-to-valley roughness is close to 20 nm. Large APDs are inevitable on Ge surfaces with such roughness. Thus, the first priority to obtain a more ideal GaAs growth condition on Ge is to provide a smoother Ge surface. Based on these considerations, we used the following measures to reduce the template corrugation. First, the substrate is smoothed before the inverted-GaAs/Ge/GaAs growth. Immediate template corrugation reduction can be achieved by reducing the thickness of the etch-stop layers allowed by the smoother GaAs/Ge/GaAs layer. Intermediate template corrugation reduction can be achieved by improved GaAs growth on Ge. Second, one can minimize the thickness of GaAs on Ge by optimizing the growth conditions. Since the GaAs layer thickness contributes most to the template corrugation, the latter improvement can be dramatic.

3. 5. 3 Substrate smoothing

Under normal GaAs/AlGaAs growth, the surfaces are generally very smooth for GaAs homo-epitaxy. However, growth on vicinal substrates is another story. In order to grow single-phase GaAs, a high substrate miscut angle is required. In our recipe, (001) substrates 4° misoriented

towards (111)B plane (or [1-10] direction) are used because only GaAs with 4° misorientation towards the (111)A plane (or [110] direction) can be obtained when Ge layer is thin.

Unfortunately, the epi-layers grown on (001) substrates misoriented towards (111)B are extremely rough, while the growth on the substrates misoriented towards (111)A are very smooth[81-84]. The roughness dramatically reduces when the misorientation angles toward (111)B decreases. Figure 3-13 shows AFM images of GaAs growth on various vicinal substrates. The RMS surface roughness is 2.8 nm when grown on substrates 4° misoriented towards (111)B, while the film grown on substrates with 1° misorientation towards (111)B are very smooth (rms roughness 0.2 nm), which is same as is obtained on substrates with 4° misorientation towards (111)A.

The high roughness on substrates with a high miscut angle towards (111)B are mostly due the surface step configuration differences. Two types of steps exist on GaAs (001) surfaces. The first types of steps are along the [1-10] direction (A-steps) and the step edges are terminated with Ga-dangling bonds. The second types of steps are along the [110] direction (B-steps) and the step edges are terminated with As-dangling bonds (B-steps). Under As-rich conditions, the diffusion of Ga-adatoms along the two types of steps is very different. B-steps are more reactive, and the Ga-atoms incorporate easily, resulting in a short diffusion length; A-steps are less reactive, and the Ga-atoms can diffuse much further before incorporation. The steps on the (001) substrate misoriented towards the (111) A plane are dominated by A-steps. The Ga-adatoms will diffuse along the steps and prefer to be incorporated at the kink sites, thus tending to smooth the steps and adopt a step-flow growth mode, leading to atomically flat surfaces.

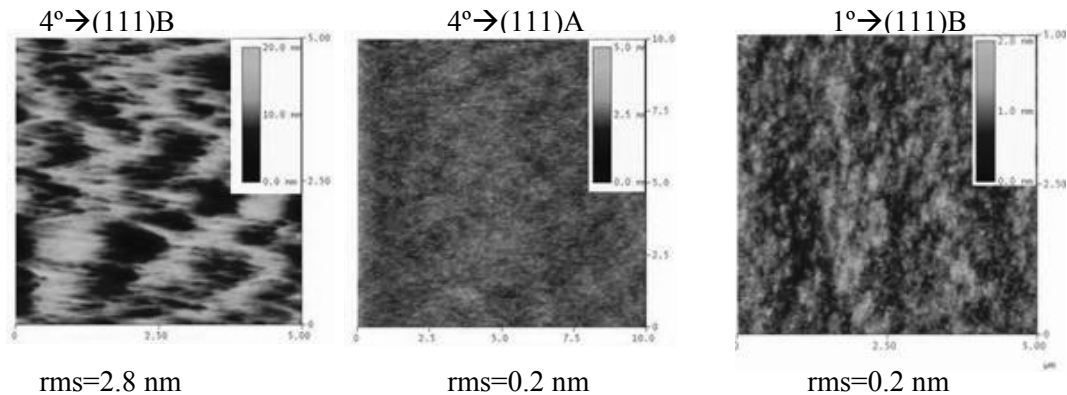


Figure 3-13 AFM images of the GaAs growth on the substrates with different miscut angles

The steps on the (001) substrates misoriented towards the (111)B are mostly B-steps. The Ga-adatoms incorporate on the steps easily before reaching the kink sites, thus they tend to grow at the step-edges themselves instead of smoothing out the steps. This growth behavior potentially causes a much rougher surface. B-steps also tend to react with impurities which inhibit step propagation and further increase the roughness[86].

In addition, the differences of the down-step diffusion also affect the surface roughness. When a Ga-adatom diffuses to a step site from the lower terrace, it will incorporate in the step, which results in the advance of the steps. The Ga-adatoms will also diffuse to the edges from the upper terraces. Usually, an additional step-edge barrier exists and prohibits down-diffusion at the steps. This additional barrier is called an Ehrlich-Schwoebel Barrier (ESB)[87]. If a large ESB exists, the adatoms will nucleate on the upper terraces, resulting in 3-dimensional growth. If the ESB is negligible, the adatoms will cross the steps and incorporate at the step edges and the growth continues with the advances of the steps instead of growth with nucleation and coalescence. This will result in much smoother surfaces. The ESB has been used successfully to explain the surface roughness of quite a few materials system. Similar calculations have been applied to GaAs (001) surfaces. One typical calculation is by Salmi[88] using molecular dynamics. The ESB was calculated to be 0.25eV for the B-steps, while it is zero for A-steps. Most of the other calculations also confirm the easy down-step diffusion for A-steps[89]. Thus, ESB barrier differences also lead to rougher growth on substrates misoriented towards (111)B.

AlAs/GaAs superlattice buffers

One solution to smooth out the substrate surface is to grow a superlattice buffer rather than a simple GaAs buffer. Previous research has shown that the superlattices are effective in smoothing GaAs surfaces, especially for structures with high Al-content. We expected that AlAs/GaAs interfaces trap impurities and minimize the effect of contaminants. The superlattice buffers (15 periods of 450Å GaAs / 50Å AlAs with 500 Å AlAs marker layers after every five periods) have been used to smooth the surfaces for previous template fabrication. However, the remaining roughness is still very high, with an rms value of 2 nm. We are thus not able to reduce the required GaAs thickness to below 1000 Å.

Lower-angle offcut

Another approach is to change the substrates. As already discussed, a smooth layer can be obtained on substrates with a lower offcut angle when the substrate is misoriented towards (111)B or on substrates with large offcut which are misoriented towards (111)A. In theory,

the substrates with a large offcut towards to (111)A are the most desirable, but the unfortunate difficulty of obtaining inverted-GaAs inhibits the usage of this substrate. In addition, even though we can grow the required phase, the GaAs layer above the Ge will still be very rough because this layer is misoriented towards (111)B. Based on this tradeoff, we chose substrates with a lower-offcut-angle misoriented towards (111)B. In our experiments, 1-degree-offcut substrates were used. The surface roughness was reduced by one-order of magnitude, and the total thickness of the required etch stop layers is reduced to less than 100 Å.

Theoretical speculation leads to a pessimistic conclusion that a low offcut angle causes more difficulties in the growth of single-phase GaAs on Ge. As shown in Figure 3-5, we assume the steps are uniformly spaced and the single-layer step height on the Ge surface is one fourth of the lattice constant. The step-spacing is around 20 Å for the 4°-tilt substrates and 81 Å for the 1°-tilt wafer. Thus, in the ideal case, the required GaAs thickness is at least 4 times thicker. Experimentally, the required thickness for single-phase GaAs growth is mostly constrained by the surface roughness and 1000 Å is required the 4° tilt substrates, which is much higher than the step-spacing. The dramatic reduction of the surface roughness can dramatically reduce the APD size before terrace spacing takes effect.

3. 5. 4 Thin GaAs growth on Ge

The growth conditions were optimized after a number of growth runs. The goal was to produce a template structure with layer thickness as low as possible without any pits before or after chemical etching. The set of growth conditions to be optimized included annealing the Ge surface, annealing the GaAs surface on Ge, substrate temperature, arsenic overpressure during the GaAs growth and the growth rate. Combining all these growth conditions, we are able to obtain single-phase GaAs on Ge with a thin layer (~10-20 nm) deposition.

The growth starts on GaAs substrates with 1° offcut. After the Ge deposition, the Ge surface is annealed without arsenic flux supply at 800 °C (thermocouple reading). Although the RHEED pattern is still 2×2 after this annealing, which means single-stpe domains still exist, this anneal affects the results and pits still exist on the sample without this anneal. No direct measurement is available to examine the surface evolution during the annealing, but it is obvious this improvement is not due to the double-layer step formation. One possible explanation is the surface steps are more uniformly spaced after this annealing, so that the growth conditions are closer to the ideal case.

After the annealing, the substrate temperature is reduced to 400 °C and 10 MLs GaAs are deposited using the MEE method. The substrate is then heated to 550 °C and annealed at this

temperature for 5 minutes. During the anneal, the RHEED pattern changes from 4×4 to 4×2, which indicates the surface is dominated by one phase. Meantime, a low As flux ($\sim 1.2 \times 10^{-7}$ torr) is supplied during the anneal, which results in a better 4×2 RHEED pattern, indicating low As flux facilitates this transition.

After annealing, about 10-12 nm GaAs is deposited at the same temperature with a low flux and a low growth rate. The growth rate is ~ 0.15 Å/s, and the BEP ratio of As₂/Ga is $\sim 8 \times$. A low As₂/Ga BEP ratio is a critical parameter to get good single-phase GaAs films because it reduces the required thickness.

Smooth GaAs layers have been obtained using this growth recipe. Figure 3-14 shows the AFM image of the as-grown wafer. The rms surface roughness is ~ 0.3 nm, close to that of the GaAs substrates. No etch pits form during the chemical etching steps. Figure 3-15 shows a high resolution TEM (HRTEM) image of the (110) cross-section of low-corrugation templates. The interfaces are very smooth and additional BF images show that no APDs exist in the film. The template corrugation height in Figure 3-15 is around 22 nm, with ~ 12 -nm of GaAs grown on Ge.

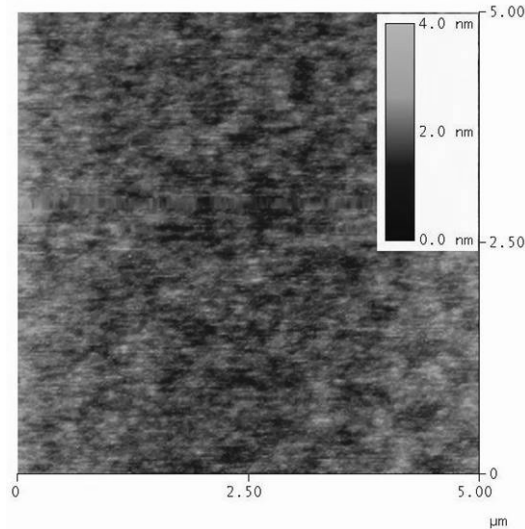


Figure 3-14 AFM image of template structure with ~ 20 nm GaAs grown on Ge

It is expected that similar growth conditions can also be utilized to grow single-phase GaAs on bulk Ge substrates or Ge-on-Si substrates, which are potentially good for the integration of optical devices on Si. In addition, all the results show that a low offcut angle is enough for GaAs orientation control on a Ge surface, rather than the typical 4-degree offcut angle. This result is favored for the growth of GaAs devices on Si.

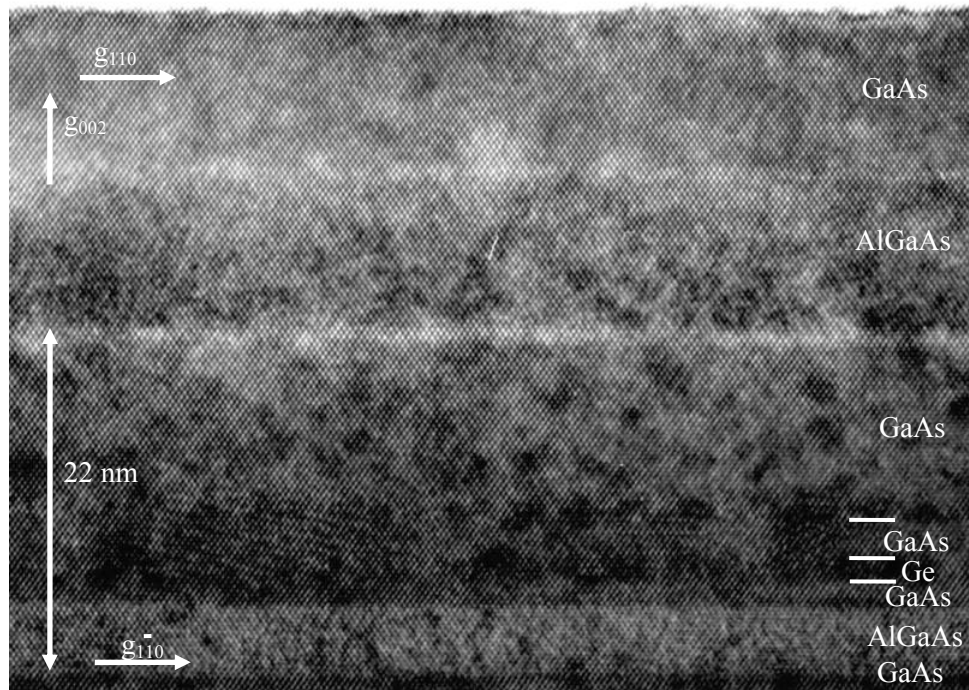


Figure 3-15 HRTEM of the (110) cross-section of the low corrugation template

3. 6 Further investigation of growth mechanisms

We have found that the optimized growth conditions of GaAs on Ge include Ge annealing, low As_2/Ga flux ratio, and GaAs annealing after a thin layer deposition. In order to apply the experience obtained here to the growth of other materials system, such as GaP on Si , we need to better understand the growth. This investigation is instructive in terms of the fundamental materials science.

3. 6. 1 Effects of flux ratio on APB planes

We would like to find out why a low As_2/Ga flux ratio is favored during the growth. This can be examined easily by varying the flux ratio during one single growth and observing the APBs by TEM. We intentionally adopted the nucleation conditions such as un-annealed Ge surfaces that lead to the formation of APD defects. Figure 3-16 shows the XTEM images of the GaAs grown under these conditions. The (110) cross-section is observed, so that the steps on the Ge are perpendicular to this plane and the enclosed APDs can be observed. These images are taken using 002 diffraction in order to see the APDs. Image (a) shows the APBs between two domains, where the APD is very large and is not annihilated, even after the final growth. Image (b) shows two APDs that are smaller and eventually annihilate during the growth.

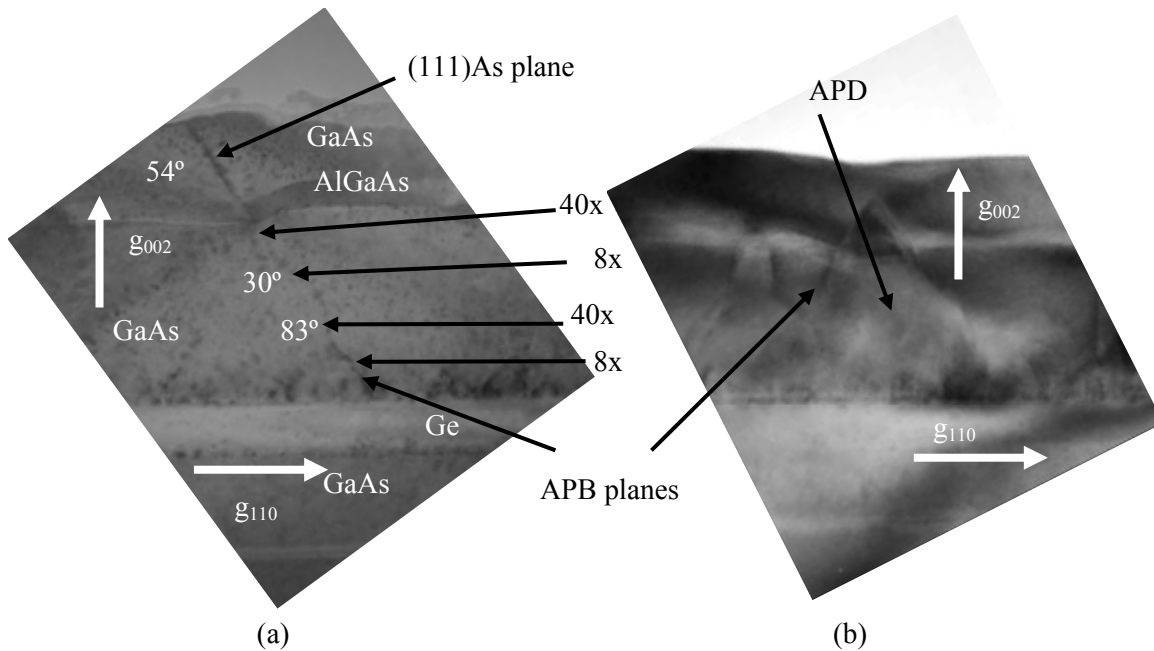


Figure 3-16 XTEM of the GaAs grown on Ge with APDs

First, we notice that all the APBs have similar shapes and this shape is most likely caused by varying As_2/Ga flux ratios. The APB planes compose several straight sections, each section corresponding to one growth condition. The As_2/Ga flux ratio is indicated as shown in figure 3-13. Two BEP flux ratios are used alternately during the growth. BEP=40 \times causes an almost vertical APB plane, while BEP=8 \times induces a more horizontal APB plane. It is clear that the low As_2/Ga flux ratio causes two adjacent APBs to meet each other much faster than high flux ratio, and thus speeds up the annihilation process of the APBs.

In addition to the APB planes, we again observed that the GaAs-layer thickness in the APDs is much thinner than it is in areas without APBs. The AlGaAs marker layer shows a kink at the plane where the APD exists. These observations indicate that the growth rates of the two phases are much different, and the phase with [1-10] perpendicular to the steps grows much more slowly than the phase with [1-10] parallel to the steps. The thickness difference varies strongly with the size of the APDs. A large APD results in a high thickness variation and causes a larger kink in the AlGaAs marker layer. Thus, the smaller the APD is, the sooner the APD is annihilated and the smoother the film.

In summary, the TEM observations indicate that the As_2/Ga flux ratio determines the APB planes and a low As_2/Ga flux ratio speeds up the annihilation of the APDs and helps the growth of single-phase GaAs growth. The growth rate difference could also help one phase become the dominant phase.

3. 6. 2 Effect of Ge surface anneal

In the low-corrugation-template-growth conditions, the Ge surfaces are annealed at a high temperature before the GaAs growth. We hoped this anneal would induce double-layer steps on the surfaces, but unfortunately, this kind of reconstruction doesn't occur. We observed a 2×2 RHEED pattern before and after the anneal. If the Ge surface contains only double-layer steps, a 2×1 RHEED pattern should be observed, because the Ge dimerization directions are exactly identical for all surface terraces. If the dimerization changes directions, a 1×2 RHEED pattern is observed. Thus, a 2×2 RHEED pattern is a mixture of 1×2 and 2×1 , indicating the surface is dominated by mixed domains with both Ge dimerization directions.

However, this annealing appreciably improves the growth. The most likely change induced by the annealing is that the surface steps are more evenly spaced than without annealing. Thus, the APD size can approach the calculated results based on the lattice constant and offcut angle.

3. 6. 3 Growth rate mismatch

We have observed that the growth rates of the two phases are different. Pitted features form due to this difference. In addition, large APDs lead to larger growth rate difference. This growth rate difference is mostly caused by the diffusion anisotropy of the Ga-adatoms on GaAs (001) surfaces. As shown in figure 3-5, in the As-stabilized regime, the GaAs (001) surface reconstructs itself to form As-dimers. The As-dimerization directions are along $[1-10]$ direction. Figure 3-5 shows the typical $\beta(2\times 4)$ reconstruction of a GaAs (001) surface. The Ga-adatoms diffuse along the dimerization direction much faster than along the perpendicular directions. Different anisotropic ratios have been reported based on experimental measurements or theoretical calculations, varying from $4\times$ to $10\times$. The diffusion difference has been attributed to the one missing dimer row in every four dimer rows along the $[1-10]$ direction[90-94]. The effect of this diffusion anisotropy is studied by examining the diffusion of Ga-adatoms across the steps. Figure 3-17 shows three domains separated by two monolayer steps. Assuming the center domain is GaAs with the $[1-10]$ perpendicular to the steps (B-phase), the domains on both sides are GaAs with the $[1-10]$ parallel to the steps (A-phase). The arrows illustrate the fast diffusion direction on the surface of each domain. Assuming the adatoms can diffuse across the steps, Ga-adatoms on the surface of the B-domain will diffuse to the right A-domain along the fast diffusion direction, while the Ga-adatoms will not diffuse back to the center B-domain since the fast diffusion directions are parallel to the steps on the A-domains. Obviously, a low growth rate and a low As pressure favor this diffusion.

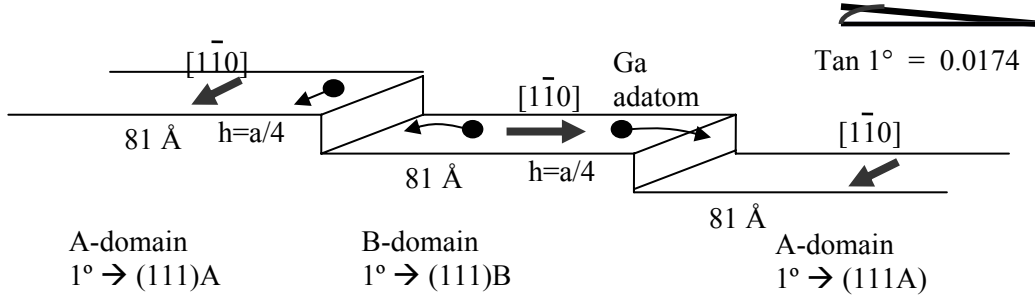


Figure 3-17 Ga-adatoms diffusion on the GaAs surface with double domains

A low growth rate allows the Ga-adatoms to freely diffuse until they finally incorporate at the surface steps. A low As-pressure allows a higher diffusivity. The net effect of this anisotropic diffusion leads to the thickness of the B-domain being much thinner than the A-domains. This thickness difference will be higher and higher due to the existence of APDs and the surface cannot be smoothed out unless the APDs are annihilated in the very early growth stages.

Following these diffusion anisotropy arguments, we now have a better understanding of why MEE growth doesn't help in the annihilation of APDs. The fast diffusion direction on GaAs (001) surfaces is related with the surface reconstruction. It is along $[1-10]$ when the surface is stabilized by As-dimers. During the MEE growth a low As-background pressure is present during the Ga deposition period. The surface is stabilized by Ga-dimers[95], and the fast diffusion direction can likely switch to $[110]$, resulting in the faster growth of B-domains. In this manner, the faster growth area is switched between two alternating domains and the two phases can possibly grow vertically. However, not all of the observations show MEE growth causes the poor results we observed. Some researchers have reported single-phase GaAs growth by growing up to 1000 Å by MEE. We believe the precise growth conditions during MEE growth are responsible for these effects. If the background As-pressure is too high during MEE growth, the surface can still be terminated by As-dimers, which likely happened in most of the cases. In our growth runs, the background As-pressure is low enough, $\sim 6 \times 10^{-9}$ Torr, when the As flux is turned off by the valved cracker during the MEE growth.

3.7 OP-GaAs template regrowth and applications

After the growth of the inverted-GaAs/Ge/GaAs structure, the wafer is lithographically patterned and chemically etched to form the orientation pattern. Then the wafers are reloaded into the MBE chamber to grow the OP-GaAs templates or to grow the AlGaAs waveguide

structures. The growth results for the OP-GaAs templates are briefly introduced in this section, as well as the thick film growth results based on our OP-GaAs templates. Particular care is required for the regrowth of AlGaAs waveguides, which aims to reduce the waveguide corrugation. This will be discussed in the next chapter.

3. 7. 1 OP-GaAs template regrowth results

The critical issue for regrowth is maintaining the phase of each single domain in the template and producing vertical propagation of the induced domains at the pattern boundaries. The total thickness of the GaAs is $\sim 3 \mu\text{m}$ for the OP-GaAs template regrowth, which is thick enough to tolerate the etch-back during HVPE growth. Since the QPM period is relatively large ($> 20 \mu\text{m}$) for most of the nonlinear optical processes inside the transparency range of GaAs, the vertical propagation of the domain boundaries through the template film can be easily obtained under all of the MBE growth conditions tested.

The growth also targets minimization of the corrugations on the domain boundaries. Figure 3-18 shows the typical defects that exist at the domain boundaries. Pits exist at the boundaries. The optimization process of the OP-GaAs template is not complicated, since the domain periods are wide compared with the growth thickness. MEE is used to initiate the growth. A thicker MEE-grown layer results in better boundary quality, however, the required thickness depends on the template corrugation height. Large template corrugation requires a thicker MEE growth to improve the boundary quality. Limited by the MBE machine (limited lifetime of shutter operations), we cannot use MEE to grow very thick GaAs layers to eliminate the corrugations. Thus, the low corrugation template is also desirable for OP-GaAs template fabrication.

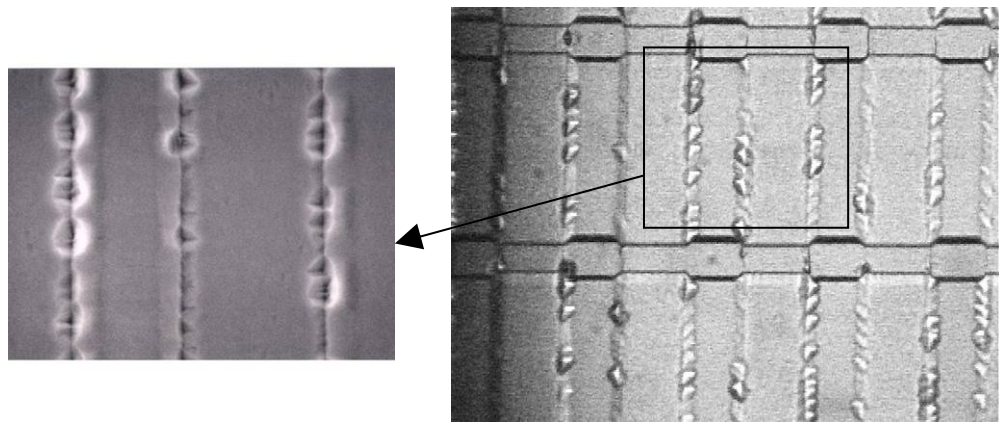


Figure 3-18 Corrugations on the domain boundaries after regrowth

We have obtained low corrugation templates by reducing the substrate miscut angle. In addition, better interface quality is obtained by reducing the substrate miscut angle although the template corrugations are the same. Figure 3-19 shows the improved domain boundaries by reducing the substrate offcut-angle. The regrowth on a 4° offcut substrate shows a pitted domain boundary, while the regrowth on 2° offcut substrates shows a smooth domain boundary. Unfortunately, the GaAs growth rate by HVPE is much lower on substrates with lower offcut angles. It would be very difficult to grow a thick GaAs film (0.5-1 mm) by HVPE using a low growth rate, because the parasitic furnace sidewall growth will impede the continuing growth after a long growth run. Nonetheless, this kind of substrate can be used for the AlGaAs waveguide growth.

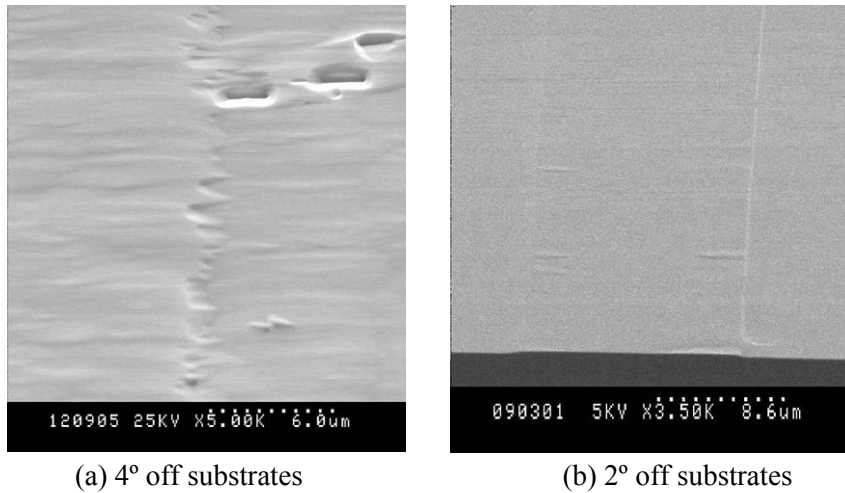


Figure 3-19 Domain boundaries quality improvement

In order to improve the regrowth quality on the 4-degree-offcut substrates, a low As_2/Ga flux ratio was used after $\sim 200\text{-\AA}$ -GaAs growth by MEE. The diffusion length of Ga adatoms increases under a low As_2/Ga flux ratio, and it is effectively equivalent to the MEE in some sense. The boundary corrugation is dramatically reduced under this growth condition. Figure 3-20 shows the final fabricated template, in which no pits at the domain boundaries are observed. However, similar growth conditions are not suitable for the growth of waveguides because v-grooves exist on the domain boundaries and increase the additional waveguide corrugation. The growth of the waveguide structures are discussed in the next chapter.

3. 7. 2 Thick film results and devices results

The OP-GaAs templates were sent to Dave Bliss at the Air Force Research Labs for HVPE thick film growth. Thick films (100s μm) allow propagation of large diameter Gaussian beams, suitable for high power interactions. Although the conversion efficiency of bulk generation is much lower than in the waveguide format, bulk devices allow very high pump power suitable for high power applications. In addition, no corrugation problems exists for bulk devices, as long as the vertical domain propagation is maintained.

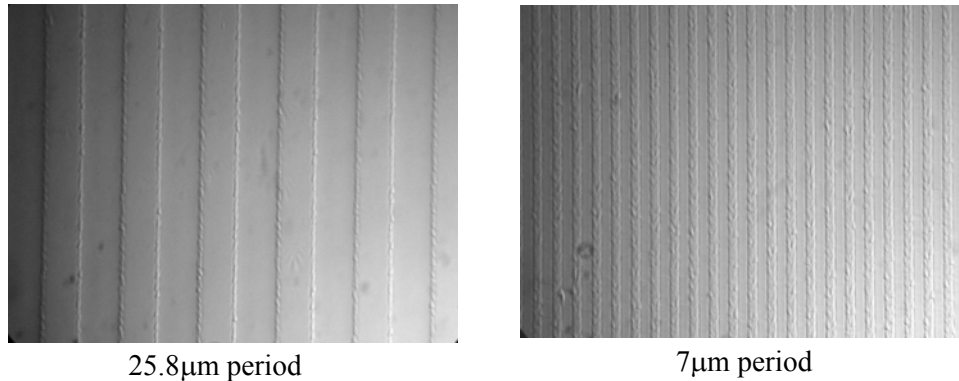


Figure 3-20 Morphologies of the OP-GaAs template after regrowth

HVPE can provide very high growth rates ($>50 \mu\text{m/hr}$). It uses AsH_3 and GaCl as the reactive gases, and H_2 as the carrier gas. The most difficult challenge for HVPE growth is maintaining the vertical domain propagation while obtaining moderate growth thicknesses. It has been found that some domains are closed over after a certain thickness of GaAs growth, especially for the structures with narrower QPM periods. In addition, the parasitic growth on the walls of the reaction tube or at the exhaust will limited the total growth thickness. Quite a few “knobs” are tuned to solve these issues. The details of the HVPE growth optimization process will not be discussed here.

Figure 3-21 shows thick film grown by HVPE. For the 80- μm -period gratings, all the domains grow throughout the total film, while for 40- μm -period gratings, some domains are closed over in the middle of the growth.

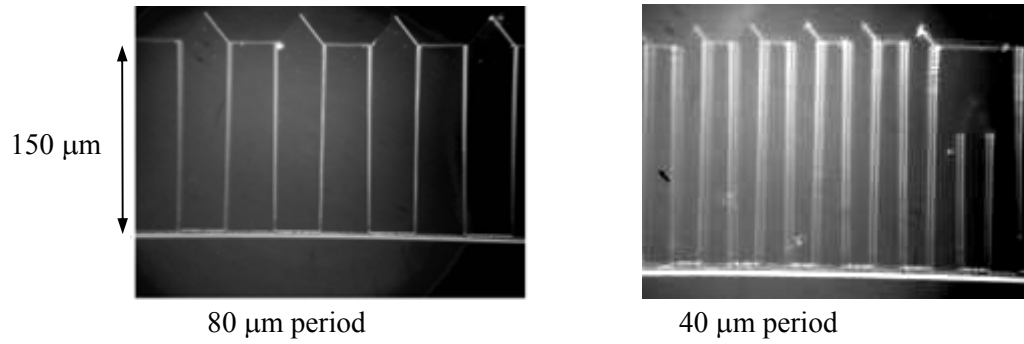


Figure 3-21 Thick OP-GaAs film grown by HVPE

Optical results based on these thick OP-GaAs structures have been demonstrated, including broadband spectrum mid-IR sources generated by optical parametric generation (OPG), THz radiation generated by OPO and DFG[28,29,32]. All these results show that OP-GaAs is very promising as an infrared nonlinear optical material.

Chapter 4 **LOW-CORRUGATION AlGaAs QPM WAVEGUIDES**

As introduced in the first chapter, nonlinear conversion is useful for fabricating optical switches in the future all-optical WDM networks. High conversion efficiency is required due to the low power operating conditions in communications networks. Thus, it is desirable to fabricate GaAs/AlGaAs waveguides in order to take advantage of the high optical mode confinement for high mixing efficiencies. In addition to communication applications, waveguide devices are also desirable for generating mid-infrared irradiation with moderate output power. In this chapter, we describe our efforts to improve the waveguide growth conditions and demonstrate exciting optical results.

4. 1 Introduction

As already mentioned, because of the isotropic nature of GaAs, birefringent phase matching is not possible in conventional AlGaAs waveguides, thus various artificial approaches have to be adopted, such as form-birefringence phase matching (BPM), modal phase matching (MPM), and QPM.

Unfortunately, efficient nonlinear waveguide devices based on the GaAs/AlGaAs system have not been realized regardless of the phase-matching approach because of the propagation losses at the interacting wavelengths. As described in chapter two, in lossless waveguides, the output optical power and the normalized conversion efficiency are proportional to the square of the waveguide length. In lossy waveguides, the attenuation at both fundamental and second-harmonic wavelengths results in most of the second harmonic (SH) power inside the waveguides being generated near the input end of the waveguide but most of the SH power exiting the waveguide being generated close to the output end. The maximum conversion efficiency is obtained with an optimized waveguide length that depends on the loss at the interacting wavelengths so that the waveguides must be cleaved into short devices (1~3 mm) in order to achieve the highest (although still moderate) conversion efficiency.

The lowest loss at 1.6- μm wavelength, ~ 5 dB/cm, has been reported in an AlGaAs nonlinear waveguide using the BPM technique[39-43]. However, the loss at the SH wavelength in this structure is as high as 100 dB/cm, estimated from the low conversion efficiency observed in this type of waveguide. The loss probably comes from the absorption

by levels introduced in the gap of AlGaAs during the oxidation of the surrounding AlAs layers as well as the scattering due to the rough AlO_x/AlGaAs interface. It is not straightforward to devise a method to protect AlGaAs during oxidation and to improve the interface quality. The highest continuous wave (CW) equivalent SHG efficiency in BPM waveguides is around 7%W⁻¹. Although a much higher value is reported for pulsed operation, the pulse duty cycle factor has to be multiplied in order to convert pulsed SHG efficiency to equivalent CW SHG efficiency.

Compared with other approaches, QPM waveguides based on OP-GaAs templates are more promising, since the adjacent domains differ in crystal orientation but have equal refractive indexes, thus no light scattering occurs at the domain boundaries if the waveguide corrugation associated with orientation reversal can be reduced to negligible levels. Unfortunately, in GaAs QPM waveguides, high loss results from scattering by the corrugated waveguide core, which is proportional to the square of the corrugation height. High waveguide loss, varying from 30~100 dB/cm at ~770 nm, has been observed, due to large waveguide-core corrugation, by various research groups[56-57,96-98]. Most of the reported SHG conversion efficiencies for doubling 1.55-μm-wavelength radiation in MBE-grown waveguides are only around 10⁻⁴~10⁻³ W⁻¹ because of this high waveguide loss.

With lower template corrugation, Yoo et al[96] obtained so far the highest CW SHG conversion efficiency (15%W⁻¹) using a 3-mm-long waveguide based on a wafer bonded template and organometallic chemical vapor deposition (OMCVD) rather than MBE regrowth. While propagation loss at 1.55 μm was around 5.5 dB/cm, but the loss at the SH wavelength was still as high as 25~45dB/cm, which limits the conversion efficiency. Nonetheless, these results indicate that AlGaAs QPM waveguides can yield high conversion efficiency if the waveguide loss can be reduced.

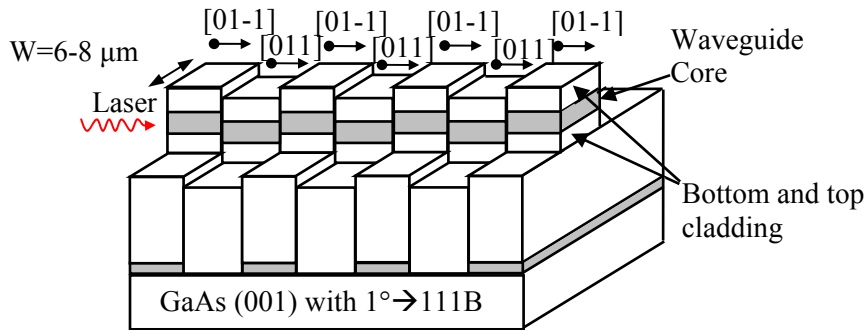
In this chapter, we will describe our fabrication process that leads to low-loss QPM waveguides. We will first describe the design of the waveguide structures suitable for telecommunication applications and then discuss the loss mechanisms of the previous QPM waveguides to identify the main scattering sources. The waveguide growth is then optimized, targeting reducing the losses based on the loss analysis. In the end, the waveguide devices are tested. The conclusions and results obtained in this part will build up a basis for developing low-loss DFG waveguides which can be used either for the communications applications or for generating mid-infrared irradiation.

4. 2 Waveguide structure design

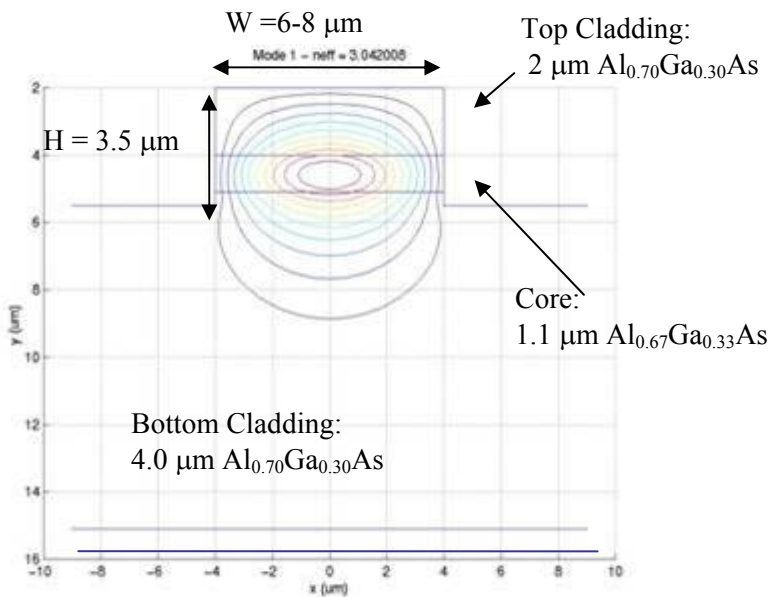
Although our waveguides are targeted for both telecommunication applications and mid-IR source applications, we fabricate waveguides operating around 1.55 μm suitable for optical communications applications to test the quality of our waveguides during the process optimization stage. It is expected that the losses decrease at longer wavelengths, thus we can definitely build low-loss waveguide devices operating in the mid-IR if we succeed in building waveguides operating at 1.55- μm wavelengths.

We start with a waveguide design that operates around 1.55 μm . As already introduced in the first chapter, optical switching is achieved by converting from one wavelength to another wavelength through DFG with the pump wavelength at ~ 775 nm. To meet this goal, several requirements must be met for these applications. First, the waveguides should be transparent at all the interacting wavelengths, especially at 775 nm. Second, the waveguide structure is designed to obtain high ideal conversion efficiency. Third, the waveguide should be single-mode at 1.55 μm so that only one phase-matching peak exists. In the end, waveguides should be low loss so that high conversion efficiency is possible.

The waveguide has been designed by previous coworkers based on considerations above[56,75]. Figure 4-1a shows the geometry of the QPM waveguide design which is grown on the OP-GaAs template. The light is confined in the ridge waveguide core with higher refractive index than the bottom/top cladding and air. The light is coupled into the waveguide core from the front-facet and emits from the end-facet. As shown in Figure 4-1a, corrugations exist in the QPM waveguides fabricated on the OP-GaAs templates. This corrugation will induce intense light scattering. To mitigate the light scattering, weak confinement is used and the refractive index difference is minimized so that the waveguide dimension can be large while still maintaining single-mode operation at 1.55 μm . Figure 4-1b shows the waveguide structure design using a cross-section parallel to the end-facet. The thickness of different layers, the ridge height and the waveguide width are shown in the figure as well. The Al content between the core and cladding differs by 3%, with the waveguide core being $\text{Al}_{0.67}\text{Ga}_{0.33}\text{As}$, and the cladding being $\text{Al}_{0.70}\text{Ga}_{0.30}\text{As}$. The thickness of the waveguide core is 1.1- μm . A high Al composition ensures the transparency at 780 nm. Since the GaAs substrate has higher refractive index than the waveguide core, light will leak into the substrate through the bottom cladding layers, thus increasing the waveguide loss, especially in a weakly confined condition. Thus, a thick bottom cladding layer (5 μm) is required to prevent this power leakage. Single-mode operation at the wavelength 1.55 μm is obtained in the waveguides with widths less than 9 μm ; the mode profile is shown in Figure 4-1b.



(a)



(b)

Figure 4-1 Waveguides structure and the optical mode at 1.55 μm

4.3 Analysis of loss mechanisms

The primary challenge in fabrication of an efficient QPM waveguide is the high loss. The loss in previous OP-GaAs waveguides was above 30-40dB/cm at both the fundamental wavelength 1.55 μm and the SH wavelength and the useful length of waveguide is only ~ 2 mm, leading to extremely low conversion efficiency ($\sim 1\%$ /W)[56,75,98]. Thus, in order to develop waveguides that can be used in practical applications, we need to investigate the sources that cause the losses of our previous waveguides, and find solutions to reduce these losses.

In conventional waveguides without any nonlinear QPM grating, the losses are mostly coming from scattering of the rough sidewalls, the scattering of the interface between the core

and cladding, the material absorption, and leakage to the substrates with higher refractive index. In our case, the waveguides are designed to minimize the effect of the latter two sources, thus the first two sources dominate the waveguides loss. A unique issue exists in our case, where the waveguides are grown on an OP-GaAs template and the template corrugation causes periodic interface roughness between the waveguide core and cladding.

4. 3. 1 Losses due to the periodic waveguide corrugations

As we already mentioned several times, the template corrugation introduces corrugations in the waveguide core. Figure 4-2 shows a cross-section parallel to the waveguide sidewalls so the domain boundaries are perpendicular to the waveguide sidewalls. The effect of the template corrugation is illustrated. During the waveguide regrowth, the height differences between adjacent domains are preserved. Thus, the template corrugation causes periodic corrugation at the core/cladding interface. When the light propagates along the waveguide core, part of the light sees a periodic refractive-index difference.

Theoretical estimations show that the loss is proportional to the square of the template corrugation height. Figure 4-3 shows the waveguide loss as a function of the corrugation period. Two characteristics are shown in this figure. First, the loss is affected by the corrugation period, which indicates that under certain QPM periods, the loss induced by the template corrugation can be minimized. Thus, it is possible to design the QPM periods to minimize the waveguide loss at both wavelengths. Second, the loss is proportional to the square of the template corrugation height. A high template corrugation results in high loss in QPM waveguides. In our early studies, we observed very high loss in these waveguides and obtained a low SHG conversion efficiency of 1%/W[56]. This observation is in agreement with other research groups. Koh *et al*[57], obtained an internal conversion efficiency of $2.0 \times 10^{-3}\%$ /W using QPM waveguides with a 900-Å-template-corrugation height, about three orders of magnitude lower than the theoretical value because of the unexpected high loss.

On the other hand, low-corrugation templates dramatically reduce the loss. As shown in Figure 4-3, when the template corrugation height is about 500 Å, the waveguide loss is expected to be less than 4dB/cm regardless of the corrugation periods. This loss is close to that of the unpatterned waveguides. Although not quite accurate, this simulation indicates that low-loss QPM waveguides are possible with low corrugation templates. The experimental data published by other groups also shows this tendency. Yoo *et al* measured a loss of ~5.5 dB/cm at 1.55 μm with a 300-Å-template-corrugation [96]. Unfortunately, the loss at SH wave was much higher than expected, and the efficiency was still not satisfactory.

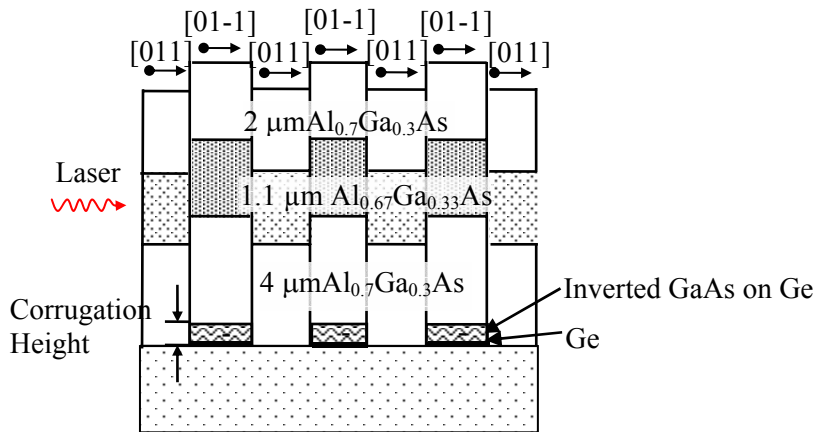


Figure 4-2 Scattering in QPM waveguides due to the template corrugations

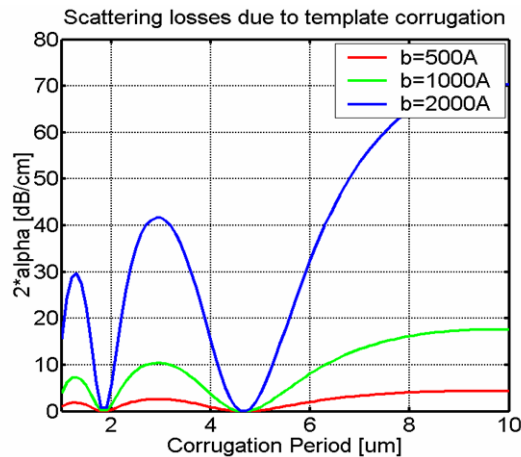


Figure 4-3 Effect of the waveguide corrugations on the waveguide loss

To experimentally characterize the effect of template corrugation on the loss and compare with theoretical estimation, we did a series of loss measurements on waveguides grown on a template with 450-Å-template corrugation. We first measured the loss as a function of wavelength. The measurement results and simulation are plotted in Figure 4-4. Figure 4-4a is the simulation result, which shows that the loss does not monotonically change with wavelength, but instead is close to zero at certain wavelengths. It is expected the scattered light will destructively interfere at those wavelengths and thus the scattered light intensity is close to zero.

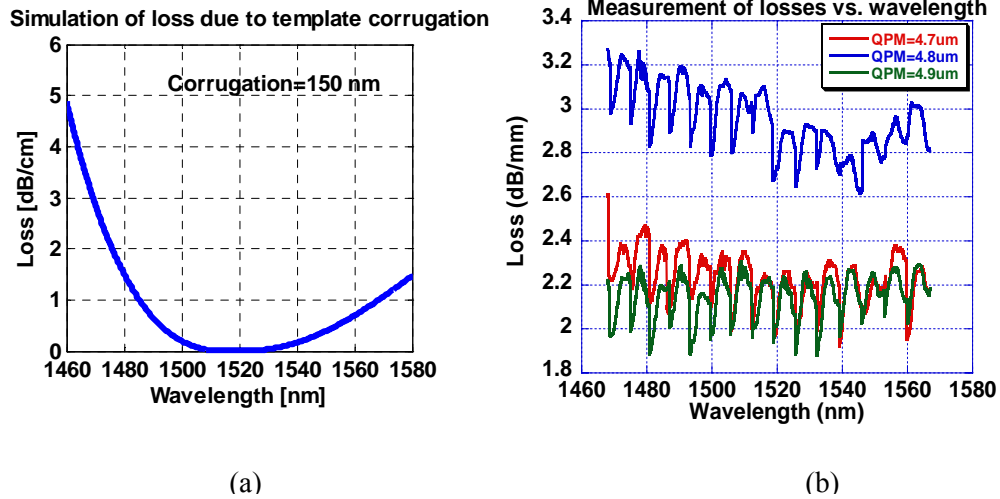


Figure 4-4 Waveguide loss vs wavelengths due to template corrugations

The loss measurement is shown in Figure 4-4(b). Due to the limited tunability of the input laser, the wavelengths are tuned from 1470 to 1570 nm. The data shows three types of waveguides, each with different QPM periods. The fringes in the curves are artifacts during the data acquisition process because of the limited number of samples. It is clear that the plots show a common trend, which is the loss does not vary monotonically with wavelength. The loss is minimum around 1540 nm for the waveguide with 4.8- μm -QPM-period, around 1520 nm for the waveguide with 4.7- μm -QPM-period. The similarity of the simulations and measurements indicate the template corrugation does affect the waveguide loss in agreement with the theoretical estimation. The variation of the loss measured is ~ 0.4 dB/mm, close to the simulation result with $b=150$ nm. This means that the waveguide might have an effective corrugation which is much higher than the original template corrugation. Of course, it is also possible that the theoretical estimation itself is off.

In addition to the magnitude of the loss variation, the measurement also shows a much higher loss value at the minimum point. The loss at the minimum point is ~ 22 dB/cm, much higher than the theoretical estimation. It is clear that other loss mechanisms might exist and that the template corrugation is not the dominant light scattering source for this template.

4. 3. 2 Losses due to the sidewall roughness

Another possible loss mechanism is scattering from the rough sidewalls. This effect is more important for QPM waveguides than for unpatterned waveguides. After waveguide regrowth, the surface is corrugated due to the template corrugation. The waveguide mesa is defined by photolithography and etching. The photoresist acts as a mask during the dry etching and a

hard bake is required to make sure the photoresist is hard enough. During the hard baking, the photoresist reflows and increases the patterned mesa width. This reflow causes uneven mesa width because of the corrugation. The subsequent dry etching transfers the uneven width into the sidewall roughness, as shown in the left image of Figure 4-5. On the other hand, a much smoother sidewall is obtained for the unpatterned waveguide as shown in the right image of Figure 4-5.

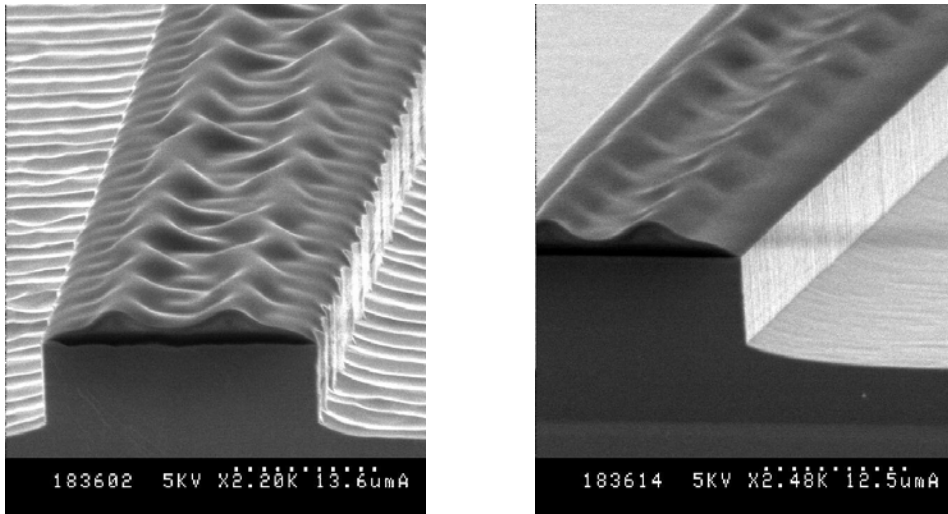


Figure 4-5 Morphologies of both patterned and unpatterned waveguides

Apparently, a large template corrugation increases the sidewall roughness and this can potentially increase the loss. In order to examine the significance of the sidewall roughness, we measured the loss in a function of waveguide width. The results are shown in Figure 4-6. The widths of the waveguides vary from 6 to 13 μm , and the losses of the patterned waveguides with various QPM periods as well as the unpatterned waveguides are measured. As shown in the figure, the losses of the patterned waveguides are above 20dB/cm, much higher than that of the unpatterned waveguides. The loss variation of the waveguides with different width is $\sim 1\text{-}2$ dB/cm. Compared with the 20dB/cm loss, this variation is small. This result demonstrates that the sidewall roughness is not the dominant mechanism for the high loss.

4. 3. 3 Losses due to random interfacial roughness

In addition to the periodic corrugation between the waveguide core and waveguide cladding, a random corrugation exists because of the interface roughness. Apparently this source is not a major contributor for the unexpectedly high loss, because such roughness will also increase the losses of the unpatterned waveguides. Although the interface roughness of the patterned

waveguides is much higher, the increase of the roughness is still small compared with the dimension of the waveguide cores.

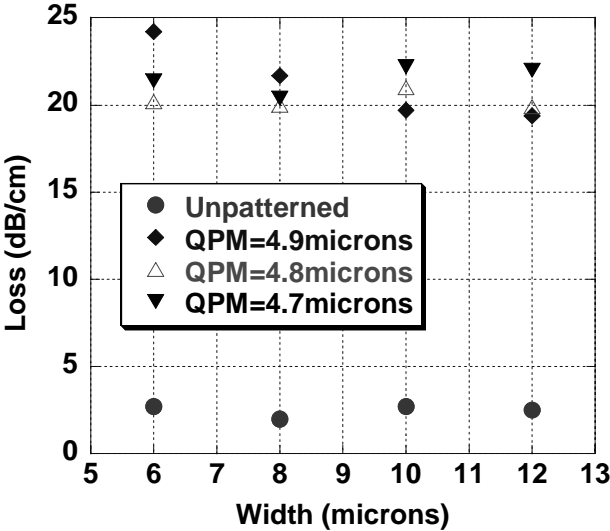


Figure 4-6 Losses vs waveguide widths for both various waveguides

4. 3. 4 Regrowth-induced corrugation—v-grooves

After excluding all other factors, we attribute the high loss to additional corrugation formed during the AlGaAs waveguide overgrowth on the patterned structure. Figure 4-7 shows an SEM image of the waveguide that we measured. The left image shows the top-view of the QPM waveguides, and the QPM domains are clearly defined. The boundaries between domains are not very smooth. The right SEM image shows the details of one of the domain boundaries. Deep v-grooves are observed at the domain boundaries. Apparently the depths of the v-grooves are much larger than the template corrugation. The depths of the v-grooves are measured in a separate cross-sectional SEM image to be ~2000 Å, while the template corrugation is only 450 Å. Such deep grooves will intensely scatter the light and account for the high loss we measured. It is evident that the v-grooves increase the effective waveguide corrugation significantly over the original template corrugation.

As shown in Figure 4-3, if the template corrugation is 2000 Å, the loss can be as high as 40dB/cm. Although the QPM periods are designed to minimize the effect of template corrugation (operated at the minima in Figure 4-4a), the actual minima point might be off from the design point, thus, the loss can be as high as 20dB/cm easily with a 2000-Å-corrugation. In addition to the direct light scattering, the v-grooves also contribute to additional sidewall roughness, as shown in figure 4-7. This additional sidewall roughness would also increase the waveguide loss.

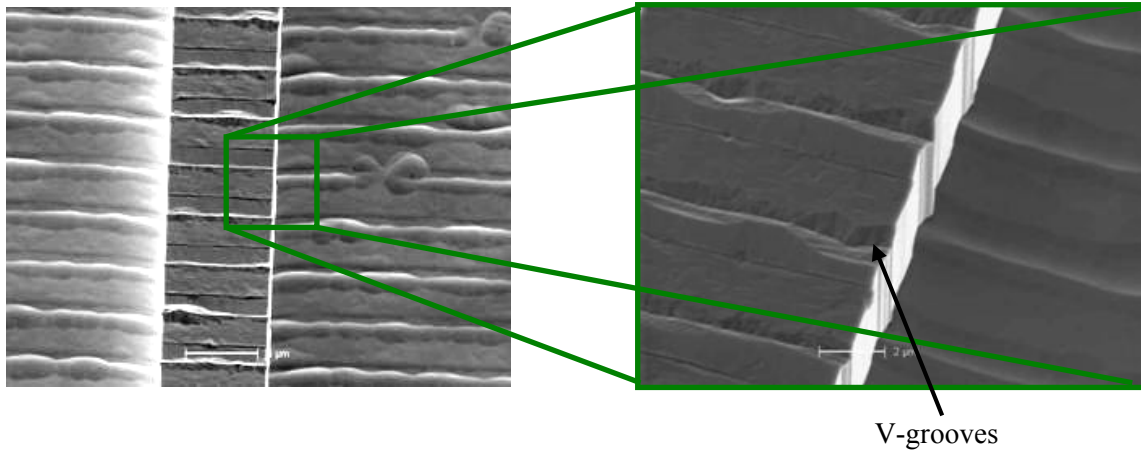


Figure 4-7 SEM images of the QPM waveguides growth on template with 45-nm template corrugation

In this sense, we believe these v-grooves are the dominant loss mechanisms at current stage of development. In order to reduce the waveguide loss, we need to investigate the formation mechanism and explore the growth conditions to eliminate these growth corrugations.

4. 4 Formation of v-grooves

Several factors could possibly account for the formation of the v-grooves. The first possibility is insufficient diffusion of Ga adatoms. A low adatom mobility would induce rough growth and cannot smooth the interface grooves. If this is the reason for the V-groove formation, the solution would be to increase the growth temperature. The second possibility is domain-boundary energetics. The boundaries between the domains are APBs, which are energetically unfavored. During the growth, the adatoms prefer not to incorporate at APBs. If this mechanism is the reason, a low growth temperature will suppress the diffusion of adatoms away from the APBs and help smooth the growth. A third possibility is the surface energy. During the growth, the sidewall will form a facet that is energetically favored. A high mobility of the adatoms favors this facet formation. Again, a low growth temperature will help smooth the growth. Independent of the sources, it is clear that growth temperature will play an important role.

4. 4. 1 Growth temperatures and V/III flux ratio

A new set of waveguides were grown at different temperatures on templates with the same period. The template corrugation is 45 nm. Figure 4-8 shows top-view SEM image of the

regrowth of a thick $\text{Al}_{0.7}\text{Ga}_{0.3}\text{As}$ layer. Two growth temperatures are shown here, 665 °C and 725 °C. The growth rate and V/III BEP flux ratios are identical for two growths. Obviously the domain boundaries of the film grown at 665 °C are much smoother than the film grown at 725 °C. Figure 4-9 shows SEM images of cross sections of the waveguides. The domain boundaries are perpendicular to the cross-section, so that the v-grooves can be observed. The SEM images are taken without additional stain etching to reveal the domain boundaries. As shown in figure 4-9, the domain boundary is visible in as-cleaved samples and all the domains propagate vertically throughout the growth.

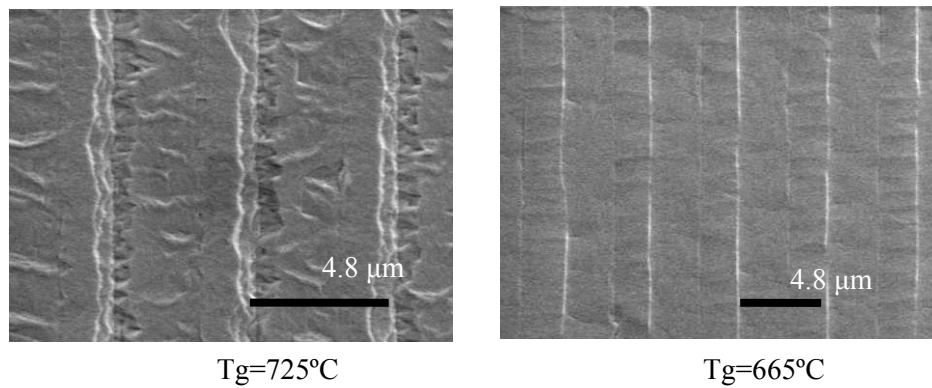


Figure 4-8 Top views of the AlGaAs film growth on the patterned template

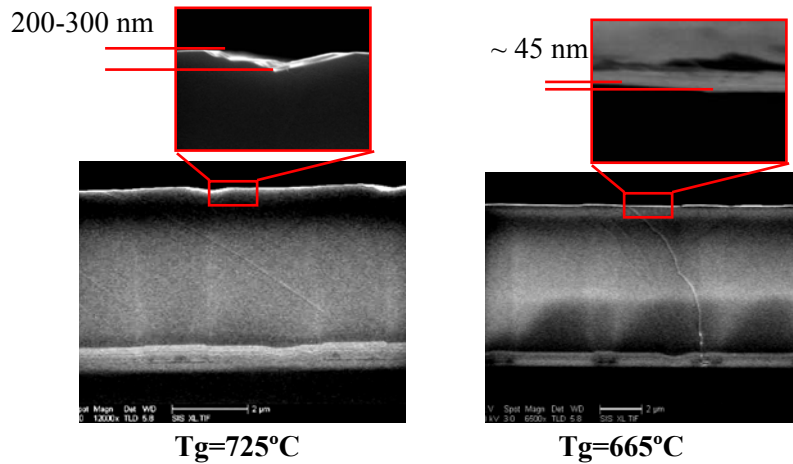


Figure 4-9 Top views of the AlGaAs film growth on the patterned template

Deep v-shape grooves form on the domain boundaries for the sample which is grown at 725°C. The depth of the groove is estimated to be 200-300 nm on the surface and a similar corrugation in the waveguide core is estimated. This magnitude is much larger than the

original template corrugation. With a lower growth temperature, the v-shape grooves become almost invisible. The remaining waveguide corrugation is then close to the original template corrugation, around 45nm. This corrugation height is very small compared with the waveguide core dimension.

This observation indicates that the domain boundary corrugation occurs at high growth temperatures instead of low temperatures. A low growth temperature is necessary to suppress the v-groove formation.

At the same time, it is worthwhile to investigate the reason for the v-groove formation and how the v-grooves form during growth before continuing the growth optimizations. Figure 4-10 shows a cross-section image in which the domain boundaries at the early stage of growth are examined.

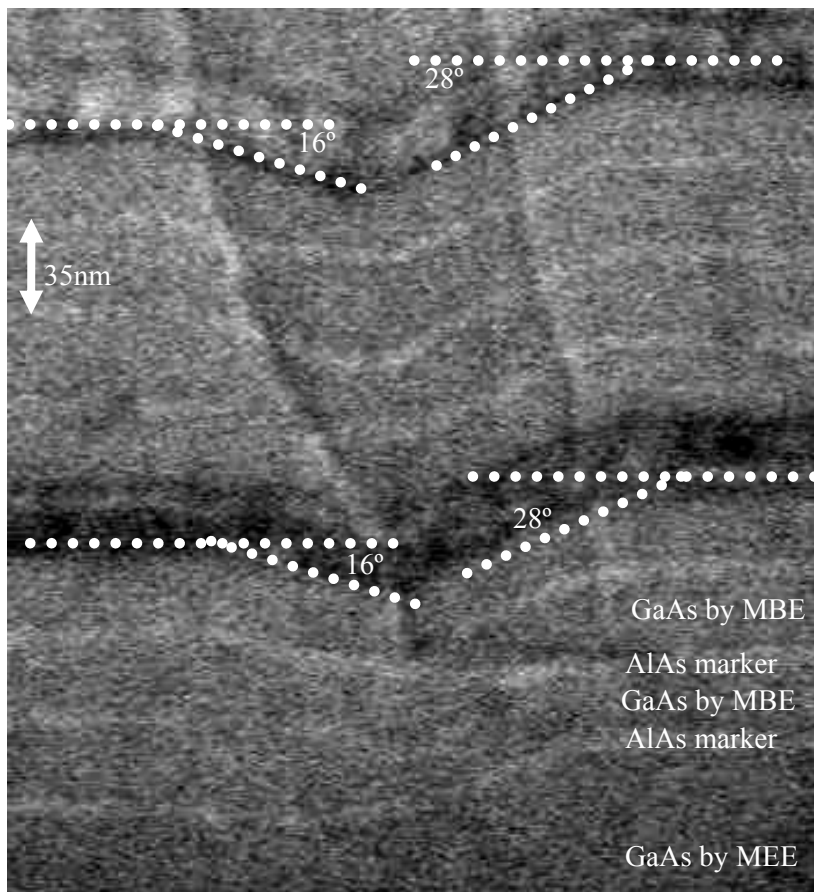


Figure 4-10 Cross-sectional SEM image on the domain boundaries with constant growth conditions

During the AlGaAs waveguide structure growth, a series of buffer layers are grown to smooth the surface which has been chemically etched, including a GaAs layer by MEE growth and AlAs/GaAs superlattice buffer layers by MBE. AlAs layers are utilized as marker-layers in this image to illustrate the formation of v-grooves. As we can see, the v-grooves did not form during the MEE growth stage, but appeared soon after the normal AlAs/GaAs growth. In addition, the facet angles of the two domains are stable once the v-grooves form. During the continuing growth, the facets stay roughly constant if the growth conditions are kept constant.

Figure 4-11 shows a cross-sectional SEM image of a regrowth structure, where the growth temperatures vary during the growth. The growth temperature at the first stage is 695°C and is 665°C in the second stage. Other parameters are exactly same. We can observe a rapid transition of the facet angle after the temperature changes. At the high growth temperature, a facet closer to vertical forms while at low temperature, a facet is more horizontal. It is obvious that a facet close to vertical increase the v-grooves depths.

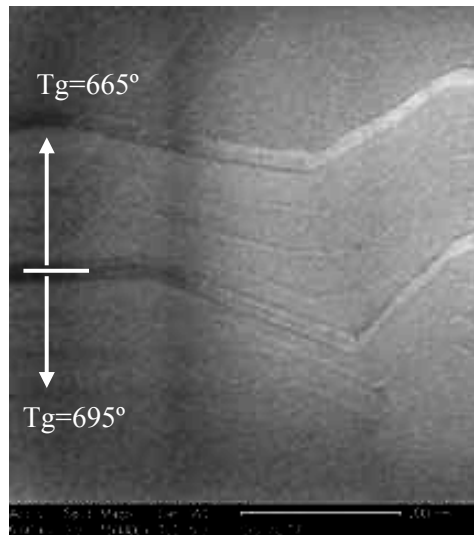


Figure 4-11 Cross-sectional SEM image of the domain boundaries with changing growth temperatures

These results indicate that the stable facet angle depends on the growth conditions. To investigate the mechanisms of the formation of the stable facet, we measured the angles of the stable facets, as illustrated in Figure 4-12. The orientation of each domain on both sides of the APB is indicated. The domain on the right is the domain with different orientation from the substrate, and it is higher than the domain on the left. θ_1 and θ_2 are the angles between the stable facet and the horizontal planes. These angles are measured under various growth conditions and the results are listed in table 4-1.

As shown in table 4-1, the V/III BEP ratio is kept constant at 20x, and the growth temperatures increases from 625 to 695°C. Both angles increase with the growth temperature and stop at certain values at high growth temperatures. This trend indicates that energetically-stable facets exist for the sidewalls of both domains. However, the increase of θ_1 is not as dramatic as θ_2 , and even for growth at high temperatures, θ_1 changes by only 1-2 degrees. This indicates the sidewall facet of the left domain is always close to the energetically favored planes.

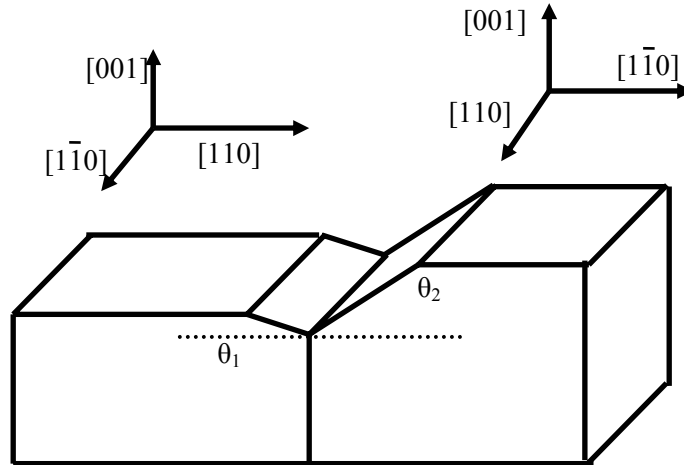


Figure 4-12 Illustration of the facet angles on the domain boundaries

Table 4-1 Stable facet angles vs growth temperatures and V/III flux ratios

Tg(°C)	V/III Flux Ratio	θ_1 (°)	θ_2 (°)
625	20×	17	30
640	20×	16	33
665	20×	18	34.5
695	20×	20	44.5
650	8×	19	54

Table 4-1 also lists the facet angle for the growth with an-8× flux ratio. Again, θ_1 doesn't change much, but θ_2 increases to 54°. Thus, the effect of changing the flux ratio is much greater than reducing temperature only.

These results indicate that the formation of the v-grooves is because the sidewalls of the adjacent domains form facets close to their equilibrium state. The stable facets of the two domains on both sides of the APB are different. Prior studies about the growth of GaAs on patterned substrates have shown similar results[99-106]. If the substrates are patterned with mesas running along [110] or [1-10] direction, at high growth temperatures the sidewall will

adopt certain stable facets[Ref 100]. When the film is grown above the oxide-desorption temperature of GaAs, the sidewalls form stable facets under these growth conditions. The conclusion is that, if the mesa is along the [110] direction, the stable sidewall is close to a $\{111\}$ B plane, which gives a facet angle of 54.7°; On the other hand, when the mesa is along [1-10], the stable sidewall is close to $\{411\}$ A, resulting a facet angle of 19.4°. Our assignment of stable facets is in direct agreement with this observation.

Based on these observations, we conclude that higher growth temperatures and low V/III BEP ratios enable the diffusion of adatoms, fostering the formation of equilibrium facets, leading to the formation of deep v-grooves. We need to suppress the adatom diffusion to eliminate grooves by using a lower growth temperature, higher V/III BEP ratios, or a combination of both.

4. 4. 2 Al composition

In addition to the growth temperature and the flux ratio, the Al composition of AlGaAs also affects surface adatom diffusion and hence the facet angles. Al adatoms incorporate into the surface lattice sites much faster than Ga-adatoms. A high Al-composition has a similar effect to a low growth temperature and high V/III BEP ratio. The required temperatures for suppressing v-groove formation during GaAs growth are much lower than during high Al-composition-AlGaAs growth. V-grooves exist during pure GaAs growth when the growth temperatures are $> 600^{\circ}\text{C}$, while the no v-grooves are observed for $\text{Al}_{0.7}\text{Ga}_{0.3}\text{As}$ growth at 640°C . It is necessary to find the optimal temperature for AlGaAs growth with various compositions. In our case, $\text{Al}_{0.7}\text{Ga}_{0.3}\text{As}/\text{Al}_{0.67}\text{Ga}_{0.33}\text{As}$ is used during the growth and the optimum growth conditions are around 640°C , with V/III BEP ratio at $20\times$.

4. 4. 3 MEE growth

As already introduced, MEE growth is a powerful growth technique to obtain smooth initial surfaces and high crystalline quality, especially useful for patterned regrowth as the chemical etching leaves a rough surface prior to regrowth. Before growing the AlGaAs waveguides on the chemically etched structure, a GaAs buffer grown by MEE helps smooth the surface. The effect of MEE growth can also be observed from Figure 4-10. The initial 400-Å GaAs layer is grown by MEE before the AlAs marker layer growth. As we can see, there are no v-grooves formed during the MEE growth. The v-grooves start immediately after normal GaAs MBE growth. This observation directly contradicts to our original thinking that MEE growth is equivalent to high growth temperatures and low flux ratios since MEE also increases the

diffusion of Ga adatoms.

A possible explanation for this observation would also be similar to our explanation of the effect of MEE on APD annihilation. During MEE growth, the surface experiences a transition from one terminated by Ga dimers to one terminated by As dimers. It has been well recognized in prior studies by various groups[101] that the V/III BEP ratio will alter the stable surface, especially during vapor phase deposition. For patterned mesas running along the [110] direction, the equilibrium sidewall planes change from {111}B planes under As-rich conditions to {111}A planes under Ga-rich conditions. During MEE growth, the As-rich surface and Ga-rich surface appear alternately, resulting in vertical sidewalls, especially for the lower terraces. Thus, no v-grooves form under this growth condition.

Thus, MEE growth can be used to smooth the surface roughness without introducing corrugation on the domain boundaries. The required GaAs thickness grown by MEE depends on the template corrugation height. A higher template corrugation requires a thicker buffer layer to smooth the surface and improve the domain boundary quality. With a template corrugation of ~22nm, only 20-30 nm MEE-grown GaAs is required during the regrowth.

4. 4. 4 Discussions

All our results show that v-groove formation is a result of surface adatom diffusion to form equilibrium facets under high growth temperatures. This explains most of our observations. It is also interesting to compare this orientation-patterned growth with ordinary patterned growth where no antiphase boundaries exist at the pattern boundaries[100,101]. No v-grooves were observed from the studies of other groups, though the sidewall facets at the equilibrium state are close to the equilibrium facets when the mesas are parallel to [110] or [1-10] direction. This difference indicates that APBs actually cause the surface to rearrange and form v-grooves. Since the APB is energetically unfavored, the lower domains will tend to form their own facets instead of staying at the APBs; while in ordinary patterned regrowth, the lower domains prefer not to form their own facets because no additional interface will form at the domain boundaries.

In conclusion, the existence of APBs makes adatom rearrangement necessary and high temperature and low V/III BEP ratio activate the adatom rearrangement.

4. 5 Waveguide growth results

Based on above studies, we sought to optimize the waveguide fabrication process. Figure 4-14 illustrates the significant progress in the waveguide growth. At the early stage of the

development, the waveguides were grown on templates with a corrugation higher than 1000-Å. The substrates were misoriented by 4° towards (111)B. The growth temperature was much higher than the optimal condition. Under these growth conditions, the QPM domains are not clearly defined because of the formation of angled facets. The surfaces are extremely rough, as shown in figure 4-13a and waveguides fabricated from this material were very lossy so that no nonlinear generation was observed with waveguide length as short as 3 mm.

Figure 4-13b shows a photomicrograph of a waveguide grown under optimized growth conditions on the low-corrugation template. The QPM boundaries are clearly defined and no corrugation on the domain boundaries is observed in the image.

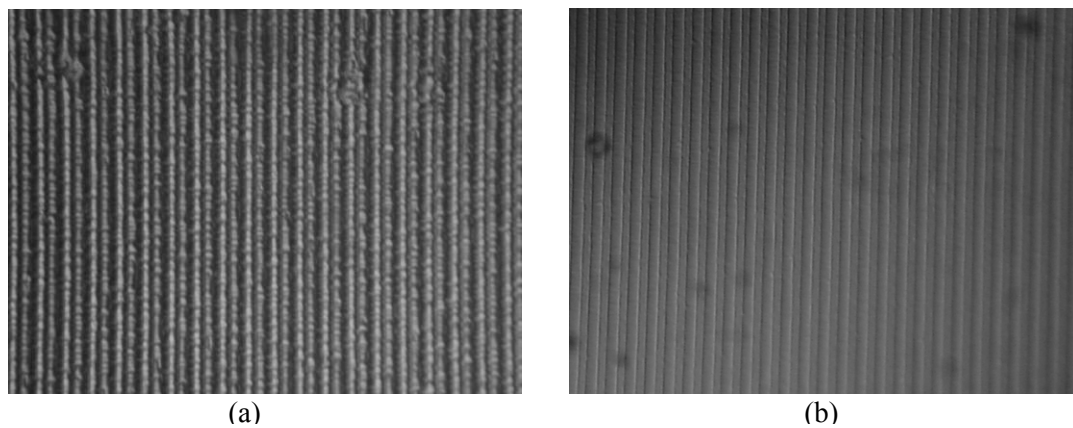


Figure 4-13 Optical microscopy images of waveguide regrowth morphologies
(a) On templates with 1000-Å corrugation without optimized conditions;
(b) On low-corrugation template with 200-Å corrugation after optimization

The top-view of the SEM image of the waveguides also shows good domain boundary quality, as illustrated in Figure 4-14a. The domain boundaries are almost invisible. However, the duty cycle of each domain is off from the nominal 50% design due to the accumulated errors during lithography and chemical etching. This kind of duty cycle offset will reduce the conversion efficiency, but will not increase the waveguide loss. The cross-sectional image is shown in Figure 4-14b. No v-grooves exist on the domain boundaries, and the corrugation between adjacent domains is ~20 nm, close to the original template corrugation. It is also worth mentioning that the APBs can no longer be directly observed in Figure. 4-14, but can be revealed by additional stain etching, while in Figure 4-9, the APBs are visible without any stain-etching. This indicates that under optimized growth conditions, the domain boundary quality is dramatically improved.

4. 6 Waveguide fabrication

After the regrowth of waveguides on the OP-GaAs template, the film is patterned to define the waveguide mesa. The film is then etched using photoresist as an etching protection mask to form waveguide ridges. Etching is the most important step in waveguide fabrication because it will define the geometry and dramatically affects the quality of the sidewalls. Two different kinds of etching exist: wet, and dry.

A simple and quick way to etch waveguides is wet etching. However, this etching produces a curved sidewall shape, and is not desired for the ridge waveguide fabrication, because straight sidewalls are required. In addition, the etching is not repeatable because the etching rate will change, depending strongly on temperature, time since the solution was mixed, and agitation speed, as well as the dimension of the waveguides. It is hard to control the etching depth just by timing, thus dry etching is desired to meet our requirements.

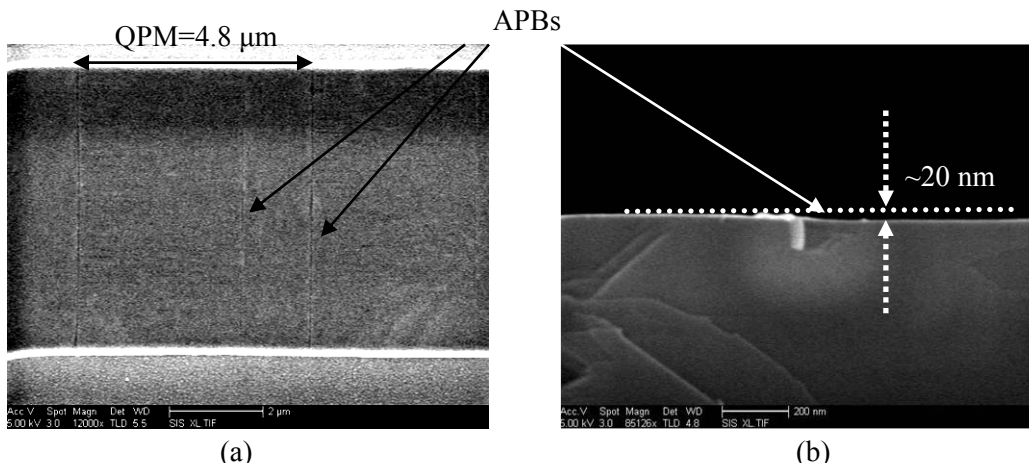


Figure 4-14 SEM of the regrowth on the patterned templates
(a) Top-view; (b) Cross-sectional view

4. 6. 1 Dry etching

Plasma etching can provide straight sidewalls and the etching thickness can be controlled to be within 5% of the target etching depth. Plasma etching is performed using a discharge in a reactive gas to create reactive atoms and radical species that react with surfaces to form volatile compounds. The formed products evaporate from the surface, leaving an etched substrate.

In our case, we use a technique called Electron Cyclotron Resonance (ECR) enhanced Reactive Ion Etching (RIE). RIE is the most widely used etching technique and is based on a combination of chemical activity of reactive species generated in the plasma with physical

effects caused by energetic ion bombardment. A microwave generator provides high density plasma through the ECR technique. The combination of these two techniques gives a high-density of low-energy ions in the plasma. We can thus obtain highly anisotropic etching with high etch rate and low surface damage.

The photoresist is recognized to be the key factor for the sidewall roughness. The pattern roughness of the photoresist causes a rough sidewall. In addition, the photoresist can be damaged by the plasma, also adding to the sidewall roughness. Thus, two approaches are required to improve the quality of the sidewalls: (1) pre-treat the photoresist to make it smoother and more resistant, and (2) modify the process to reduce photoresist damage during etching.

Pre-etching treatment of the photoresist is required in order to avoid burning the photoresist during etching. In order to make the photoresist hard enough to avoid damage during etching, hard-baking at high temperature (130°C) for long time (~30 min) is used. Baking at this temperature makes the photoresist reflow, producing a typical rounded pattern shape. The reflow of the photoresist smoothes out most of the pattern roughness and a more uniform mask is obtained for the unpatterned waveguides. However, for QPM waveguides, the reflowing transfers the surface corrugation into periodic sidewall roughness. This periodic sidewall roughness makes the loss of the QPM waveguides higher than that of the unpatterned waveguides. The magnitude of the induced-sidewall roughness due to the photoresist reflowing is determined by the waveguide corrugation. In this sense, a low-corrugation template is necessary for reducing the sidewall roughness without changing the waveguide etching recipe. The waveguide grown on a template with 20-nm corrugation shows a sidewall roughness of ~20 nm, which is close to the sidewall roughness of the unpatterned waveguides. However, this periodic roughness, even though of similar dimension increases the loss compared with the uncorrelated sidewall roughness. After hard baking, the sample is then exposed to UV radiation for a long time (~20 min), so that the thin, sharp photoresist edges become hard enough to withstand the plasma damage.

4. 6. 2 Diffusion-limited etching

Since the main advantage of wet etching is smoothness of the walls, it is desirable to use wet etching to smooth the sidewalls after dry etching. Diffusion-limited etching is the best choice for smoothing the roughness because the etch rate of the protruding area is faster. The chemical used is HCl:H₂O₂:H₂O=80:4:1. The etching rate of this etch is ~0.4 μm/hr. To smooth out the sidewall roughness, a very fast dip in the etch is required. Otherwise, over-

etching occurs, resulting in both curved sidewalls and a much narrower waveguide width than designed. The dipping time is as short as 5s. The etching results are demonstrated in figure 4-15. Figure 4-15a shows a top view SEM image of the waveguide. The waveguide runs horizontally. The sidewalls are very smooth. However, curved sidewalls form after this diffusion-limited etching as shown in figure 4-15. Early studies have shown that this kind of sloped sidewalls increase the waveguide propagation loss[107]. There is thus competition between a smoother sidewall which reduces the loss, and the sloped sidewall which increases the loss. Obviously the smoothing effect is more salient when the template corrugation is high, but small when the template corrugation is low.

To avoid the formation of curved sidewalls, it is necessary to use chemicals with much smaller etch rates, so that the etching process is easier to control. Unfortunately, this optimization process has not been investigated in this dissertation work and remains as one of the challenges for fully optimized waveguides.

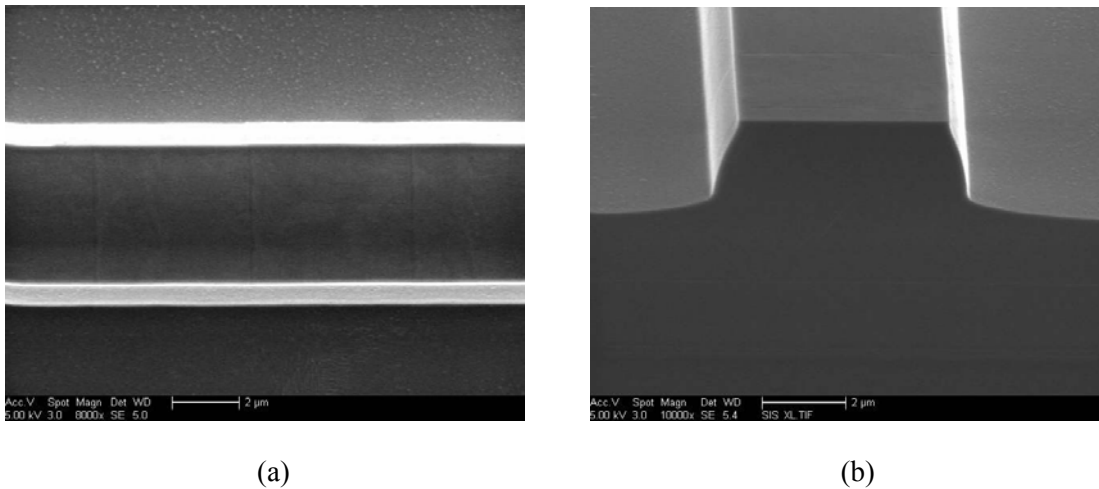


Figure 4-15 SEM of the fabricated waveguides

4. 7 Optical characterization

After we were satisfied with both the regrowth and waveguide fabrication quality, we cleaved the waveguides into samples with various lengths to characterize the optical performance, including losses and SHG. In this section, without additional comment, the results described are from waveguides which were grown on low-corrugation templates with 22-nm corrugations using optimized regrowth conditions.

4. 7. 1 Loss measurement

4. 7. 1. 1 Fabry-Perot measurement at 1.55 μm

The loss at 1.55 μm is measured using a technique called the Fabry-Perot technique[108], which is very useful because it is insensitive to the coupling efficiency into the waveguide. To measure the loss, we cleave two end facets and launch light into the waveguides. The facets act as mirrors, creating a Fabry-Perot cavity and the transmission of the light then has several peaks and valleys, as shown in Figure 4-16. From the contrast between the peaks and valleys, knowing approximately the reflectivity of the facets and the length of the guide, we can derive the value of the attenuation coefficient.

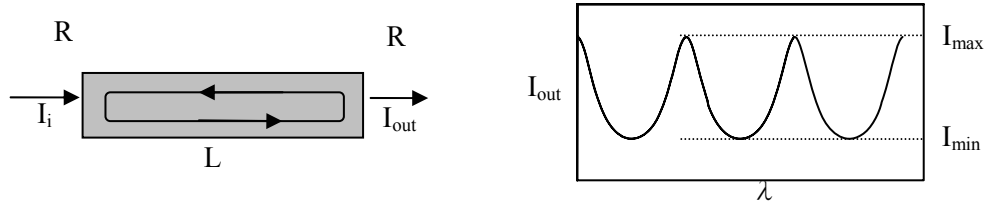


Figure 4-16 Fabry-Perot method for loss measurement

Fabry-Perot technique theory

The coherent intensity transmission of a Fabry-Perot cavity as depicted in the insert of Figure 4-17 is determined by the following equation:

$$\frac{I_t}{I_0} = \frac{\eta T^2 \exp(-\alpha L)}{(1 - R \cdot \exp(-\alpha L))^2 + 4R \cdot \exp(-\alpha L) \sin^2 \frac{\phi}{2}} \quad 4.1$$

$R = \sqrt{R_1 R_2}$, $T = \sqrt{T_1 T_2}$, where $R_{1,2}$ and $T_{1,2}$ are the intensity reflection and transmission coefficients for the two dielectric mirrors. α is the total intensity attenuation coefficient, and $\phi = 2\beta L$ is the phase delay, L being the cavity length and β being the propagation constant in the waveguides. η is the coupling efficiency to the cavity. By changing the wavelength, the phase delay of the light in the cavity is changed and the transmission exhibits Fabry-Perot fringes with maxima and minima as predicted by equation 4.1. From the maximum and minimum transmitted intensity, I_{max} and I_{min} , the contrast K is defined:

$$K = \frac{I_{\max} - I_{\min}}{I_{\max} + I_{\min}} \quad 4.2$$

and $R \cdot \exp(-\alpha L)$ can be expressed as a function of K :

$$R \cdot \exp(-\alpha L) = \frac{1}{K} \left(1 - \sqrt{1 - K^2} \right) \quad 4.3$$

thus, the waveguide loss can be expressed as:

$$\alpha = \frac{4.34}{L} \left(\text{Ln}(R) - \text{Ln} \left(\frac{1}{K} (1 - \sqrt{1 - K^2}) \right) \right) \quad 4.4$$

The precision of the measurement is limited by the precision of “ R ”, meaning the mirror reflectivity. In weakly confined waveguides, R is roughly determined by the modal effective refractive index, such as:

$$R = \left(\frac{n_{\text{eff}} - 1}{n_{\text{eff}} + 1} \right)^2 \quad 4.5$$

where n_{eff} is the modal effective refractive index.

This technique is valid only for relatively low-loss waveguides, and sufficiently long waveguides, so that this sensitivity is not too serious. In addition, it is suitable for single-mode waveguides. In multimode waveguides, the superposition of the Fabry-Perot fringes of the different optical modes changes the contrast and the loss measurement is invalid.

Measurement results

Figure 4-17 shows the loss as a function of waveguide width. The waveguide widths are measured from SEM images, which are 1- μm narrower than the nominal design due to the over-etching during the sidewall-smoothing process using the diffusion-limited etching. In the plot, the waveguides with 9- μm widths are multi-mode waveguides and the loss value measured using the Fabry-Perot method is no longer valid because the apparently wider waveguides should have lower loss than narrow waveguides. The losses of single-mode waveguides with widths of 4, 5, 7 μm , increase dramatically with decreasing waveguide width, which indicates that the sidewall roughness is still a major source of the waveguide loss. The further reduction of the loss requires the redesign of new waveguide structures to reduce the scattering from the sidewall roughness. The losses are \sim 4-7 dB/cm. The lowest loss is obtained in single-mode waveguides with the greatest width, 7 μm , which is \sim 4.5 dB/cm. This loss is the lowest value yet reported for AlGaAs nonlinear waveguides.

In addition, the losses of the unpatterned waveguides with various widths are also plotted as comparison. The differences between the patterned and unpatterned waveguides are ~ 1 dB/cm, much smaller than the total waveguides loss. These differences can be accounted partially by the remaining template corrugation height of 22 nm. The template corrugation not only causes periodic light scattering, but also induces additional surface roughness in the patterned regions compared with the unpatterned region. Both effects lead to higher loss of the patterned waveguides. Nonetheless, the loss differences are small, which means that the remaining template corrugations are no longer the dominant source inducing the waveguides losses. At present, the likelihood to further reduce the template corrugation is small, thus other measures are needed to reduce the waveguide loss even for the unpatterned waveguides.

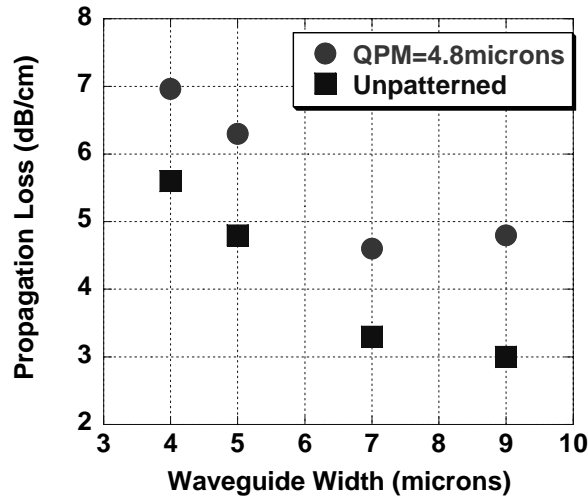


Figure 4-17 Loss of the QPM waveguides and the unpatterned waveguide grown on the low corrugation template

4. 7. 1. 2 Loss at second harmonic wavelength 775 nm

Since the waveguides are multimode at the wavelengths around 775 nm, the loss at the SH wavelength cannot be measured directly from the Fabry-Perot method. In addition, no convenient laser sources are available around 775 nm, we cannot estimate the loss by varying the waveguide length by cutting the waveguide step by step and measuring the transmission power.

Losses of QPM waveguides

In order to estimate the loss at the second harmonic wavelengths, we fabricated a 5-mm-long QPM waveguide, which contains five 1-mm long sections with various QPM periods; 4.6, 4.7, 4.8, 4.9 and 5.0 μm , as shown in figure 4-18a. The SHG tuning curve from this waveguide

has 5 QPM peaks, each peak corresponding to one QPM period. Assuming the loss, input fundamental power and SHG conversion efficiency are constant across the five phase-matching wavelengths, which is a reasonable assumption because the wavelength range is only 40 nm, the SHG power or the SHG conversion efficiency is expressed by the losses at both the fundamental wavelength and the SH wavelength, as follows:

$$\eta = \eta_0 \cdot \exp(-2\alpha_1 L - \alpha_2 (L_0 - L - \Delta L)) \quad 4.6$$

where η_0 is the conversion efficiency for a single 1-mm long QPM waveguide, α_1 is the loss at the fundamental wavelength, and α_2 is the loss at the second harmonic wavelength; L_0 is the total length of the waveguide, ΔL is the length of each section, and L is the position of the grating in the waveguide.

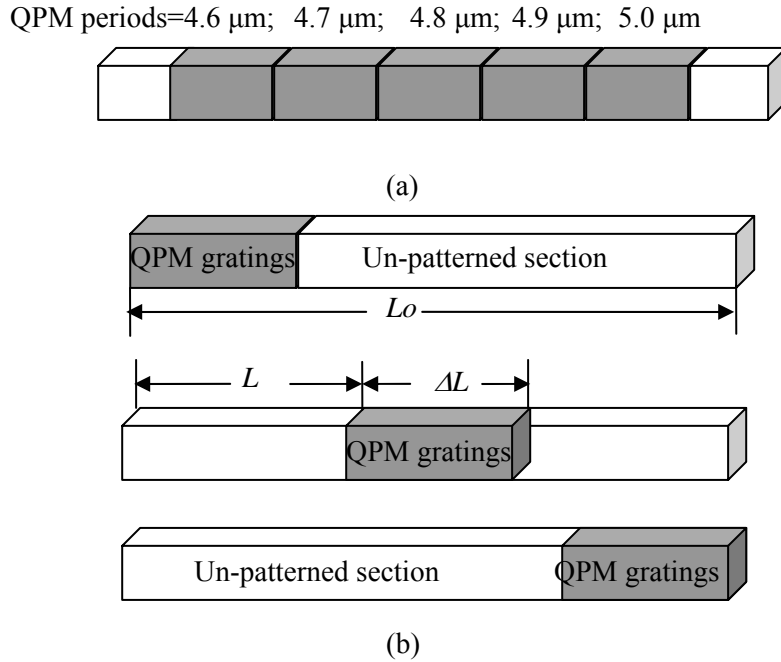


Figure 4-18 Waveguides layout for measuring the losses at 775 nm for both the patterned and unpatterned waveguides

From equation 4.6, we can obtain the relationship between the loss at the fundamental wavelength and the loss at the SH wavelength:

$$\text{Ln}(\eta / \eta_0) = (\alpha_2 - 2\alpha_1)L - \alpha_2 (L_0 - \Delta L) \quad 4.7$$

and $(\alpha_2 - 2\alpha_1)$ is just the slope of in the plot of the $\text{Ln}(\eta / \eta_0)$ vs L .

Given the value of α_1 measured using Fabry-Perot methods and the relationship obtained here, we can calculate the loss at the second harmonic generation wavelength. It is worth mentioning that the loss value obtained here is definitely not as accurate as the Fabry-Perot method, but it gives a close estimation of the real loss value. The accuracy depends on whether the coupling efficiency of the light into the waveguides and the losses are constant or not with changing wavelengths. Of course, the loss value is more accurate if the plot of $\text{Ln}(\eta/\eta_0)$ vs L is more linear.

Losses of unpatterned waveguides

The losses at 775-nm wavelength for the unpatterned waveguides are measured by similar methods. As shown in figure 4-18b, a 2-mm-long QPM grating is placed in the unpatterned waveguide at three locations, front, end and middle. The SHG conversion efficiency from the three waveguides vs the grating position can be expressed relative to the losses of unpatterned waveguides as:

$$\eta = \eta_0 \cdot \exp\left(-2\alpha_{1up}L - \alpha_{2up}(L_0 - L - \Delta L)\right) \quad 4.8$$

where α_{1up} is the loss of the unpatterned waveguides at 1550 nm and α_{2up} is the loss of the unpatterned waveguides at 775 nm. From equation 4.8, we obtain a similar linear equation for $\text{Ln}(\eta/\eta_0)$ vs the grating position L in the waveguides as shown in equation 4.9,

$$\text{Ln}(\eta/\eta_0) = (\alpha_{2up} - 2\alpha_{1up})L - \alpha_{2up}(L_0 - \Delta L) \quad 4.9$$

Again, the accuracy of the measured result depends on the variation of the coupling efficiency of the light into the waveguide. We assume a constant coupling efficiency can be achieved after we carefully align the sample position to obtain equal transmission power at fundamental wavelengths, which is a good approximation. Nonetheless, this method only gives a close estimation of the loss at the 775 nm.

Measurement results of the loss at 775 nm

The losses for the unpatterned waveguides are measured according to the method described above. Figure 4-19 shows a logarithmic plot of the SHG efficiency as a function of the positions of the 2-mm-long QPM gratings in an unpatterned waveguide.

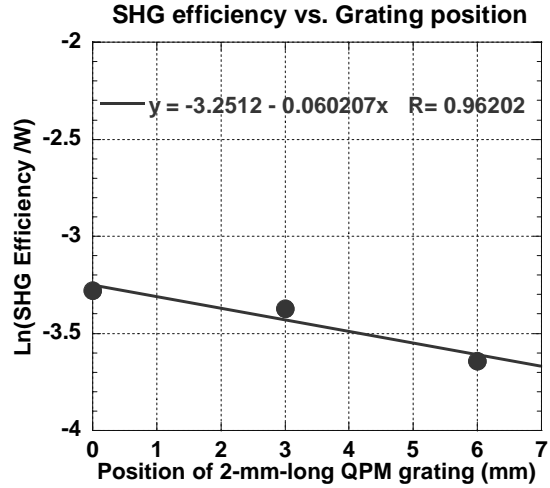


Figure 4-19 SHG conversion efficiency from the 2-mm-long QPM gratings at different locations in the plain waveguides

By fitting the loss parameters in the plot, we obtain:

$$(\alpha_{2up} - 2\alpha_{1up}) = -0.06207 \text{ mm}^{-1} \text{ or } (\alpha_{2up} - 2\alpha_{1up}) = -2 \text{ dB/cm}$$

The loss at 1550 nm is ~ 3.2 dB/cm measured by the Fabry-Perot method. Thus, the loss at 775 nm is $\sim 4\sim 5$ dB/cm, which is less than twice the loss at the fundamental wavelength.

Similarly, we obtained the loss at the SH wavelength in the patterned waveguides by fitting the parameters of the efficiency equation. Figure 4-20 shows the SHG conversion efficiency of the waveguides with five QPM gratings.

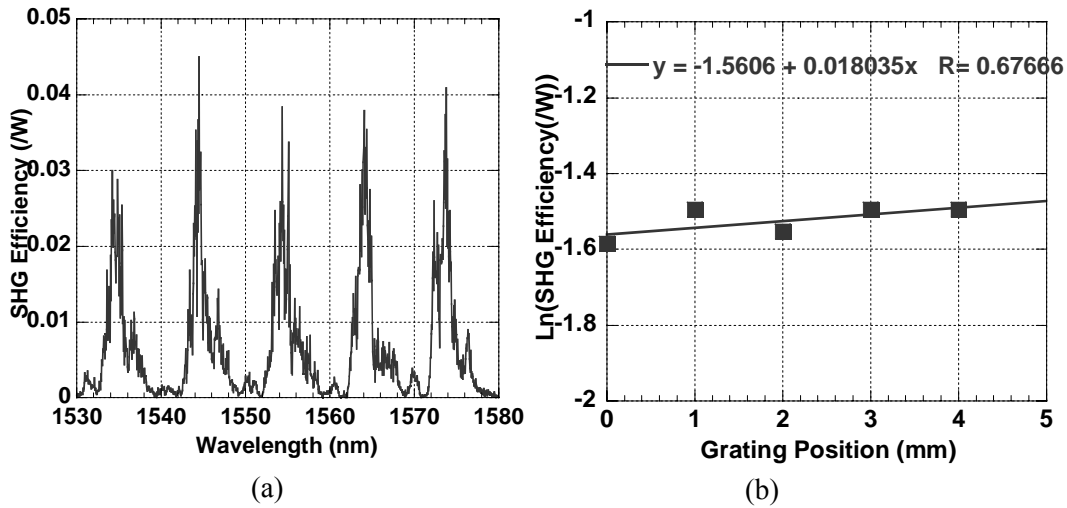


Figure 4-20 SHG conversion efficiency from the waveguides with five QPM periods. (a) SHG conversion efficiency vs input fundamental wavelength; (b) Logarithm plot of the SHG efficiency in a function of position

The SHG tuning curve is shown in figure 4-20a, where the conversion efficiency is recorded by tuning the fundamental wavelength. The tuning curve exhibits five phase-matching peaks with various intensities. Figure 4-20b is the plot of $\text{Ln}(\eta/\eta_0)$ vs the position of the gratings. Linear fitting gives a slope of 0.018035. Thus, based on equation 4.7, we obtain,

$$(\alpha_2 - 2\alpha_1) = 0.018035 \text{ mm}^{-1} \text{ or } (\alpha_2 - 2\alpha_1) = 0.78 \text{ dB/cm}$$

Given $\alpha_1 = 4.5 \text{ dB/cm}$ at 1550 nm measured using Fabry-Perot methods, we get the loss at 775 nm, α_2 is $\sim 9.78 \text{ dB/cm}$.

Compared with the loss differences at the fundamental wavelengths, the loss differences at the SH wavelengths are much higher between the QPM waveguides and the unpatterned waveguides. This indicates that the periodic scattering due to the template corrugation is more severe at shorter wavelengths than at longer wavelengths. Although this loss value has been dramatically improved compared with the earlier work, which is typically above 20dB/cm at the second harmonic wavelength, more work is required to further reduce the loss value at shorter wavelengths in order to utilize the AlGaAs QPM waveguides at the communication wavelengths. Nevertheless, QPM waveguides with all the interacting wavelengths in the mid-infrared range can be built based on the loss values obtained here.

4. 7. 2 Second harmonic generation (SHG) measurement

4. 7. 2. 1 Experimental setup

The waveguides are cleaved into samples with various lengths to measure the second harmonic generation. Figure 4-21 illustrates the experimental setup for the optical measurements. A fiber-coupled tunable external-cavity-diode laser (tunable around 1.55 μm) amplified by an erbium doped fiber amplifier (EDFA) is used as the pump source. A polarizer and an in-line polarization controller control the polarization before the light is coupled into the waveguide. With a beam sampler monitoring the input power, the beam is coupled in and out of the waveguide using high numerical aperture (NA=0.65) aspheric lenses. Type-I SHG is tested with the fundamental input TE-polarized and SH output TM-polarized. We record SH power after the output coupling lens as a function of the wavelength using a lock-in amplifier to increase the signal-to-noise ratio.

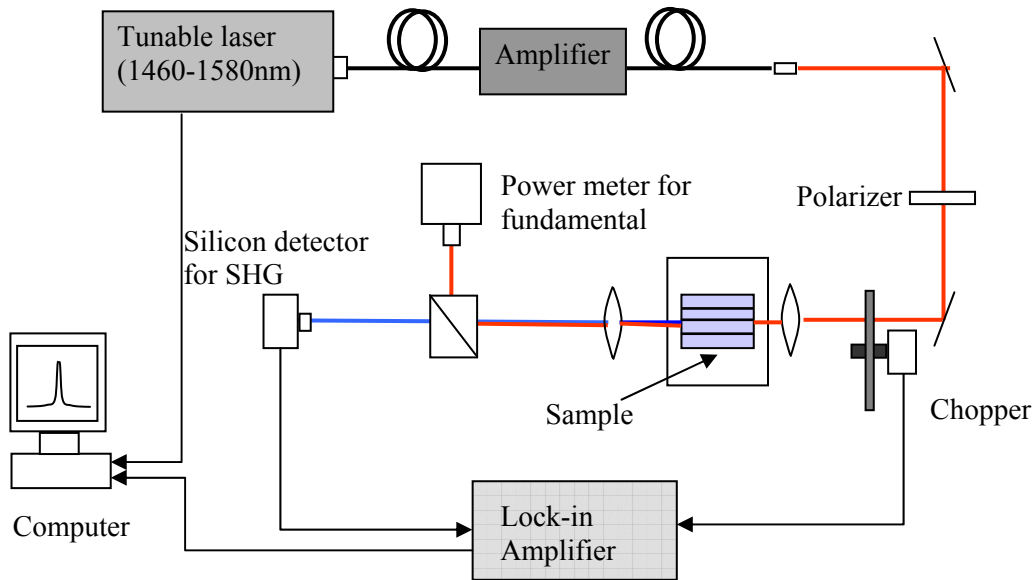


Figure 4-21 Optical setup for measuring loss and second harmonic generation

4. 7. 2. 2 SHG tuning curve

The SHG efficiency is measured by measuring the SHG tuning curve. The SHG tuning curve is obtained by recording the second harmonic power while tuning the wavelength of the fundamental input. Figure 4-22 shows a typical spectrum of the SHG tuning curve. The length of the waveguide measured is 8 mm, and the width is 7 μm . The input power recorded is roughly the power in front of the input facet of the waveguides. The actual power of the fundamental wave coupled into the waveguides is just a fraction of the recorded value. The SH power recorded is also the power that exits the waveguide and again, this power is just a fraction of the actual SH power generated because of the Fresnel reflection of the output facet. The SHG tuning curve exhibits sinc^2 characteristics with clear side-peaks, which are approximately symmetric, following theoretical expectations. The phase-matching peak is around 1652.9 nm, away from our nominal design. We attribute the shift of the peak wavelength to growth-rate-drifting during a long MBE growth run. The actual Al-composition in the waveguide core is $\sim 65\%$ instead of 67% as the designed value, and the Al-composition in the cladding is $\sim 68\%$ rather than 70%. In addition to the behavior of the Sinc^2 function, there are fringes added to the tuning curve. Those fringes are Fabry-Perot fringes from a cavity which formed by the two end facets.

In figure 4-22, the input power is ~ 7.8 mW, and the highest SH power is ~ 5.9 μW , which has been enhanced because of the Fabry-Perot cavity. To precisely estimate the peak-SH power generated with 7.8-mW fundamental input, the Fabry-Perot fringes must be removed

using a Fourier transform. This gives a peak power at around $\sim 4.8 \mu\text{W}$.

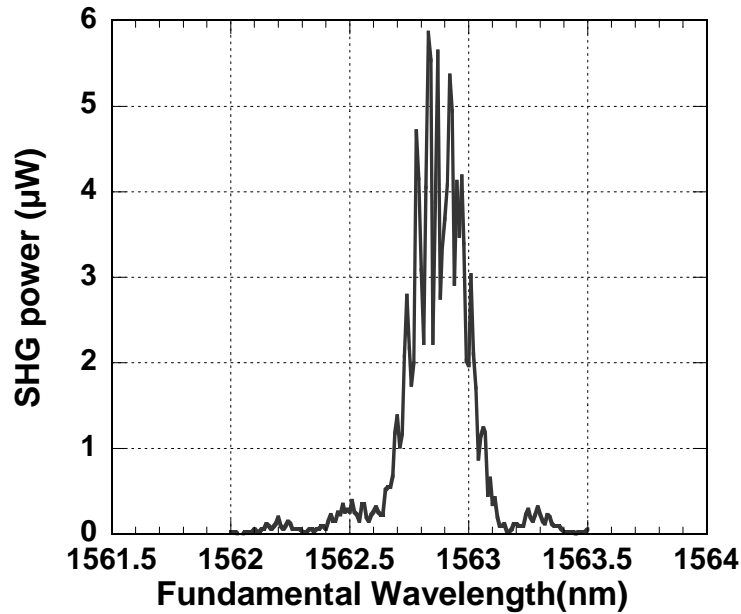


Figure 4-22 SHG tuning curve of an 8-mm long QPM waveguide

The SHG tuning curves with various fundamental input powers were recorded. The SHG power and the fundamental input power are plotted logarithmically, as shown in Figure 4-23. The plot exhibits linear behavior with a slope ~ 2.0 , indicating the SH power is proportional to the square of the input power. This result again follows theory. In addition to the linear behavior, the highest SH power recorded is $\sim 2 \text{ mW}$ under cw-operation. The peaks shift to longer wavelengths under high fundamental input power, indicating Joule heating plays a role.

4. 7. 2. 3 SHG efficiency estimation

To estimate the SHG efficiency, we need to consider the modal coupling coefficient and the Fresnel reflection of the fundamental wave at the input facet, as well as the Fresnel reflection of the SH wave at the output facet. The waveguide is designed to produce highest modal coupling efficiency. However, the modal coupling efficiency is not as high as expected because of the large beam size in front of the input facet. The coupling efficiency is estimated roughly by measuring the transmission of short $\sim 1\text{-mm}$ -long unpatterned waveguides,.

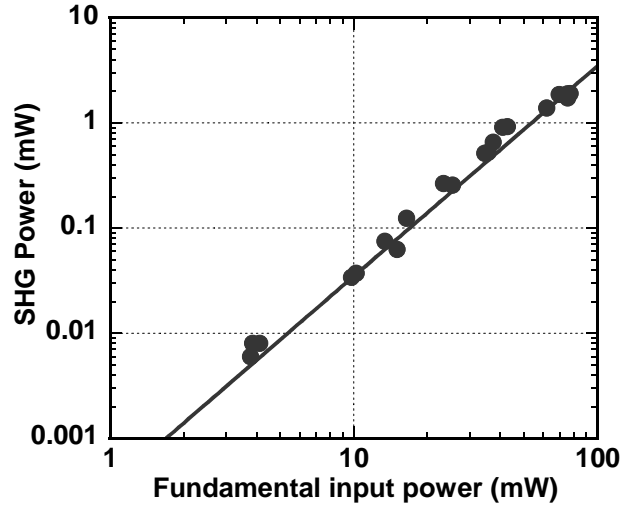


Figure 4-23 Relationship of SHG power and fundamental input power

Equation 4.10 shows the equation used to estimate the coupling coefficient, $\eta_{Coupling}$, for the waveguides with various widths.

$$\frac{P_{Out}}{P_{In}} = (1 - R_1) \cdot (1 - R_2) \cdot \eta_{Coupling} \cdot \exp(-\alpha L) \quad 4.10$$

where, $R_{1,2}$ are the Fresnel reflection coefficients at each facet, and $\exp(-\alpha L)$ is the reduction due to the loss when light propagates through the waveguide. This method of course is not accurate, varying with the value of the reflection and waveguide loss. The waveguide loss is estimated from Fabry-Perot methods and it is not accurate itself. However, if the waveguide length is very small, around 1 mm, and the waveguide loss is not too high, $\sim 2\text{-}3$ dB/cm, the variation of the waveguide loss will have a small effect on the accuracy of the evaluation of the coupling coefficient. Thus, the coupling coefficient measured based on this method is not far from the real value.

Table 4-1 lists the coupling coefficient for the waveguides with different widths. It shows that when the width is greater than 10 μm , the coupling coefficient is almost constant, while the coupling coefficient is reduced dramatically when the waveguide widths is $< 8 \mu\text{m}$, indicating the input beam size is $\sim 8\text{-}10 \mu\text{m}$.

Table 4-2 Coupling coefficient for the waveguides with various widths

Width =	6 μm	8 μm	10 μm	12 μm	14 μm
Coupling coefficient	51%	66%	75%	75%	75%

The Fresnel reflection coefficients are calculated based on the modal effective index as expressed earlier in equation 4.5. Thus, the reflection coefficient of the fundamental wave is about 0.255, and is ~ 0.275 for the SH wave.

After considering all of the factors mentioned above, the fundamental power coupled into the waveguide is ~ 3.9 mW, $\sim 50\%$ of the power in front of the input facet, and the generated SH power is ~ 6.6 μ W before exiting the waveguides. The internal SHG conversion efficiency

is thus calculated as $\eta_{SHG} = \frac{P_{SHG}}{P_{IN}^2} = \sim 43 \text{ \%W}^{-1}$, which is record high and about twice as our

previous report[109].

Let us now compare this measurement with the theoretical calculation. The normalized internal SHG conversion efficiency, η_{Norm} , in a lossless waveguide is $\sim 420 \text{ \%W-cm}^2$. Thus, the ideal efficiency in an 8-mm long lossless waveguide is 268 \%/W . The differences between the ideal value and the measurement are mostly due to waveguide losses. The theoretical SHG efficiency in a lossy waveguide is calculated to be $\sim 50 \text{ \%W}$ based on equation 2.16, with a loss of 4.5 dB/cm at the fundamental wave and 9.7 dB/cm at the SH wave. We still obtained a measurement efficiency lower than the theoretical calculation including losses. We believe the offset of the duty cycle away from 50% accounts for this discrepancy. Due to the lithography accuracy and over-etching during the process, the adjacent domains are not equal, thus reducing the maximum conversion efficiency. The widths of two adjacent domains are 33% and 67% of the QPM period respectively. The reduction of the conversion efficiency is calculated by integrating over the coupling equation as illustrated in equation 4.11.

$$\frac{P_{(f,1-f)}}{P_{(0.5-0.5)}} = \frac{\left| \int_0^{\frac{2\pi}{\Delta k} f} \exp(-i \cdot \Delta k \cdot L) dL - \int_{\frac{2\pi}{\Delta k} f}^{\frac{2\pi}{\Delta k}} \exp(-i \cdot \Delta k \cdot L) dL \right|^2}{\left| \int_0^{\frac{\pi}{\Delta k}} \exp(-i \cdot \Delta k \cdot L) dL - \int_{\frac{\pi}{\Delta k}}^{\frac{2\pi}{\Delta k}} \exp(-i \cdot \Delta k \cdot L) dL \right|^2} \quad 4.11$$

where f is the duty-cycle factor.

Equation 4.11 gives a SHG power of $\sin^2(\pi f)$ of the ideal SHG power. Thus, a duty-cycle of 33% results in a reduction to 76% of the expected SHG power. With this correction, the theory calculation is close to the measurement.

4. 7. 2. 4 SHG efficiency vs. length

The SHG efficiencies of the waveguides with various lengths are also measured for waveguides with various losses. Figure 4-24 shows the plot of SHG efficiencies vs waveguide lengths that are fabricated on two different samples. Sample #1869 is grown on the low corrugation template with the lowest loss, ~ 4.5 dB/cm at $1.55 \mu\text{m}$ and ~ 9.7 dB/cm at 775 nm . Sample #1823 has higher loss due to a larger template corrugation and the existence of interfacial grooves, with losses of ~ 7.5 dB/cm at $1.55 \mu\text{m}$ and ~ 16 dB/cm at 775 nm . The solid circles and diamonds are the measurements and the curves are the curve fits with the given loss values. The longest waveguide measured is 8 mm. From the plot, we clearly see that the dependence of SHG efficiency on length coincides very well with theoretical predications. The optimum length to obtain highest conversion efficiency is ~ 9 mm for sample #1869 and ~ 5 mm for sample #1823, clearly illustrating the strong dependence on loss.

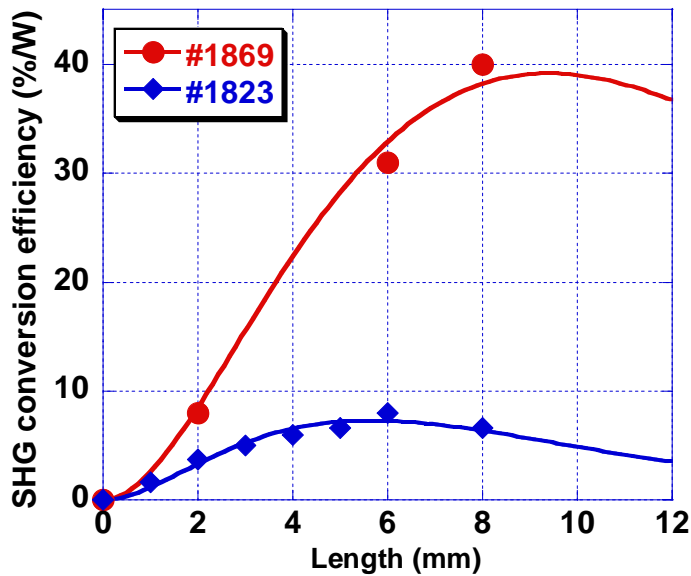


Figure 4-24 Dependence of SHG conversion efficiency on sample length

4. 8 Conclusion

In conclusion of this chapter, the effects of growth conditions of the GaAs/AlGaAs on orientation-pattered regrowth have been studied. The main contribution is that we found the limiting factor for the waveguide loss comes from regrowth-induced v-groove corrugations, which occur at the domain boundaries. Although the template corrugation itself also plays an important role, the reduction of template corrugation becomes significant only after the v-

grooves are eliminated. By studying the mechanism of the v-groove formation, we proposed that the v-grooves are caused by the existence of the APBs since similar v-grooves are not observed in regrowth on ordinary lithographically patterned, but not orientation-patterned substrates. All the growth parameters that enhance the diffusion of adatoms induce v-groove formation. Based on those studies, optimized growth conditions were obtained to eliminate the v-grooves. The waveguides grown under those conditions on low-corrugation templates introduced in this chapter generated waveguides with record low loss and record high conversion efficiency.

The loss at both fundamental wavelengths and SH wavelengths are measured. The loss at the SH wavelengths is measured using a parameter fitting approach developed in this dissertation work, yielding a self-consistent result. The internal SHG conversion efficiency is much higher than all previous research on AlGaAs nonlinear waveguides.

Compared with LiNbO₃, the conversion efficiency is still low, and loss is still high. The loss of LiNbO₃ waveguides is typically ~0.1dB/cm and the conversion efficiency is greater than 1000%/W. However, the work in this dissertation has solved most of the fundamental materials growth problems. Continuing improvement is possible by optimizing the waveguide structure design, and fabrication. It is highly possibly to fabricate QPM AlGaAs waveguides with losses lower than 1dB/cm. Since GaAs and AlGaAs have much higher nonlinear coefficients than LiNbO₃, an AlGaAs waveguide with loss lower than 1dB/cm could yield a conversion-efficiency comparable to that of LiNbO₃. In addition to the possible high conversion efficiency, AlGaAs and GaAs have a broader transparent range than LiNbO₃. It is possible to fabricate waveguides operating in the mid-IR range where LiNbO₃ cannot. Since the losses scale down as the wavelength increases, it is possible to fabricate GaAs QPM waveguides for mid-IR generation without additional fabrication improvement. Finally GaAs or AlGaAs QPM waveguides are of the same materials as the pump lasers, thus making possible an entirely monolithic integrated IR source. Thus, the realization of practical AlGaAs nonlinear waveguides for a variety of applications in the future is highly promising.

Chapter 5 GROWTH OF OP-GaP TEMPLATE

5.1 Introduction

A new materials system is also investigated in this dissertation work, that is, orientation-patterned GaP (OP-GaP). GaP has potentially even more attractive properties for nonlinear optics than GaAs. GaP has very high thermal conductivity (110 W/m-K), which is several orders of magnitude higher than most other nonlinear crystals and also twice that of GaAs. This large thermal conductivity allows efficient heat extraction so that high operating power is possible. It also has a very broad transparency range (0.6~11 μ m) and a very low absorption coefficient, particularly in the visible and near-IR region. This minimizes two-photon absorption, which is significant only for photon energies greater than half the bandgap. Thus, nonlinear optical devices based on GaP allow very high pump input power in the near-IR wavelength range so that it can take the advantage of current highly developed semiconductor lasers. In addition to its thermal properties and transparency, GaP also has a large nonlinear coefficient, $\sim 40\text{pm/V}$, and the device efficiency is not compromised. These properties make GaP a potentially ideal material system for nonlinear optical devices under high power operation.

Figure 5-1 shows a theoretical plot of the wavelengths generated through OPO processes as a function of the coherence length for various materials based on literature dispersion relations[110]. Several materials systems are plotted together as a comparison for a 2- μ m pump wavelength. As illustrated, the curve for GaP is almost vertical. This indicates that GaP devices with a proper QPM period can generate irradiation with a very broad spectrum without tuning the QPM periods or other parameters. The output spectrum can possibly extend from $\sim 3\mu\text{m}$ up to 10 μm . Based on this property, a variety of interesting OPO-based mid-IR sources can be built, including spectrally broadband, rapidly tunable and ultrafast mid-IR sources.

The success of OP-GaAs provides an excellent foundation to explore the possibility of fabricating OP-GaP films. Hopefully the approach to produce orientation inversion for OP-GaAs can be applied to the OP-GaP system. Similar to GaAs growth on Ge, in order to engineer GaP orientation, we need to find a group IV element which lattice matches to GaP. Thanks to the Mother Nature, we have a readily available material, Si, which is not only the foundation of the semiconductor industry, but an ideal material for this application. The

lattice mismatch of GaP and Si is $\sim 0.37\%$. Although this mismatch is much larger than that of GaAs and Ge, it allows growth of a sufficiently thick epitaxial film for a fabrication process similar to the GaAs/Ge system without serious stress in the film.

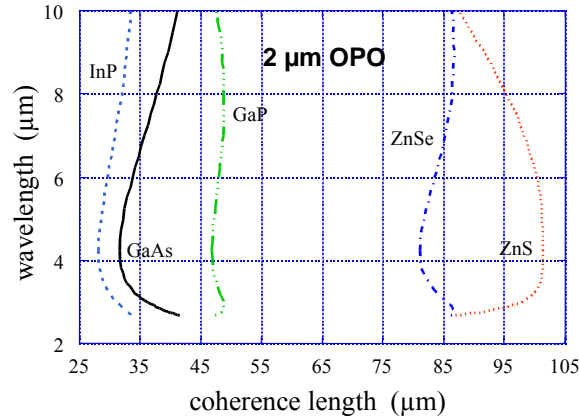


Figure 5-1 Phasematching for 2 μm -pumped OPOs in zincblende semiconductors. The vertical extent of GaP indicates a nearly wavelength independent coherence length and very wide phasematching bandwidth

In contrast to OP-GaAs growth, where the growth is carried out on GaAs substrates and a thin Ge layer is used, if we can obtain two distinct single-phase GaP layers on Si, we can fabricate OP-GaP film on Si substrates. Several benefits can be achieved for OP-GaP on Si. First, the low-cost and availability of Si substrates with various sizes, allow us to develop nonlinear devices with low cost, compared to using expensive GaP substrates. Second, the high thermal conductivity of Si substrates helps with heat extraction, benefiting high power operation devices. Third, Si substrates are much stronger, and can withstand mechanical handling, increasing device yield. In addition, if nonlinear wave-guiding devices can be fabricated on Si, or even conventional GaP waveguides can be fabricated on a Si substrate, there becomes the possibility for integrating optoelectronic devices with electronic devices. Other possibilities would also make this growth desirable, such as GaP light emitting devices, quantum dot laser devices on Si based on growth of GaP on Si. However, compared with the growth of GaAs on Ge substrates or a Ge thin film, which has been extensively studied, the growth of GaP on Si is not well understood or controlled.

5.2 Review on GaP growth on Si and its challenges

The growth of GaP on Si attracted some research interest in 1980s, for the fabrication of optoelectronic devices or high-speed electronic devices on Si. However, no impressive results

were ever achieved during this period. The research was then focused on the electronic properties of GaP on Si and the properties of GaP/Si heterojunctions[111]. The epitaxial film quality, in terms of the surface roughness and defect density were not satisfactory[111-117].

The earliest study of GaP growth on Si by solid source MBE was carried out by Wright, et al[114-116]. They mostly used the (211)-oriented Si substrates for the growth since the nucleation of GaP on (211) Si would not cause antiphase domain defects. Single orientation GaP was obtained, however, the material quality were poor. Under all the growth temperatures investigated from 300 to 650°C, very spotty RHEED patterns were observed, which means the surface is extremely rough. They found that the P_2/Ga flux ratio had a direct effect on the surface roughness, and a low P_2/Ga ratio gave the best surface quality, though the surface was still quite rough[115]. Other GaP growth on Si was mostly carried out using OMCVD or gas source MBE. Nonetheless, most of the work struggled with reducing the defects and obtaining a smooth surface. No GaP electronic or optoelectronic devices were ever built on Si substrates.

The limited success of the all previous work indicates the growth of GaP on Si is more difficult than GaAs on Ge. In general, the growth exhibits 3-D growth characteristics, even with a very thin layer deposition. Even under MEE or ALE growth, a rapid transition from a 2-D growth to a 3-D growth regime occurs after several-monolayers GaP deposition. The 3-D growth mode leads to the generation of various types of defects, where dislocations and twins are the most common ones, and creates a very rough surface. It is expected the bonding between Ga and P is very strong, so that the mobility of the Ga adatoms is low. Under normal growth temperatures, the surface cannot be smoothed, leaving a rough growth. A very high temperature is required to obtain smooth growth. However, phosphorus-desorption occurs at high growth temperatures. On the other hand, the adsorption efficiency of phosphorus on Si is very low, and it is very difficult to form a continuous P layer on Si, as required for polar-on-nonpolar growth, thus APDs are far more likely to form. A low growth temperature is required to increase the surface coverage of P on Si. However, growth at low temperature results in an extremely rough surface. In addition, the thermal expansion mismatch is also a problem, in that defects are generated during the cooling stages.

Fortunately, our application aims at special properties of GaP, engineering GaP orientation, especially for developing the template structure used for thick film deposition. As long as the OP-GaP structure can be fabricated, the film surface roughness is not as critical because the devices based on bulk materials don't require such smooth surfaces. Even for waveguide applications, the root-mean-square (rms) of the surface roughness at several

nanometers is still acceptable compared with the dimension of the waveguide core, which is usually around $\sim 1\mu\text{m}$, though a smoother interface definitely reduces the loss.

Thus, the goal of the growth study is to find the growth conditions to generate GaP with single orientations. If we can successfully obtain one single-oriented GaP domain on Si, we can use the same process as OP-GaAs, where GaP/Si/GaP heterostructures can be grown on GaP substrates. If we can find two growth conditions, which can produce controlled single-phase GaP with both orientations, we can simply fabricate OP-GaP on Si substrates and take the advantages of the Si substrates.

In this chapter, we will first describe how we investigated the growth condition of single-phase GaP on Si and the preliminary results. The phases are controlled by controlling growth temperature, prelayers and V/III flux ratio. RHEED is used as the in-situ monitor and first evidence for phase identification. Anisotropic ex-situ etching reveals the sidewall profile that identifies the phase orientation. AFM are carried out to characterize the crystalline quality and surface morphology. We will then describe how to improve the surface smoothness. In the end, we describe the first fabrication and results of OP-GaP templates.

5.3 Single-phase GaP growth on Si

5.3.1 GaP phase control

As discussed during the study of GaAs growth on Ge, the phases can be controlled by controlling the growth temperatures, V/III flux ratio, prelayers and surface structures. We hope these conclusions can be applied to GaP growth on Si as well. GaP films were grown in a Varian GEN II MBE system. P_2 flux was provided by a GaP decomposition cell with a P_2 partial pressure as high as 99%[118,119]. The beam flux is controlled by a mechanical shutter, unlike As_2 flux control, where the flux is controlled by a valve. The on/off switching of P_2 is not as rapid as As flux, and a background pressure of P_2 exists even when the shutter is closed. The remaining background P_2 flux adds difficulties to the growth control and we found the P-exposure history of the Si surfaces dramatically affects the final results, which is different from GaAs growth on Ge, where the exposure history effect is not as strong.

Phosphorous doped Si substrates oriented 4° off (001) towards the $\langle 110 \rangle$ direction were used to test the growth. As we learned from the GaAs growth on Ge, a higher offcut angle fosters the preferential growth of one phase over another, and typically 4° off substrates are used. Thus, we adopted a 4° offcut as well.

The Si substrates were cleaned using a modified RCA clean technique (10 minutes in

H₂SO₄:H₂O₂ (4:1) at 90°C; 10 minutes in H₂O:HCl:H₂O₂ (5:1:1) at 70°C; 15 seconds in HF (50:1) at room temperature; Spin Dry). A final HF:DI water(1:100) solution dip for 10 seconds was performed right before loading into the MBE pre-chamber with a pressure about 1×10^{-8} Torr. After baking, the wafers were transferred to MBE growth chamber with a pressure below 2.0×10^{-10} Torr. A 30-min thermal desorption of oxide was performed at 850-1000°C before growth was initiated. Typically, a strong 2×1 RHEED pattern mixed with a weak 1×2 RHEED pattern was observed before growth. This indicates that the Si surface has mixed surface domains under these growth conditions.

5.3.1.1 Exposure history

Growth is initiated with exposure of the surface to P₂ or Ga; P₂ is mostly used because of the P₂ background. We found that the growth results vary strongly with how the thermal oxide-desorption is carried out and how the P₂ exposure is controlled, and even between different growth runs with nominally identical growth parameters. The operational characteristic of the GaP-decomposition source adds to the complexity. The P₂ flux is controlled only by temperature, however, the flux is not constant during the growth or between different growths. The flux fluctuates a lot during the growth. In order to get a stable flux, we wait for a long time before starting the growth, but the stability is still not satisfactory. In addition, because the flux on/off ratio is controlled only by a mechanical shutter, the flux with the shutter closed is about 1/5 of the flux with the shutter open, so an inadvertent P₂ exposure occurs before the P₂ shutter is opened.

Unlike As on Ge surfaces, where the interaction is more easily controlled, the interaction of As or P on Si is very complicated. Let us take the interaction of As with Si as an example. It has been discovered that the configuration of As on the Si surface is determined by how the Si surface is exposed to the As flux. A study was carried out by Bringans et al[120], in which four different exposure methods were used and the As reconstruction on the Si surface was measured by low energy electron diffraction (LEED). A (2×1) reconstruction means that the As-dimers on Si surfaces are parallel to the steps, denoted as As_{||}. A (1×2) reconstruction means that the As-dimers on Si form bonds perpendicular to the steps, denoted as As_⊥. The ratio of LEED intensity of (2×1) to (1×2) indicates the fraction of As_{||} and As_⊥.

Before the As exposure, the Si surface is annealed at high temperature to form a single-domain Si surface, where bilayer steps dominate. Then As- exposure is carried out with four methods.

Method (a): the substrate temperature is raised from room temperature (RT) to the

exposure temperature (T_e), and is held at this temperature for a fixed time, then is reduced back to RT. During the whole process, the As pressure is kept at P_{As} .

Method (b): the substrate is heated to T_e while the As flux is off. At T_e , the As flux is supplied for a fixed time, and then the substrate temperature is reduced to RT.

Method (c): the substrate temperature is reduced from high temperature to T_e while the As pressure is constant at P_{As} . The temperature is held at T_e for a fixed time, and then is reduced to RT.

Method (d): the As exposure is carried out at RT, and the substrate is then annealed at T_e without As protection.

Bringans's study shows that the As configurations vary with the exposure approach at the same As-exposure temperatures. The As_{\parallel} is dominant in method (b) at $\sim 500^{\circ}C$, while the As_{\perp} is dominant with RT-exposure and $\sim 600^{\circ}C$ anneal. In general, the As-reconfiguration determines the final phase GaAs grown on Si.

Although the study is about As exposure on Si, we believe a similar complexity exists for P exposure on Si surfaces. To investigate the effect of P-exposure history, we carried out a series growths using various exposure methods, similar to Bringan's methods. The P-exposure is carried out using three methods.

Approach 1: no deliberate P_2 -exposure history control

Under the first growth condition, the P_2 -exposure is not controlled to avoid the P_2 background pressure. The thermal oxide-desorption is carried out in the III-V growth chamber where a high background P-pressure is present during the thermal desorption. Thus, we don't know the exact temperature at which the P-exposure occurs. GaP with a total thickness of 500\AA was grown, and the phase of GaP identified by AFM.

Figure 5-2 shows AFM images of GaP films grown under this condition. First, a texture-like pattern is observed from the AFM images. This texture is typical for GaP growth under certain growth conditions and it has been observed to be along the [1-10] direction. Thus, the GaP with two separate orientations has opposite texture directions. Based on this, we can check whether the GaP is in mixed phase or not. Figure 5-3 shows the AFM images of the films grown at various temperatures. Obviously the textures are along both directions, indicating mixed phases are obtained.

In addition to the texture directions, the AFM images also show that the antiphase domains have different thickness. This indicates that one phase has much slower growth rate than the other phase, and this observation is in agreement with the conclusion of GaAs on Ge.

Basically, single phase GaP can not be achieved under this P-exposure condition, independent of growth temperature. Obviously, controlled P₂-exposure is necessary.

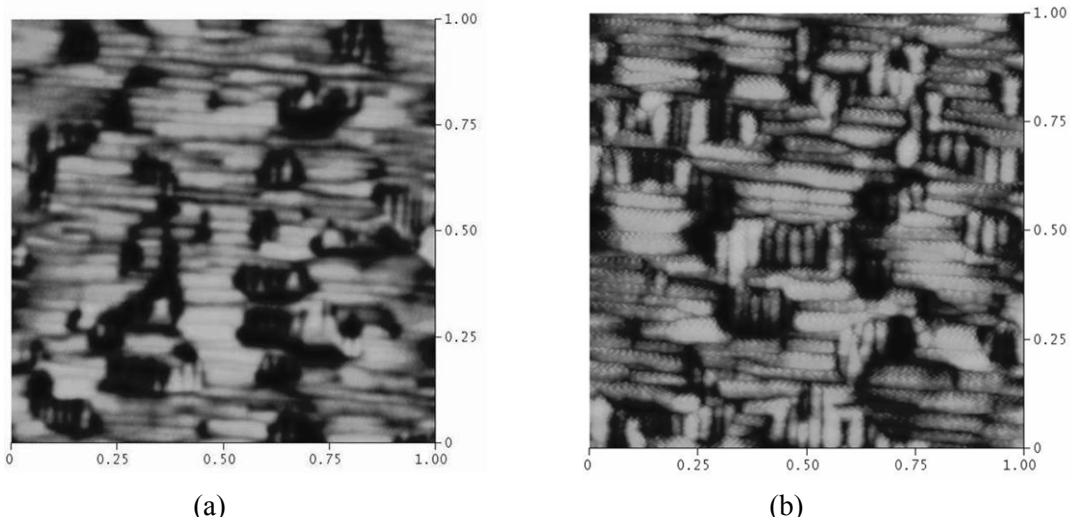


**Figure 5-2 AFM images of GaP on Si without exposure control
a: Tg=510°C; b: Tg=350°C**

Approach 2: P₂-exposure after substrate temperatures are stable

In this approach, the thermal oxide-desorption is carried out in a separate MBE chamber dedicated to Si-Ge growth. Thus, no As/P background pressure is present during the oxide blow off process. The substrate is then cooled to RT and transferred to III-V growth chamber through an ultra-high-vacuum transfer tube. In the III-V growth chamber, the substrates are heated up to various exposure temperatures (T_e).

The GaP-decomposition source is heated up after the substrate temperature is stabilized. The P-exposure is then carried out and the growth is started with P-prelayer. About 10-monolayer GaP is deposited at this exposure temperatures and the subsequent growth is carried out at ~550°C. Again, GaP with a total thickness ~500Å is grown.

Figure 5-3 shows the AFM image of GaP grown with various P-exposure temperatures. Under the temperature investigated, the AFM images show a single texture direction, indicating the GaP growth is dominated by one orientation. Figure 5-3 also shows a texture-morphology different from Figure 5-2, and this is mostly due to variation of growth rate and V/III BEP ratio.

In addition, under most of the exposure temperature investigated, the texture directions are the same, though APDs exist at some exposure temperatures. The APD sizes are very small, and particularly, no APDs are observed for the exposure temperature at 550°C, which indicates that a higher exposure temperature is more likely to yield single-phase GaP.

However, when we further increase the exposure temperature to 600°C, the films are in mixed phases. This is probably because P-desorption occurs at the Si surface at higher temperature. In general, our observation partially agrees with Bringan's results of As exposure using method #2.

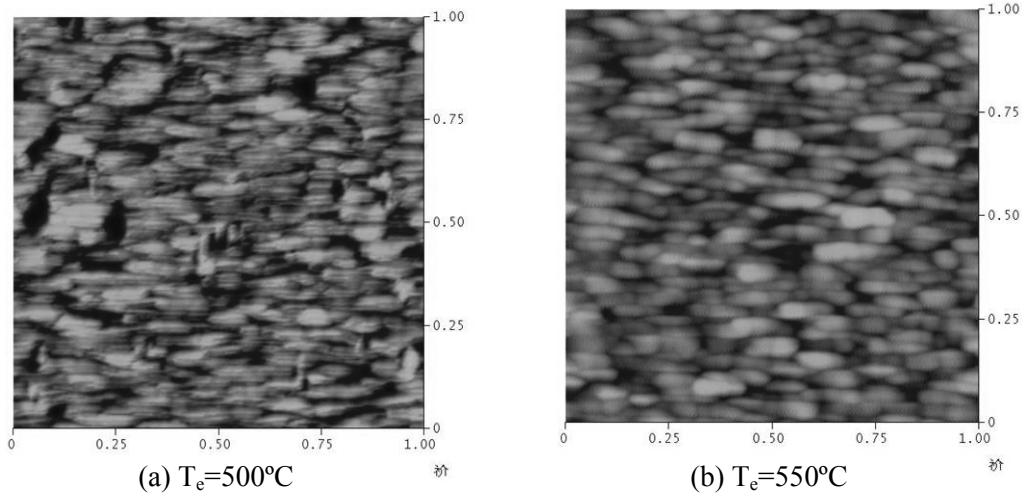


**Figure 5-3 AFM images of GaP on Si vs P_2 -exposure temperature
 --- P_2 -exposure occurs at the exposure temperatures**

Approach 3: P_2 -exposure when temperature reduces after oxide-desorption

The thermal oxide-desorption is carried out in the same III-V growth chamber. After the oxide desorption, the P -flux is supplied and the substrates are cooled to the exposure temperature with P_2 -exposure. About 10-monolayer GaP is deposited at this exposure temperature and the subsequent growth is carried out at $\sim 550^\circ\text{C}$. Again, GaP with a total thickness $\sim 500\text{\AA}$ is grown. Figure 5-4 shows the AFM images for the GaP film grown under this growth condition. This growth shows similar effects that all texture directions are along one direction. However, the texture direction is different from what have been observed from Figure 5-3.

This indicates that different P_2 -exposure control does affect the final growth results. Two exposure approaches result in two different orientations with identical growth-conditions. Thus, it is highly likely to produce two distinct GaP single phase on Si by proper control of the exposure and nucleation conditions.

In addition, GaP grown with the exposure temperature around 200-300°C is not as straightforward as the exposure temperatures at 500-550°C. No definite conclusions can be made from this observation. Since it varies with the growth run, the interaction of P and Si surface is likely very complicated around this temperature range. The exact reason is not well

understood and the operation of the GaP-decomposition source adds significantly to this complexity.

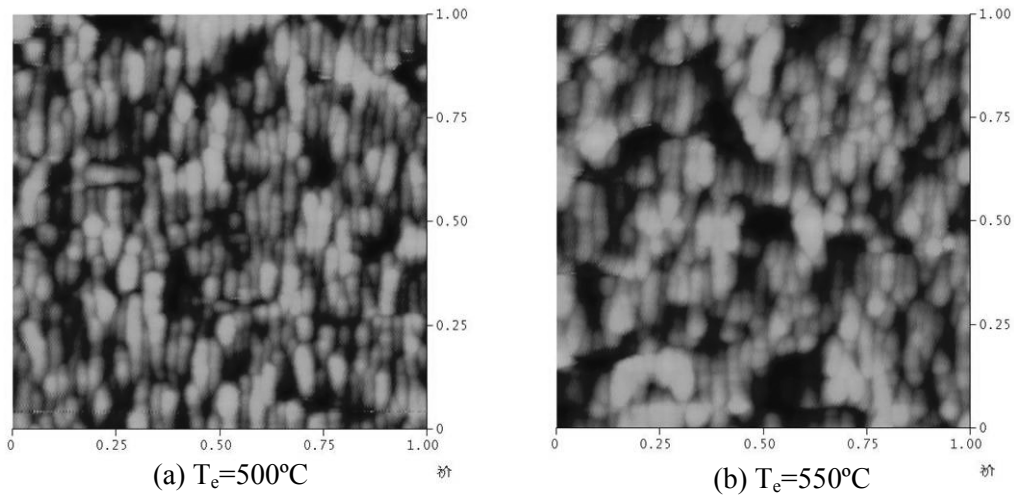


**Figure 5-4 AFM images of GaP on Si vs P_2 -exposure temperature
 P_2 -exposure starts at high temperatures**

Since P_2 exposure control is essential for GaP growth on Si, it is necessary to have a valved-phosphorus source to provide the P flux. A valved-phosphorus cell can more accurately control the phosphorus pressure and inadvertent phosphorus-exposure is unlikely to happen.

5.3.1.2 Growth temperatures

We also found the nucleation temperature (usually the same as the P-exposure temperature, but sometimes a Ga prelayer were used) very important to determine the GaP orientation, similar to the growth of GaAs on Ge. In this section, the second approach above is used to control the P-exposure. The GaP is grown using two methods. The first one is to directly grow GaP at the exposure temperatures with proper P_2 /Ga BEP flux ratio. The temperature varies from 300 to 600°C and P_2 /Ga BEP flux ratio varies from 3 to 10 times. The second method is a two-step growth, mostly for low temperature nucleation. During the two-step growth, a thin nucleation layer was grown at a low temperature (about 200-350°), and then a thicker film was deposited at a higher temperature (around 700°C). The phases are determined from RHEED and from the sidewalls of patterned mesas after anisotropic chemical etching.

RHEED pattern

The orientation of GaP is monitored by RHEED during the growth. GaP exhibits a 2×4 GaP RHEED pattern under both low and high temperature growth, as already introduced, this indicates the film is close to single phase. As demonstrated in figure 5-5, due to the offset angle of the substrate, the Kikuchi lines will oscillate around the horizon when the substrate is rotating. The lines intersect either above or below the horizon when the electron beam is along the 4° misoriented direction (perpendicular to the steps), and intersect on the horizon when electron beam is perpendicular to the misoriented direction (parallel to the steps).

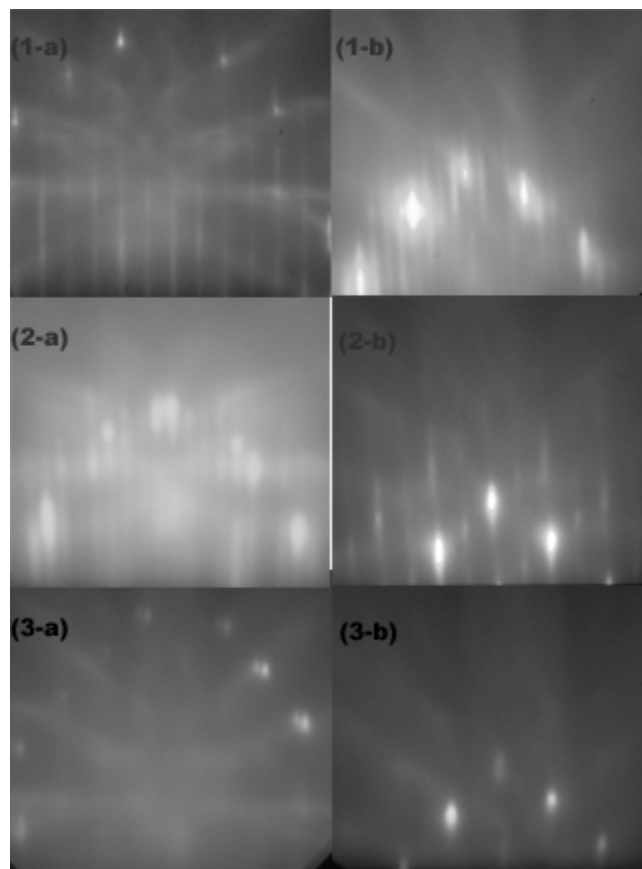


Figure 5-5 RHEED patterns of GaP grown on Si
a: Electron beam incident perpendicular to steps; b: Electron beam incident parallel to steps. (1): 575°C, one-step growth; (2) 350°C, two-step growth; (3) 350°C, one-step growth

The first row of the images in figure 5-5 show a 2×4 RHEED pattern at high growth temperature $T_s=575^\circ\text{C}$ with a low P/Ga flux ratio= $2.5\times$. The $2\times$ reconstruction is observed when the electron beam is along the misoriented direction, and the $4\times$ reconstruction is seen

after the substrate is rotated by 90°. The streaky characteristic of the RHEED pattern indicates the GaP surface is smooth under this growth condition.

As the growth temperature is decreased to $T_s=350^\circ\text{C}$, a 4×2 reconstruction is observed for the two-step growth. The the difference between RHEED patterns indicates that different phases are achieved at different temperatures as expected. However, a spotty RHEED patterned is observed for the single-step growth at this temperature, indicating the surface is very rough at this growth temperature.

Anisotropic etching result

In addition to examining the RHEED pattern, we further confirmed the phases using anisotropic etching of the GaP film. SEM was used to observe the sidewall profile after etching. A solution of $\text{HBr}:\text{H}_2\text{O}_2:\text{H}_2\text{O}=1:1:10$ was used due to its etching rate difference of (111)A and (111)B planes. The etching time was about 50 seconds for 4000\AA GaP on Si. Because the (111)A plane etches slowly, the sidewalls of the etching profile will be either obtuse or acute for the different GaP phases.

Figure 5-6 shows SEM pictures of the sidewall profiles under different growth temperatures and P/Ga flux ratios. At a low flux ratio of $2.5\times$, the sidewall profiles are acute for temperatures higher than 500°C , which indicates that single-phase GaP achieved. This confirms the RHEED observation. The sidewall is close to obtuse at lower temperatures of 400°C , indicating the GaP with another orientation dominates. However, it is not as apparent as at high growth temperatures, probably due to the existence of antiphase domain defects. The difference in the sidewall profile proves the phases are different under different growth temperatures. The acute sidewall indicates that the phase with 4° off (100) towards (111)A plane grows at high temperature, and the obtuse sidewall means 4° off (100) towards (111)B plane is achieved at low growth temperature.

At 450°C temperature and flux ratio of $2.5\times$, the sidewall is vertical, which indicates that mixed phases have been grown. Thus, a threshold temperature exists for determining which phase is grown. The threshold temperature for phase selection is about 450°C when the flux ratio is equal to $2.5\times$.

5.3.1.3 V/III flux ratio

As shown in Figure 5-6, when the flux ratio is increased to $8\times$, an acute sidewall is still observed for growth at 550°C . However, all the sidewalls are vertical for all temperatures $<500^\circ\text{C}$. The etching profiles indicate that a high flux ratio increases the threshold

temperature for phase selection. It is still uncertain why the low temperature phase disappears under high flux ratio, but it is possible that the large roughness changes the surface properties controlling phase selection.

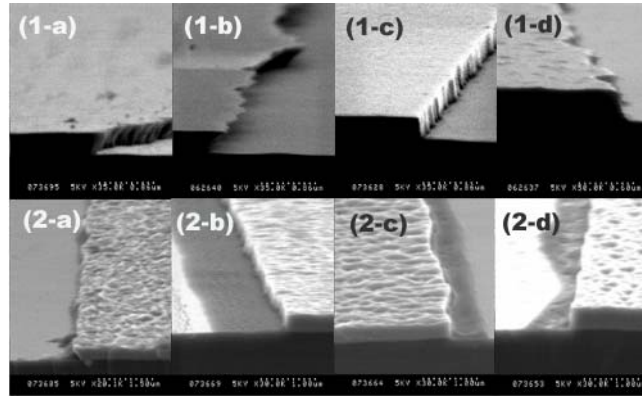


Figure 5-6 SEM images of anisotropic etching V/III flux: (1) 3×; (2) 8×. Temperatures: (a) 550°C; (b) 500°C; (c) 450°C; (d) 400°C.

In addition, the surfaces are extremely rough with a high flux ratio, no matter what temperature is used, which indicates that a low flux ratio is preferred to get high quality GaP growth.

5. 3. 1. 4 Nucleation conditions---temperatures and prelayers

During the studies shown in Figure 5-5 and Figure 5-6, the P₂-exposure and the growth of a thick GaP film are carried out at the same temperature. The first layer or prelayer is phosphorous. Further growth study shows that the phases of GaP roughly depend on the growth conditions of the first 10 monolayers, including the prelayers, the growth temperatures and the P₂ exposure methods. This characteristic will help improving the quality of GaP. As shown in Figure 5-6, the surface of GaP grown at low temperature is extremely rough, and a two-step growth method is required to improve the film quality. The surface of the GaP is still rough using this growth method, though much smoother than the one-step growth case.

If only ~10 MLs GaP are required to control the phases, a thick GaP layer can be grown under optimized growth conditions and the film quality will be dramatically better, no matter what nucleation conditions are used. The growth conditions of the first 10MLs of GaP (or so called nucleation of GaP) are studied in terms of nucleation temperatures and prelayers. Figure 5-7 shows the results of anisotropic etching for films with different four nucleation

conditions. Two nucleation temperatures are studied, 350 and 500°C, and for each temperature, either a Ga-prelayer or a P-prelayer is used.

For the growth with P-prelayers, the P₂ exposure is controlled according to the 2nd approach described before, in which, the P₂ flux is supplied after the substrate temperature is stabilized. At the exposure or nucleation temperatures, the Si surface is exposed to P₂ flux for 5 mins and about 10MLs GaP is deposited by MEE growth.

For growth with Ga-prelayers, after the substrate is stabilized at the nucleation temperatures, the P-source is heated up to provide about 1×10⁻⁸Torr P₂-flux when the shutter is open, so that the background P₂ pressure is about 1-2×10⁻⁹Torr when the shutter is closed. After deposition of about 1ML Ga, the P-shutter is opened to stabilize the surface, and at the same time, the P₂-source is heated up to provide P₂-flux for normal GaP growth. We hope the first layer is uniformly covered by Ga, but Ga droplets form without P₂ to stabilize the surface, the the growth will be very bumpy. This has been observed for the growth without low-P₂ flux protection.

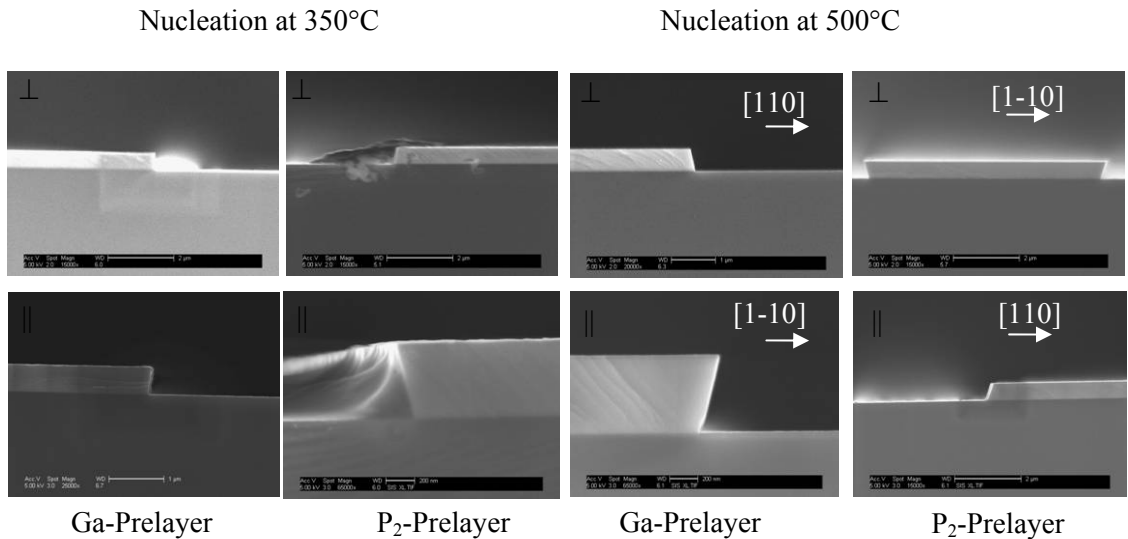


Figure 5-7 SEM images of anisotropic etching with various prelayers and growth temperatures

||: mesa parallel to steps; ⊥: mesa perpendicular to steps

The top row of SEM images in Figure 5-7 show the sidewalls of mesas perpendicular the to surface steps due to the substrate offcut, and the bottom row of SEM images show the sidewalls of mesas parallel to the surface steps. The sidewall angles are opposite under the same growth conditions. With P₂-prelayers, the phases are opposite for growth temperatures at

350 and 500°C. With Ga-prelayers, the phases are identical for both temperatures.

In all four growth conditions, only the phase grown with a P₂-prelayer and nucleation at 500°C is different from the rest. The surface quality of this phase is also the best. The surface is very rough for films grown under other conditions. Figure 5-8 shows the AFM images of films grown under these four growth conditions. The surface texture directions clearly indicate the phase differences. The RMS surface roughness is less than 1nm for the sample grown at 500°C and P₂-prelayer, but around 2nm for the others.

5.3.1.5 Summaries on phase control

As a quick summary, the phases of GaP are affected by the V/III flux ratio, nucleation temperature and P₂-exposure history. Table 5-1 lists the phases controlled by growth temperatures and prelayers. Besides the growth conditions listed in table 5-1, the P₂/Ga flux ratio is also a crucial element. A low P₂/Ga flux ratio is desired for the growth and the optimal value is around 3 for GaP growth on Si.

The comparison of GaAs growth on Ge and GaP on Si shows that the phase control is similar in both systems. A high nucleation temperature results in single-phase of 4°→111A, where the opposite phase forms at low growth temperatures. However, the interaction of P atoms and Si atoms on the Si surface plays a more significant role than the interaction of As on Ge.

Table 5-1 Orientations of GaP on Ge under different growth conditions

Growth condition number	Nucleation Temperature (°C)	Prelayers	P ₂ -exposure history	GaP Phases	Surface Roughness
1	350°C	P ₂	#2, exposure at 350C	4°→(111)B	OK
2	350°C	Ga		4°→(111)B	Worst
3	500°C	P ₂	#2, exposure at 500C	4°→(111)A	Best
4	500°C	Ga		4°→(111)B	OK
5	500°C	P ₂	#3, exposure at high T	4°→(111)B	OK

In addition, both systems show that a low V/III flux ratio improves the single-phase growth and the requirement of a low P/Ga flux ratio is more critical. A high P/Ga ratio dramatically increases the threshold temperatures for phase selection, which is not observed in GaAs grown on Ge.

5.3.2 Surface roughness

The quality of GaP on Si in prior works was very poor, and particularly, the surface was

extremely rough, with rms surface roughness in the range of 2 nm. The poor quality of the GaP on Si prevents its application for integration of optoelectronic devices on Si substrates. Though our devices have a higher tolerance to surface roughness, a smooth surface is generally preferred, in that the template corrugation will be much smaller. In addition, other types of GaP devices, such as LEDs would also be possible if the quality of GaP could be improved. The growth conditions were investigated to improve the surface smoothness, including the flux ratios, GaP surface anneal during growth, and MEE growth techniques.

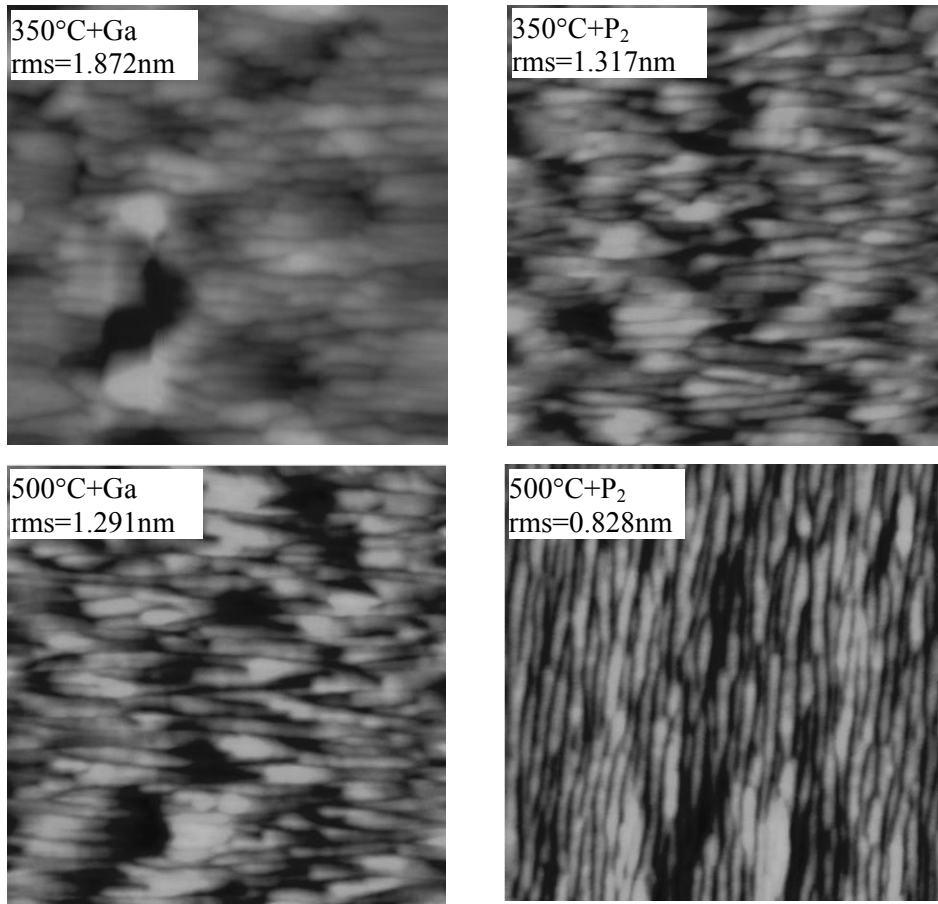


Figure 5-8 AFM images of GaP with four nucleation conditions

5.3.2.1 Flux ratio

The first parameter found to directly affect the surface roughness is the P₂/Ga BEP flux ratio. A high flux ratio dramatically increases the surface roughness, thus a flux ratio as low as possible is desired. Figure 5-9 shows the AFM images of samples grown under various growth conditions. The images on the top row are the samples grown at a low flux ratio of

2.5 \times , and the images on the bottom row are grown at a flux ratio of 8 \times . At a high temperature (500 $^{\circ}$ C) and a low flux ratio, the film is very smooth, the peak-to-valley roughness is below 5 nm and the rms roughness is 0.824 nm. The surface roughness increases dramatically with decreased growth temperature; the peak-to-valley distance is 10nm at 450 $^{\circ}$ C, 30nm at 400 $^{\circ}$ C. A high growth temperature is required to achieve smooth growth. At the high flux ratio 8 \times , the surface is rough for all the growth temperatures. All the growths have a roughness of about 40nm. Thus, a low flux ratio is required for the GaP growth on Si. This conclusion coincides with the observation of GaAs on Ge, where a low flux ratio at \sim 8 \times helps the growth. However, the P/Ga flux ratio cannot be too low, for example less than 2 \times , otherwise, the P flux is not sufficient to maintain a P-stabilized surface and Ga droplets form. The best flux ratio is \sim 2.5 \times ; this conclusion is consistent with Wright's results[115].

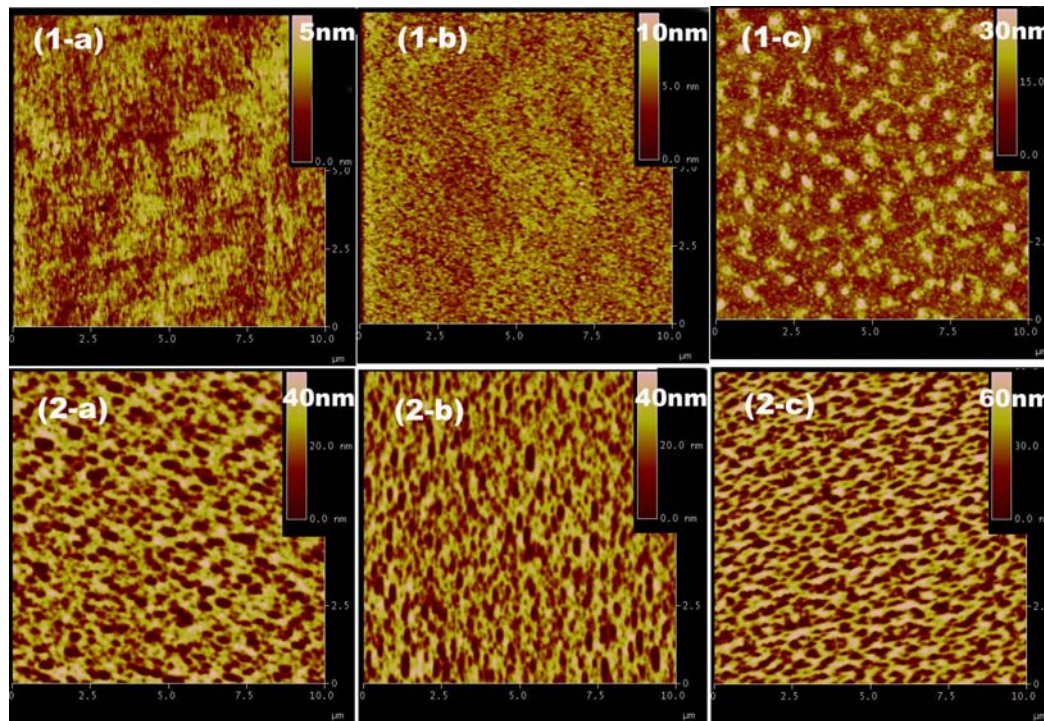


Figure 5-9 AFM images of GaP grown under different flux ratios
 1: V/III=2.5; 2: V/III=8; a: T_g=500 $^{\circ}$ C; b: T_g=450 $^{\circ}$ C; c: T_g=400 $^{\circ}$ C

In addition, generally a low flux ratio means a higher growth temperature is also desired. However, the results show that when the growth temperature is higher than 600 $^{\circ}$ C, the surface is rough and cloudy, close to what we observed during GaAs growth on Ge, where lots of antiphase domains exist. Thus, the best temperature range to get smooth single-phase GaP films is around 500-550 $^{\circ}$ C.

5.3.2.2 MEE growth and annealing

We were also interested to see if the MEE growth would help improve the surface quality as we didn't want to rely on controlling the flux ratio only because the GaP-decomposition source cannot provide a stable P-flux. In addition, the uniformity of the P-flux is poor, especially at a low P₂/Ga flux ratio, resulting in variation of the quality across a single wafer. Table 5-2 shows the results of GaP grown under three different conditions. Each growth type represents average results of a few growth runs. The GaP is nucleated at 500°C, and the subsequent growth is carried out at 550°C for three growth conditions. GaP with a thickness of ~200Å is grown by MEE.

Table 5-2 Surface roughness of GaP

Wafer number	Growth methods of GaP on Si	rms of surface roughness
1491a	a. 10MLs GaP by MEE at 500 °C b. 150Å GaP by MBE at 550°C, V/III=2.5×	0.313nm
1489	a. 10MLs by MEE at 500°C b. 150 Å GaP by MEE at 550°C	0.937nm
1491b	a. 10MLs by MEE at 500°C b. 10mins anneal at 550°C without P ₂ flux c. 150 Å GaP by MEE at 550°C	0.511nm

The second growth step of sample #1491a is carried out by regular MBE with a low P₂/Ga flux ratio at 2.5×. The rms of the surface roughness is around 0.313nm, which is as smooth as the homo-epitaxy growth. Sample #1489 is grown using MEE. However, the rms of the surface roughness is close to 1 nm. This result directly contradicts the conclusion from other materials systems. During the study of GaAs growth on Ge, we also observed that MEE growth doesn't help the growth of single-phase GaAs, but it still results in smoother GaAs films.

The most probable explanation is that there exists a high background P-pressure, even when the shutter is closed during the MEE growth of GaP. The high background pressure causes the MEE growth steps to be ineffective. A source that can better control the flux is required to study the effect of MEE growth. However, we didn't realize this until after we had systematically studied the MEE growth technique for thin GaAs on Ge.

Sample #1491b includes an additional anneal step between the two growth steps. After about 10MLs GaAs growth, the film is annealed. The purpose of this annealing step is to accelerate the coalescence of GaP nuclei and thus achieve 2-D growth. The anneal temperatures and P₂-pressure during anneal are studied. Table 5-2 shows a typical annealing

result. Compared with the same growth without anneal, the surface has been improved. We also found a low P_2 -overpressure (or with background P_2 only) during the annealing is desirable for smoothing the surface. A high P_2 -overpressure during the annealing does not appreciably improve the surface roughness. All these observations coincide with the growth results of GaAs on Ge. We believe similar mechanisms effect GaP on Si. However, the roughness is still much greater than for simple MBE growth with low P/Ga flux ratio. In this sense, direct MBE growth with a low P/Ga flux ratio with this P_2 source has proven to be the best approach to obtain smooth GaP on Si.

5. 4 OP-GaP template fabrication

5. 4. 1 Process flow

The OP-GaP template is fabricated based on the growth results described earlier. Since we are able to grow single-phase GaP with both orientations on Si, it is natural to design the growth techniques to fabricate OP-GaP templates on Si substrates. Figure 5-10 shows the process flow of the OP-GaP template on Si. We start with Si substrates with 4° offcut towards [110]. First, a single-phase-GaP film is grown on Si, denoted as GaP(+) in Figure 5-10. The thickness is between 500-1000Å in order to obtain single-phase GaP, but as thin as possible so that the template corrugation is not too high. The sample is then taken out of the MBE chamber and patterned with proper QPM periods. The exposed GaP layer is etched via dry etching or chemical etching. After removing the photoresist and cleaning the surface, the sample is reloaded for regrowth. During the regrowth, the growth parameters are properly controlled so that we obtain single-phase GaP with the opposite orientation on the exposed Si surfaces, while still maintaining good crystal quality on the remaining GaP surfaces. After initial nucleation growth, the surface forms a pattern with two orientations. A subsequent thick GaP layer $\sim 2 \mu\text{m}$ is deposited on the patterned substrates, and both domains grow vertically, maintaining the right QPM domain boundaries.

Conceptually, this is an easy design, however, there are quite a few growth issues that must be solved. The first one is choosing the right growth conditions for both GaP(+) and GaP(-) phases, because the second growth will be affected by the existing GaP. A second issue is how to control the etching process to remove the exposed GaP and maintain good Si surface quality. The final issue is how to obtain clean surfaces for the MBE regrowth.

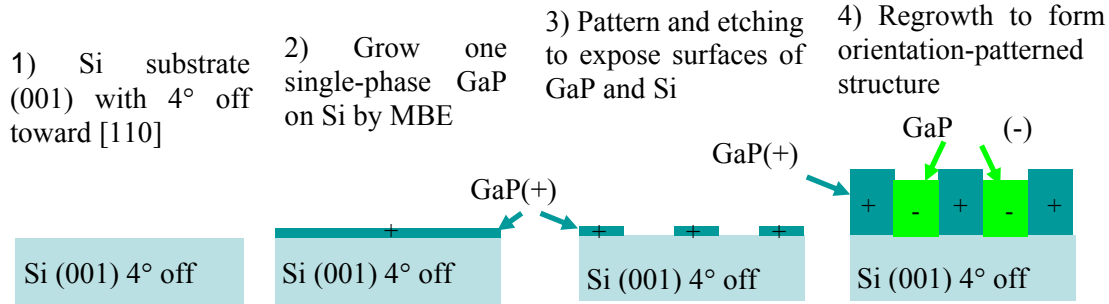


Figure 5-10 Fabrication process of OP-GaP template on Si substrates

5. 4. 2 Etching and cleaning

The etching recipe of the GaP has been studied. Both dry etching and wet etching techniques were investigated. The dry etching is straightforward, which is the same as the techniques used to fabricate AlGaAs waveguides. The etching recipe is the same as described in chapter 4. The only difference is the etching rate of GaP, which is about 1000Å for 2 mins. The etching rate of Si using this etching recipe is much slower, thus it is possible to completely remove the GaP without damaging the Si layer. However, the dry etching is not an ideal method for epitaxial regrowth. The remaining Si surface is extremely rough and the growth of GaP on Si is very complicated. AFM measurements show the GaP grown on the Si surfaces after dry etching is an order of magnitude rougher than the GaP grown on the non-etched clean Si surfaces.

Thus, a wet etching technique was performed. Various chemicals have been tested. However, most of them have very high etching rates, such as HBr:H₂O₂:H₂O (1:1:10) and HCl:HNO₃:H₂O(1:1:1) with etch rates much higher than 1µm/min. It only takes a couple seconds to etch the GaP layer with thicknesses of 300-1000Å and the lateral etching is then very severe. Great efforts have been taken to control the etching process, but the etching quality is not yet controllable. In the end, we used HCl: HNO₃: CH₃COOH (1:1:1). This etchant etches GaP only and stops at the Si substrate. The etch rate is around 0.25µm/min[121], and ~10 seconds is required to etch 500Å GaP.

After etching the GaP film, the sample is cleaned. To obtain a clean surface before the regrowth is crucial, in that the surface conditions almost certainly control the results we obtain. A similar cleaning process to that used on the GaAs template was used. The photoresist is cleaned in heated photoresist-removal solvent (1165) combined with ultrasonic cleaning. Solvent 1165 is heated to 50°C and the sample is soaked in this solvent for 10 mins. After the 1165, the sample is transferred to heated acetone for another 10mins. In the end, the sample is cleaned with cold methanol and isopropanol for 5 mins each.

After removing the photoresist, a series of chemical etching is performed to clean the surface right before reloading into the MBE system for regrowth. The sample is cleaned in HCl:H₂O, H₂O₂, HF, H₂O₂ sequentially. This cleaning process is repeated for 2-3 times. In the end, the sample is etched in HF, and loaded immediately to prevent the surface from oxidizing. A good RHEED pattern is observed before the growth after the sample is cleaned using this approach.

5. 4. 3 Two single-phase GaP growth

The growth methods of two single-phase GaP films have to be investigated, especially considering the growth of the second single-phase GaP on Si. The growth parameters to get single-phase GaP on Si were listed in Table 5-1. The GaP with 4° off towards (111)A is grown only under one growth condition, in which the P₂-exposure occurs at 500°C and a P₂-prelayer is used. Theoretically, any other growth condition will result in the GaP with 4° off towards (111)B. However, P₂-desorption from the remaining GaP makes the use of a Ga-prelayer impossible. Thus, only P₂-prelayers are used for the 2nd growth step. Two possible growth conditions are used to grow the second GaP with 4° off towards (111)B.

One of the growth conditions used is exposure of Si surface to P₂ at low temperatures, 350°C. No oxide-desorption is carried out using this growth condition, otherwise a P₂-overpressure is required to protect the P₂ from desorption and the background P₂-pressure is too high when the substrate temperature is reduced from the desorption temperature. Thus, the Si surface has to be cleaned and hydrogen-terminated to prevent surface oxidation.

The second growth condition used to obtain a GaP with 4° off towards (111)B is to apply a P₂-exposure at high temperature, and then reduce the temperature with P₂-exposure. It is possible to carry out Si-oxide desorption in this case. However, the temperature cannot be too high, because P₂ desorption is severe, even with a high P₂-overpressure.

OP-GaP templates have been successfully obtained under two growth conditions. Figure 5-11 shows SEM and AFM images of the OP-GaP grown using the first set of growth conditions. The thickness of the first GaP is around 1000Å and GaP with a total thickness of 1µm is grown after processing. The SEM is a top view of the OP-GaP after regrowth, and an isotropic etching is performed so that the right end facets of both domains are revealed after the chemical etching. The end facets are of opposite angles, indicating that orientation of both phases is achieved. The AFM images also show the texture directions are reversed across the domain boundaries, which again confirms the domain inversion between the boundaries. Unfortunately, the surface roughness of the second GaP is very large, as denoted as the

GaP(-). This is probably because the Si surface was not thermally cleaned before the growth of the second GaP layer.

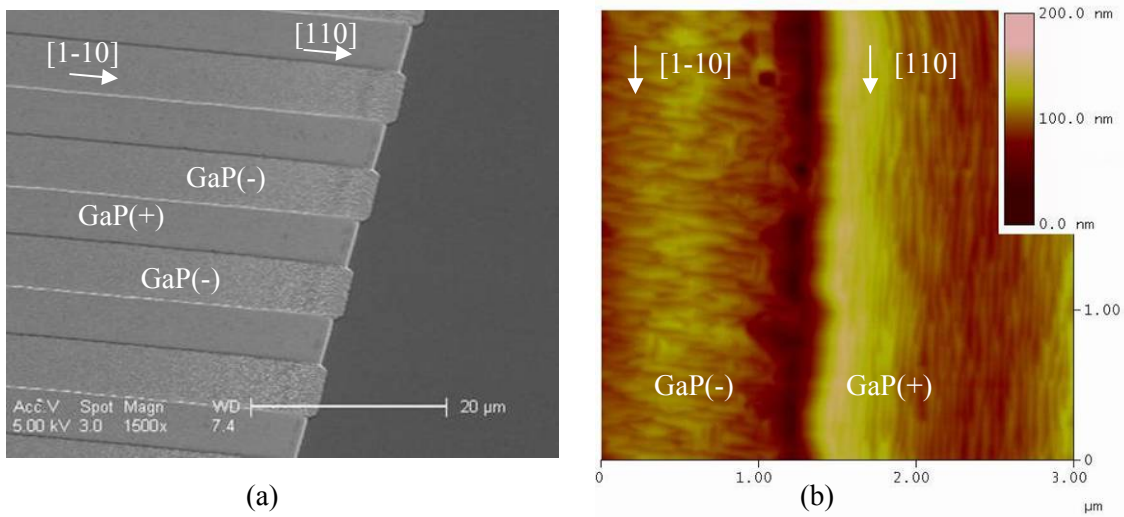


Figure 5-11 SEM and AFM images of the OP-GaP template structure

Figure 5-12 shows a cross-sectional SEM of the OP-GaP structure. The thickness of the first GaP layer is $\sim 300\text{\AA}$. The second GaP layer is grown using the second approach described above, in which the substrates are thermally cleaned at $\sim 800^\circ\text{C}$ with a P_2 -overpressure to protect the GaP surfaces. After thermal cleaning, the substrate temperature is reduced to about 500°C under P_2 -flux. About 10MLs GaP is then grown at 500°C by MEE, followed by a subsequent GaP layer 300\AA thick grown at 550°C . Finally, $\sim 5\text{-}\mu\text{m}$ GaP is grown at $\sim 630^\circ\text{C}$ with a P_2/Ga flux ratio of about $5\times$.

The cross-section is etched using an anisotropic etchant ($\text{HBr}:\text{H}_2\text{O}_2:\text{H}_2\text{O}=1:1:3$) to reveal the antiphase domain boundaries. As shown in Figure 5-12, the domain boundaries are clearly observed for the domains with a QPM period of $4.8\ \mu\text{m}$, which confirms the success of the two single-phase GaP growths. The domain boundaries are not exactly vertical, which is probably because the P_2/Ga flux ratio is too low and the growth temperature is too high. However, the QPM domains are preserved for such small QPM periods with about $5\text{-}\mu\text{m}$ growth. The variation of the domain width is negligible for the QPM periods suitable for mid-IR generation, where the QPM period is generally tens of microns.

A bumpy top surface is shown in Figure 5-12, which is caused by the chemical etching rather than the regrowth. The sample is cleaved and etched without any surface protection. Although the real surface is not very smooth after $5\text{-}\mu\text{m}$ growth, it is good enough as a seed for further thick GaP film growth.

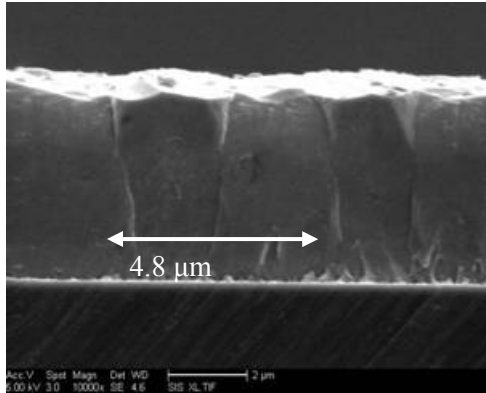


Figure 5-12 Cross-sectional SEM of the OP-GaP template structure

5.5 Conclusions

The growth of single-phase GaP has been described in this chapter. We are able to control the orientation of GaP on Si by properly controlling the growth conditions, such as growth temperature, V/III flux ratio, prelayers and P₂-exposure conditions. We fabricated OP-GaP templates on Si substrates based on the growth results and saw obvious inverted domains after a thick GaP regrowth on the template. We believe this development will provide a source for fabricating thick GaP bulk nonlinear optical devices in the near future.

Chapter 6 SUMMARY AND FUTURE WORK

In the introduction section, we identified a number of applications for nonlinear optical frequency conversion in the near and mid-IR, including: countermeasures, remote sensing, spectroscopy, as well as communications applications, such as WDM frequency conversion. All the applications required nonlinear optical devices with high conversion efficiency. Thus, developing new materials systems with high nonlinear optical coefficients is necessary. Of the III-V materials GaAs and GaP are the most promising. In order to use this family of materials, we developed an all-epitaxial orientation patterning approach. The materials growth techniques and the related mechanisms are studied in this dissertation in order to obtain efficient nonlinear optical devices.

6. 1 Accomplishment

My accomplishments are described in two parts. The first part is understanding the mechanism and the materials growth of OP-materials. The second part is the fabrication and optical characterization of nonlinear optical devices from OP-AlGaAs nonlinear waveguides.

6. 1. 1 *Material growth*

Two material systems were studied in this dissertation. The first one is OP-GaAs growth. In this study, we identified a set of growth conditions that affect the antiphase defect growth behavior, including a low V/III flux ratio, high temperature annealing, and a low growth rate. We directly observed antiphase boundary annihilation behavior and antiphase boundary face propagation as a function of the V/III flux ratio, in which a low flux ratio results in an APB plane more horizontal and speeds up the annihilation process. We studied the adatom diffusion behavior and correlated the experimental observation to diffusion anisotropy of Ga adatoms. Based on this study, we fabricated OP-GaAs templates with much lower template corrugation.

In addition, we also studied the regrowth on orientation patterned surfaces, identified the domain boundary development during regrowth as a function of growth conditions and investigated the mechanisms. As a result, we were able to grow waveguide structures with high domain boundary quality and low corrugations. In this sense, we have resolved all of the growth issues which had been previously limiting the application of this approach.

The second material system is OP-GaP. We applied the same research methods to the

GaP growth and found the growth conditions that lead to two distinct single-phase GaP on Si and thus fabricated an initial OP-GaP template on Si. The initial result of OP-GaP template on Si also makes practical high power nonlinear optical devices possible.

6. 1. 2 Device fabrication and optical characterization

We optimized the fabrication process of AlGaAs SHG waveguides pumped at 1.55 μm and identified the dominant mechanisms that limited the performance of our prior waveguides. The waveguides exhibit a propagation loss of $\sim 4.5\text{dB/cm}$ at 1.55- μm wavelength and $\sim 9.7\text{dB/cm}$ at 780-nm wavelength. An internal SHG conversion efficiency as high as 43%/W with an 8-mm-long waveguide was achieved. This is the highest reported value for AlGaAs nonlinear waveguides.

6. 2 Future work

The successful development of low-corrugation templates and low-loss waveguides makes it possible for us to fabricate nonlinear optical waveguides with high conversion efficiency so that practical applications are now possible. Unfortunately, this dissertation work didn't finish all parts of this work. In the future, several types of devices can be investigated, based on our current results, including low-loss waveguides for telecommunications, high power DFG waveguides, and OP-GaP devices based on thick film growth.

6. 2. 1 Low-loss waveguides design and fabrication

The first possible devices to be fabricated are low-loss waveguides working at wavelengths $\sim 1.55\ \mu\text{m}$. In this work, AlGaAs waveguides were fabricated with so far the lowest loss. However, the loss at SH wavelength is still high. In order to fabricate AlGaAs waveguides with ultra-high conversion efficiency to compete with the LiNbO₃ waveguides, in which, the conversion efficiency is as high as $1000\%W^{-1}$, we need to reduce the losses at both fundamental and SH wavelengths to as low a value as possible. For example, waveguides with SHG conversion efficiency of $1000\%W^{-1}$ require the losses at both wavelengths to be $\sim 1\text{dB/cm}$.

AlGaAs nonlinear waveguides apparently have great advantages over LiNbO₃ waveguides, in that the second order nonlinear coefficient of GaAs or AlGaAs is several times higher than LiNbO₃. A 3-4-cm-long LiNbO₃ waveguide is required to obtain a conversion efficiency of 1000%/W because tighter confinement is unavailable in PPLN; a much shorter AlGaAs waveguide is sufficient to obtain this efficiency if the loss can be reduced to 1dB/cm.

The waveguides obtained in this dissertation work still have losses much higher than the desired value. The template corrugations have been minimized and the regrowth conditions are also optimized to eliminate the regrowth-induced corrugations. There is not much margin to continue improve the growth conditions because the loss of unpatterned waveguides now constitutes the major part of the waveguide loss. We believe improving the waveguide quality and redesigning the waveguide structures for ultra-low loss will be the next immediate step to fabricate practical waveguides. Figure 6-1 shows a comparison of unpatterned waveguide structures to the current waveguides and possible waveguides with ultra-low loss.

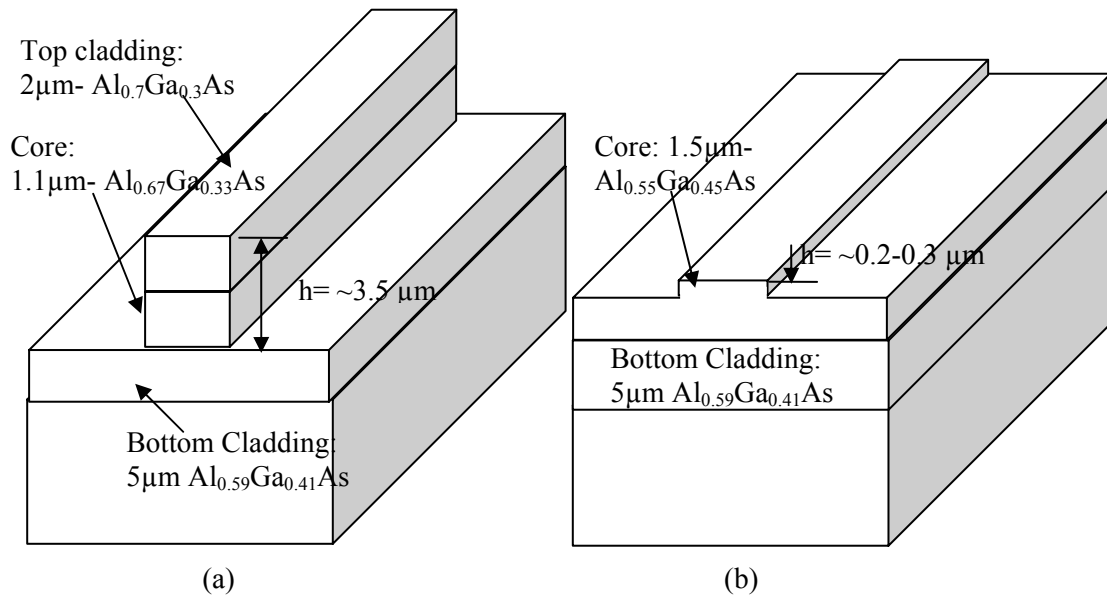


Figure 6-1 Comparison of low-loss waveguide structures vs. current waveguide structures. a: Current waveguides; b: low corrugation waveguides

Figure 6-1a is the waveguide structure we currently use for the nonlinear AlGaAs waveguides. The ridge is etched down through the waveguide core. This type of waveguide suffers from the scattering of the sidewall roughness. The loss is ~ 3 dB/cm for the unpatterned waveguides. Figure 6-1b shows a type of low-loss waveguide. No top cladding is used in this structure, and the waveguide core is $1.5 \mu\text{m}$. The ridge is only etched $\sim 0.2-0.3 \mu\text{m}$. The loss due to the sidewall scattering is minimized in this type of waveguide and a loss as low as $0.1-0.2$ dB/cm has been reported[112-124]. We believe that nonlinear AlGaAs waveguides with loss as low as 1 dB/cm can be fabricated based on this kind of structure. One major concern is whether a moderately high normalized conversion efficiency can be still maintained in this type of waveguide. If the normalized conversion efficiency is dramatically reduced with this

type of structure, the improvement resulting from the reduced waveguide loss will be compromised by the reduction of normalized conversion efficiency.

Table 6-1 shows the normalized conversion efficiency for the waveguides with various dimensions. For the waveguide width (W) of around 3.5-6 μm and an etching depth (h) of around 0.25 μm , the normalized conversion efficiency is around 350%W⁻¹cm⁻², which is close to the value of current waveguides. In addition, the waveguides with these dimensions are single-mode waveguides. Thus, ultra-high conversion efficiency can be expected with the reduced waveguide losses.

Table 6-1 Normalized conversion efficiency (W⁻¹cm⁻²) vs. waveguide dimensions

	3 μm	3.5 μm	4 μm	4.5 μm	5 μm	6 μm	6.5 μm	7 μm
h=0.2 μm	3.16	3.20	3.22	3.21	3.18	3.07	3.01	2.94
h=0.25 μm	3.17	3.43	3.60	3.68	3.69	3.60	3.52	3.42
h=0.4 μm	2.82	3.42	3.80	4.00	4.07	3.98	3.88	3.76

As shown in Figure 6-2, the SHG conversion efficiency can increase to 1000%/W from the current 43%/W if the loss at the fundamental wavelength can be reduced to 1dB/cm and the loss at the SH wavelength to ~1.5dB/cm.

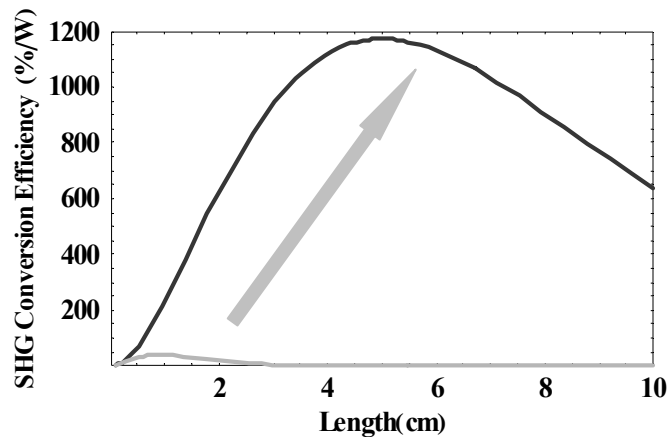


Figure 6-2 Expected SHG conversion efficiency of low-loss waveguides

6. 2. 2 High power DFG waveguide

The second possible device is high power DFG nonlinear waveguides operated in the mid-IR range using waveguides with structures similar to the current one or with new waveguide structures. Current results show that the waveguide loss increases with reduced wavelength

for narrow QPM periods. We expect the waveguide loss can be further reduced, even using current waveguides. In addition, the QPM periods for the DFG waveguides are much larger than $4.8 \mu\text{m}$, eg, $\sim 15 \mu\text{m}$ for the DFG process with input wavelengths at 1.3 and $1.55 \mu\text{m}$ and output wavelengths at $8.06 \mu\text{m}$. Large QPM periods result in fewer epitaxial growth challenges and thus better waveguide quality. Both factors will greatly reduce the waveguide loss. If the losses at all the interacting wavelengths are reduced to $\sim 3\text{dB/cm}$, conversion efficiencies as high as $200\%/W$ can be expected.

Future research should be focused on designing waveguide structures so that only one specific nonlinear interaction exists in the waveguides for one fixed QPM period, otherwise, multiple interactions exist and the output will be multiple mode and multiple wavelengths. In the ideal case, only one guided mode exists in the waveguides for all the interaction wavelengths. The waveguide dimension has to be large enough so that a guided mode exists at the longer wavelength, but large dimensions result in multiple modes at the shorter wavelengths. In SHG waveguides, a single-mode exists at the input fundamental wavelengths, thus, the SH wave generated is at single wavelength. In DFG waveguides, the input wavelengths are at shorter wavelengths and multiple modes exist. Nonlinear interactions involving higher order modes bring forth nonlinear generation at multiple wavelengths. One approach to solve this problem is to design a tapered waveguide structure[125,126], so that only a single-mode exists at the input short wavelength, while the long wavelength is guided after the tapered region.

6. 2. 3 OP-GaP thick film growth

The third possible type of device is based on bulk OP-GaP grown on the OP-GaP template. Both GaP substrates and Si substrates can be used. The results obtained thus far for OP-GaP templates are far from optimized at the current stage and great challenges are in front for us to obtain OP-GaP nonlinear waveguides. However, the bulk devices are more tolerant to the film quality and OP-GaP templates can be readily available for OP-GaP thick film growth.

There are a few problems to be solved for developing bulk OP-GaP devices. First, we need to find suitable crystal growth tools for thick film GaP growth. Second, we need to investigate the growth conditions to obtain thick films while still maintaining vertical propagation of the antiphase domains.

Furthermore, we need to investigate the effect of thermal expansion mismatch on the growth of thick GaP films on Si substrates. The total thickness will exceed the thickness of Si substrates, and a high growth temperature is required in chemical vapor deposition to obtain

fast growth and thick film deposition. Under these conditions, the thermal expansion mismatch can be very severe. Thus, GaP substrates probably work better for the thick film GaP growth than Si substrates. The fabrication process of OP-GaP on GaP substrates is close to that of OP-GaAs on GaAs substrates. Since we can control both orientations of GaP on Si substrates, it will be easier to control only one phase on a Si intermediate layer on a GaP substrate.

In this sense, the OP-GaP nonlinear devices on Si substrates are more suitable for developing guided nonlinear devices and it is the ultimate goal in terms of materials growth and devices fabrication, while OP-GaP template fabricated on GaP substrates can possibly provide a readily available device for the high power applications.

6.3 Conclusions

All-epitaxial orientation-patterning of GaAs or GaP is a very promising technology for fabricating high-performance frequency conversion devices. Most of the growth obstacles of OP-GaAs have been solved by our work. Various nonlinear optical devices, including low-loss nonlinear waveguides have been fabricated. These results show that orientation-patterning is certainly superior in many ways to other approaches. It is possible to obtain high performance OP-GaAs nonlinear optical devices that are practical in various applications. In addition, all the growth techniques can be transferred to the GaP system as well, which can lead to significantly higher power nonlinear optical devices with a much broader tuning range.

BIBLIOGRAPHY

1. T. Sorokina and K. L. Vodopyanov, *Solid State Mid-Infrared Laser Sources*, Springer-Verlag, Topics in Applied Physics, Berlin, Heidelberg, New York (2003).
2. D. Kleine and H. Dahnke, W. Urban, P. Hering and M. Murtz, "Real-time detection of $^{13}\text{CH}_4$ in ambient air by use of mid-infrared cavity leak-out spectroscopy," *Opt. Lett.* **25**, 1606-1608 (2000).
3. R. J. McNichols and G. L. Cote, "Optical glucose sensing in biological fluids: an overview," *J. Biomed. Opt.* **5**, 5 (2000).
4. M. Tacke, "Lead-salt lasers," *Philosophical Transactions of the Royal Society London, Series A* **359**, 547 (2001).
5. J. Faist, F. Capasso, D. L. Sivco, C. Sirtori, A. L. Hutchinson, and A. Y. Cho, "Quantum cascade laser," *Science* **264**, 553 (1994).
6. D. Hofstetter, M. Beck, T. Aellen, and J. Faist, "High-temperature operation of distributed feedback quantum-cascade lasers at $5.3\ \mu\text{m}$," *Appl. Phys. Lett.* **78**, 396 (2001).
7. L. A. Coldren and S. W. Corzine, *Diode lasers and photonic integrated circuits*, Wiley, New York (1995).
8. M.M. Fejer, "Nonlinear optical frequency generation," *Physics Today* **47**, 25-32(1994).
9. C. Da-Wun and K. Masters, "Continuous-wave $4.3\text{-}\mu\text{m}$ intracavity difference frequency generation in an optical parametric oscillator," *Opt. Lett.* **26**, 25 (2001).
10. G. D. Miller, R. G. Batchko, W. M. Tulloch, D. R. Weise, M. M. Fejer, and R. L. Byer, "42%-efficient single-pass CW second-harmonic generation in periodically-poled lithium niobate," *Opt. Lett.* **22**, 1834 (1997).
11. F. Ganikhanov, T. Caughey, and K. L. Vodopyanov, "Narrow-linewidth middle-infrared ZnGeP_2 optical parametric oscillator," *J. Opt. Soc. Am. B* **18**, 818 (2001).
12. K. P. Petrov, A. T. Ryan, T. L. Patterson, L. Huang, S. J. Field, and D. J. Bamford, "Spectroscopic detection of methane by use of guided-wave diode-pumped difference-frequency generation," *Opt. Lett.* **23**, 1052-1054 (1998).
13. T. J. Kulp, S. E. Bisson, R. P. Bambha, T. A. Reichardt, U. B. Goers, K. W. Aniolek, D. A. V. Kliner, B. A. Richman, K. M. Armstrong, R. Sommers, R. Schmitt, P. E. Powers, O. Levi, T. Pinguet, M. M. Fejer, J. P. Kplow, L. Goldberg and T. G. Mcrae, "The application of quasi-phase-matched parametric sources to practical infrared chemical

- sensing systems,” *Appl. Phys. B*, **75**, 317-327 (2002)
14. M. H. Chou, I. Brener, G. Lenz, R. Scotti, E. E. Chaban, J. Shmulovich, D. Philen, S. Kosinski, K. R. Parameswaran, and M. M. Fejer, “Efficient wide-band and tunable midspan spectral inverted using cascaded nonlinearities in LiNbO₃ waveguides,” *IEEE Photon. Technol. Lett.* **12**, 82 (2000).
 15. D. Mazzotti, P. De Natale, G. Giusfredi, C. Fort, J. A. Mitchell, and L. W. Hollberg, “Difference-frequency generation in PPLN at 4.25- μ m: an analysis of sensitivity limits for DFG spectrometers,” *Appl. Phys. B, Lasers Opt. B* **70**, 747 (2000).
 16. S. J. B. Yoo, “Wavelength conversion technologies for WDM network applications,” **14**, 955-966 (1996).
 17. H. Q. Ngo, D. Pan, C. Qian, “Nonblocking WDM switches based on arrayed waveguide grating and limited wavelength conversion,” *IEEE Infocom 2004*.
 18. M. H. Chou, J. Hauden, M. A. Arbore, and M. M. Fejer, “1.5- μ m-band wavelength conversion based on difference-frequency generation in LiNbO₃ waveguides,” *Opt. Lett.* **23**, 1004 (1998).
 19. P. A. Budni, L. A. Pomeranz, M. L. Lemons, C. A. Miller, J. R. Mosto, and E. P. Chicklis, “Efficient mid-infrared laser using 1.9- μ m-pumped Ho:YAG and ZnGeP₂ optical parametric oscillators,” *J. Opt. Soc. Am. B* **17**, 723 (2000).
 20. F. Rotermund, V. Petrov, and F. Noack, “Difference-frequency generation of intense femtosecond pulses in the mid-IR (4-12 μ m) using HgGa₂S₄ and AgGaS₂,” *Opt. Comm.* **185**, 177 (2000).
 21. E.D. Palik, *Handbook of Optical Constants of Solids*, Academic Press, Orlando, 1985.
 22. C. Flytzanis and J. Ducuing, “Second-order optical susceptibilities of III-V semiconductors,” *Phys. Rev.* **178**, 1218-1228 (1969).
 23. J. J. Wynne and N. Bloembergen, “Measurement of the lowest-order nonlinear susceptibility in III-V semiconductors,” *Phys. Rev.* **188**, 1211-1220 (1969).
 24. J. C. Phillips and J. A. Van Vechten., “Nonlinear optical susceptibilities of covalent crystals,” *Phys. Rev.* **183**, 709-711 (1969).
 25. Shoji, T. Kondo, A. Kitamoto, M. Shirane, and R. Ito, “Absolute scale of second-order nonlinear-optical coefficients,” *J. Opt. Soc. Am. B* **14**, 2268-2294 (1997).
 26. M. M. Choy and R. L. Byer, “Accurate second-order susceptibility measurements of visible and infrared nonlinear crystals,” *Phys. Rev. B* **14**, p.1693 (1976).
 27. Chowdhury, H. M. Ng, M. Bhardwaj, and N. G. Weimann, “Second-harmonic generation in periodically poled GaN,” *Appl. Phys. Lett.* **83**, 1077-1079 (2003).

28. K. L. Vodopyanov, O. Levi, P. S. Kuo, T. J. Pinguet, J. S. Harris, M. M. Fejer, B. Gerard, L. Becouarn, E. Lallier, "Optical parametric oscillator based on microstructured GaAs," *Solid State Laser Technologies and Femtosecond Phenomena, Proceeding of SPIE.* **5620**, 63-69 (2004).
29. P. S. Kuo, K. L. Vodopyanov, M. M. Fejer, D. M. Simanovskii, X. Yu, J. S. Harris and D. Bliss, D. Weyburne, "Optical parametric generation of a Mid-IR continuum in orientation-patterned GaAs," *Opt. Lett.* **31**, 71-73 (2006).
30. Levi O, T. J. Pinguet, T. Skauli, L. A. Eyres, K. R. Parameswaran, J. S. Harris, M. M. Fejer, T. J. Kulp, S. E. Bisson, B. Gerard, E. Lallier, L. Becouarn, "Difference frequency generation of 8- μ m radiation in orientation-patterned GaAs," *Opt. Lett.*; **27**, 2091-93 (2002).
31. S. E. Bisson, T. J. Kulp, O. Levi, M. M. Fejer, and James S. Harris Jr., "Long-wave infrared chemical sensing based on difference frequency generation in orientation-patterned GaAs," in *Conference on Lasers and Electro-Optics (CLEO 2004)*, San Francisco, CA (2004).
32. K. L. Vodopyanov, O. Levi, P. S. Kuo, T. J. Pinguet, J. S. Harris, M. M. Fejer, B. Gerard, L. Becouarn, E. Lallier, "Optical parametric oscillation in quasi-phasematched GaAs," *Opt. Lett.* **29**, 1912-1914 (2004)
33. L. Becouarn, B. Gerard, M. Brevignon, J. Lehoux, Y. Gourdel, and E. Lallier, "Second harmonic generation of CO₂ laser using thick quasi-phase-matched GaAs layer grown by hydride vapour phase epitaxy," *Electron. Lett.* **34**, 2409 (1998).
34. Y. R. Shen, *The Principles of Nonlinear Optics*. J. Wiley, New York (1984).
35. R.W. Boyd, *Nonlinear Optics*. 2nd ed. Academic Press, Amsterdam (2003).
36. P. A. Franken, A. E. Hill, C. W. Peters, and G. Weinreich, "Generation of Optical Harmonics," *Phys. Rev. Lett.* **7**, 118 (1961).
37. J. A. Armstrong, N. Bloembergen, J. Ducuing, and P. S. Pershan, "Interactions between light waves in a nonlinear dielectric," *Phys. Rev.* **127**, 1918 (1962).
38. G. D. Boyd and D. A. Kleinman, "Parametric interaction of focused gaussian light beams," *J. Appl. Phys.* **39**, 3597 (1968).
39. Fiore, V. Berger, E. Rosencher, P. Bravetti, and J. Nagle, "Phasematching using an isotropic nonlinear optical material," *Nature* **391**, 463-466 (1998).
40. Fiore, S. Janz, L. Delobel, P. van der Meer, P. Bravetti, V. Berger, E. Rosencher, and J. Nagle, "Second-harmonic generation at 1.6 μ m in AlGaAs/Al₂O₃ waveguides using birefringence phase matching," *Appl. Phys. Lett.* **72**, 2942-2944 (1998).

41. S. Venugopal Rao, K. Moutzouris and M. Ebrahimzadeh, "Nonlinear frequency conversion in semiconductor optical waveguides using birefringent, modal and quasi-phase-matching techniques," *J. Opt. A: Pure Appl. Opt.* **6**, 569-584 (2004).
42. K. Moutzouris, S. Venugopal Rao, M. Ebrahimzadeh, A. De Rossi, V. Berger, M. Calligaro, and V. Ortiz, "Efficient second-harmonic generation in birefringently phase-matched GaAs/Al₂O₃ waveguides," *Opt. Lett.* **26**, 1785-1787 (2001).
43. S. Venugopal Rao, K. Moutzouris, M. Ebrahimzadeh, A. De Rossi, G. Gintz, M. Calligaro, V. Ortiz, and V. Berger, "Measurements of optical loss in GaAs/Al₂O₃ nonlinear waveguides in the infrared using femtosecond scattering technique," *Opt. Commun.* **213**, 223-228 (2002).
44. K. Moutzouris, S. Venugopal Rao, M. Ebrahimzadeh, A. De Rossi, M. Calligaro, V. Ortiz, and V. Berger, "Second-harmonic generation through optimized modal phase matching in semiconductor waveguides," *Appl. Phys. Lett.* **83**, 620-622 (2003).
45. S. Ducci, L. Lanco, V. Berger, A. De Rossi, V. Ortiz, and M. Calligaro, "Continuous-wave second-harmonic generation in modal phase matched semiconductor waveguides," *Appl. Phys. Lett.* **84**, 2974-2976 (2004).
46. S. Janz, M. Buchanan, F. Chatenoud, J. P. McCaffrey, and R. Normandin, "Modification of the second-order optical susceptibility in Al_xGa_{1-x}As by ion-beam induced amorphization," *Appl. Phys. Lett.* **65**, 216-218 (1994).
47. Saher Helmy, D. C. Hutchings, T. C. Kleckner, J. H. Marsh, A. C. Bryce, J. M. Arnold, C. R. Stanley, and J. S. Aitchison, "Quasi phase matching in GaAs-AlAs superlattice waveguides through bandgap tuning by use of quantum-well intermixing," *Opt. Lett.* **25**, 1370-1372 (2000).
48. E. U. Rafilov, P. Loza-Alvarez, C. T. A. Brown, and W. Sibbett, "Second-harmonic generation from a first-order quasi-phase-matched GaAs/AlGaAs waveguide crystal," *Opt. Lett.* **26**, 1984-1986 (2001).
49. L. Gordon, G. L. Woods, R. C. Eckardt, R. R. Route, R. S. Feigelson, M. M. Fejer, and R. L. Byer, "Diffusion-bonded stacked GaAs for quasi-phase-matched second-harmonic generation of a carbon dioxide laser," *Electron. Lett.* **29**, 1942 (1993).
50. S. J. B. Yoo, R. Bhat, C. Caneau, and M. A. Koza, "Quasi-phase-matched second-harmonic generation in AlGaAs waveguides with periodic domain inversion achieved by wafer-bonding," *Appl. Phys. Lett.* **66**, 3410-3412 (1995).
51. C. Ebert, "Quasi-phasematched waveguides for infrared nonlinear optics using GaAs/Ge/GaAs heteroepitaxy," Ph.D dissertation, Stanford University, Stanford, CA

- (1998).
52. S. Koh, T. Kondo, T. Ishiwada, C. Iwamoto, H. Ichinose, H. Yaguchi, T. Usami, Y. Shiraki, and R. Ito, "Sublattice reversal in GaAs/Si/GaAs (100) heterostructures by molecular beam epitaxy," *Jpn. J. Appl. Phys.* **37**, L1493 (1998).
 53. C. Ebert, L.A. Eyres, M.M. Fejer, and J.S. Harris, "MBE growth of antiphase GaAs films using GaAs/Ge/GaAs heteroepitaxy," *J. Cryst. Growth* **201**, 187-193 (1999)
 54. S. Koh, T. Kondo, M. Ebihara, T. Ishiwada, H. Sawada, H. Ichinose, I. Shoji, and R. Ito, "GaAs/Ge/GaAs sublattice reversal epitaxy on GaAs (100) and (111) substrates for nonlinear optical devices," *Jpn. J. Appl. Phys.* **38**, L508-L511 (1999)
 55. L. A. Eyres, P. J. Tourreau, T. J. Pinguet, C. B. Ebert, J. S. Harris, M. M. Fejer, L. Becouram, B. Gerard, E. Lallier, "All-epitaxial fabrication of thick, orientation-patterned GaAs films for nonlinear frequency conversion," *Appl. Phys. Lett.* **79**, 904-906 (2001).
 56. L. A. Eyres, "All-epitaxial orientation-patterned semi-conductors for nonlinear optical frequency conversion," Ph.D dissertation, Stanford University, Stanford, CA (2001).
 57. S. Koh, T. Kondo, Y. Shiraka and R. Ito, "GaAs/Ge/GaAs sublattice reversal epitaxy and its application to nonlinear optical devices," *J. Cryst. Growth.* **227/228**, 183-192 (2001).
 58. M. A. Herman and H. Sitter, *Molecular beam epitaxy: fundamentals and current status*, Springer, Berlin (1996).
 59. W. Braun, *Applied RHEED: reflection high-energy diffraction during crystal growth*, Springer, New York (1999).
 60. N.-H. Cho, B. C. De Cooman, C. B. Carter, R. Fletcher, and D. K. Wagner, "Antiphase boundaries in GaAs," *Appl. Phys. Lett.* **47**, 879 (1985).
 61. H. Kroemer, "Sublattice allocation and antiphase domain suppression in polar-on-nonpolar nucleation," *J Vac. Sci. Tech. B* **5**, 1150-1154 (1987).
 62. R. Fisher, W. T. Masselink, J. Klem, T. Henderson, T. C. McGlenn, M. V. Klein, and H. Morkoc, "Growth and properties of GaAs/AlGaAs on nonpolar substrates using molecular beam epitaxy," *J. Appl. Phys.* **58**, 374 (1985).
 63. Y. Li, L. Lazzarini, L. J Giling, and G. Salviati. "On the sublattice location of GaAs grown on Ge," *J. Appl. Phys.* **76**, 5748-5753 (1994).
 64. Y. Li, G. Salviati, M. M. G. Bongers, L. Lazzarini, L. Nasi and L. J. Giling, "On the formation of antiphase domains in the system of GaAs on Ge," *J Cryst. Growth* **163**, 195-202 (1996).

65. S. M. Ting, E. A. Fitzgerald, R. M. Sieg, and S. A. Ringel, "Range of Defect Morphologies on GaAs grown on offcut (001) Ge substrates," *J. Electron. Mater.* **27**, 451 (1998).
66. J. Chadi, "Stabilities of single-layer and bilayer steps on Si (001) surfaces," *Phys. Rev. Lett.* **59**, 1691-1694 (1987).
67. E. Aspnes and J. Ihm, "Biatomic steps on (001) silicon surfaces," *Phys. Rev. Lett.* **57**, 3054-3057 (1986).
68. M. K. Hudait and S. B. Krupanidhi, "Self-annihilation of antiphase boundaries in GaAs epilayers on Ge substrates grown by metal-organic vapor phase epitaxy," *J. Appl. Phys.* **89**, 5972-5979 (2001).
69. N.-H. Cho and C. B. Carter, "Formation, faceting, and interaction behaviors of antiphase boundaries in GaAs thin films," *J. Mat. Sci.* **36**, 4209-4222 (2001).
70. P. M. Petroff, "Nucleation and growth of GaAs on Ge and the structure of antiphase boundaries," *J. Vac. Sci. Technol. B* **4**, 874-877 (1986).
71. Y. G. Galitsyn, S. P. Moshchenko, and A. S. Suranov, "Reconstruction transition (4×2) to (2×4) on the (001) surfaces of InAs and GaAs," *Semi. Struct. Interf. & Surf.* **34**, 180-185 (2000).
72. Ohtake, M. Ozeki, T. Yasuda, and T. Hanada, "Atomic structure of the GaAs (001)-(2×4) surface under As flux," *Phys. Rev. B* **65**, 165315 (2002).
73. D. J. Chadi, "Atomic structure of GaAs (100)-(2×1) and (2×4) reconstructed surfaces," *J. Vac. Sci. Technol. A* **5**, 834-837 (1987).
74. W. G. Schmidt, S. Mirbt and F. Bechstedt, "Surface phase diagram of (2×4) and (4×2) reconstructions of GaAs (001)," *Phys. Rev. B* **62**, 8087-8091 (2000).
75. L. Scaccabarozzi, "Gallium Arsenide waveguides for non-linear optical applications," M.S. thesis, Stanford University, Stanford, CA (2001).
76. Y. Horikoshi, "Migration-enhanced epitaxy of GaAs and AlGaAs," *Semicond. Sci. Technol.* **8**, 1032 (1993).
77. M. Kawashima, S. Tadashi, and Y. Horikoshi, "Characteristics of AlGaAs/GaAs heterostructures grown by migration-enhanced epitaxy at high temperatures," *Semicond. Sci. Technol.* **10**, 1237 (1995).
78. J. Taftø and J. C. H. Spence, "A simple method for the determination of structure-factor phase relationships and crystal polarity using electron diffraction," *J. Appl. Cryst.* **15**, 60-64 (1982).
79. T. S. Kuan and C.-A. Chang, "Electron microscope studies of a Ge-GaAs superlattice

- grown by molecular beam epitaxy,” *J. Appl. Phys.* **54**, 4408-4413 (1983).
80. W. Mader and A. Recnik, “Determination of crystal polarity by electron diffraction from thin crystals,” *Phys. Stat. Sol. (a)* **166**, 381-395 (1998).
 81. R. K. Tsui, J. A. Curlless, G. D. Kramer, and M. S. Peffley, D. L. Rode, “Effects of substrate misorientation on the properties of (Al, Ga)As grown by molecular beam epitaxy,” *J. Appl. Phys.* **58**, 2570-2571 (1985).
 82. J. Massies, C. Deparis, C. Neri, and G. Neu, Y. Chen, and B. Gil, “Smooth, pseudosmooth, and rough GaAs/Al_xGa_{1-x}As interfaces: effect of substrate misorientation,” *Appl. Phys. Lett.* **55**, 2605-2607 (1989).
 83. Poudoulec, B. Guenais, C. Danterroches, P. Auvray, M. Baudet, and A. Regreny, “Comparative study of interface structure in GaAs/AlAs superlattices grown by molecular beam epitaxy on (001) GaAs substrates misoriented towards (111)_{Ga} or (111)_{As} plane,” *Appl. Phys. Lett.* **60**, 2406-2408 (1992).
 84. T. Shitara, D. D. Vvedensky, and M. R. Wilby, J. Zhang, J. H. Neave, and B. A. Joyce, “Misorientation dependence of epitaxial growth on vicinal GaAs (001),” *Phys. Rev. B* **46**, 6825-6833 (1992).
 85. M. D. Pashley; K. W. Haberern; J. M. Gaines, “Scanning tunneling microscopy comparison of GaAs(001) vicinal surfaces grown by molecular beam epitaxy,” *Appl. Phys. Lett.* **58**, 406-408 (1991).
 86. D. C. Radulescu, G. W. Wicks, W. J. Schaff, A. R. Calawa, and L. F. Eastman, “Influence of substrate misorientation on defect and impurity incorporation in GaAs/AlGaAs heterostructures grown by molecular-beam epitaxy,” *J. Appl. Phys.* **63**, 5115-5120 (1988).
 87. S. Schinzer, S. Kohler, G. Reents, “Ehrlich-Schwoebel barrier controlled slope selection in epitaxial growth,” *Eur. Phys. J. B* **15**, 161-168 (2000).
 88. M. A. Salmi, M. Alatalo, T. Ala-Nissila, R. M. Nieminen, “Energetics and diffusion paths of gallium and arsenic adatoms on flat and stepped GaAs(001) surface,” *Surf. Sci.* **425**, 31-47 (1999).
 89. P. Smilauer, Dimitri D. Vvedensky, “Step-edge barriers on GaAs (001),” *Phys. Rev. B* **48**, 17603-17606 (1993).
 90. K. Shiraishi, “Ga adatom diffusion on an As-stablized GaAs (001) surface via missing As dimmer rows: first-principle calculation,” *Appl. Phys. Lett.* **60**, 1363-1365 (1992).
 91. Q.-M. Zhang, C. Roland, P. Boguslawski, and J. Bernholc, “Ab Initio studies of the diffusion barriers at single-height Si (100) steps,” *Phys. Rev. Lett.* **75**, 101-104 (1995).

92. M. Itoh, and T. Ohno, "Absence of a step edge barrier on a polar semiconductor surface with reconstruction," *Phys. Rev. B* **62**, 1889-1896 (2000).
93. Kley, P. Ruggerone, and M. Scheffler, "Novel diffusion mechanism on the GaAs (001) surface: the role of adatom-dimer interaction," *Phys. Rev. Lett.* **79**, 5278-5281 (1997).
94. J. G. LePage, M. Alouani, D. L. Dorsey, J. W. Wilkins, P. E. Blochl, "Ab initio calculation of binding and diffusion of a Ga adatom on the GaAs (001)-c-(4×4) surface," *Phys. Rev. B* **58**, 1499-1505 (1998).
95. K. Seino, W. G. Schmidt, F. Bechstedt, J. Bernholc, "Structure and energetics of Ga-rich GaAs (001) surfaces," *Surf. Sci.* **507-510**, 406-410 (2002).
96. S. J. B. Yoo, C. Caneau, R. Bhat, M. A. Koza, A. Rajhel, and N. Antoniadis, "Wavelength conversion by difference frequency generation in AlGaAs waveguides with periodic domain inversion achieved by wafer bonding," *Appl. Phys. Lett.* **68**, 2609-2611 (1996).
97. C. Q. Xu, K. Takemasa, K. Nakamura, K. Shinozaki, H. Okayama, and T. Kamijoh, "Device length dependence of optical second-harmonic generation in AlGaAs quasi-phase matched waveguides," *Appl. Phys. Lett.* **70**, 1554-1556 (1997).
98. X. Yu, L. Scaccabarozzi, O. Levi, T. J. Pinguet, M. M. Fejer and J. S. Harris, "Template design and fabrication for low loss orientation-patterned nonlinear AlGaAs waveguides pumped at 1.55 μm ," *J. Cryst. Growth.* **251**, 794-799 (2003).
99. M. Hata, T. Isu, A. Watanabe, and Y. Katayma, "Distributions of growth rate on patterned surfaces measured by scanning microprobe reflection high-energy electron diffraction," *J. Vac. Sci. Technol. B* **8**, 692-696 (1990).
100. H. Kuriyama, M. Ito, K. Suzuki and Y. Horikoshi, "Determination of the facet index in area selective epitaxy of GaAs," *Jpn. J. Appl. Phy.* **39**, 2457-2459 (2000).
101. Gil-Lafon, J. Napierala, D. Castelluci, A. Pimpinelli, R. Cadoret, and B. Gérard, "Selective growth of GaAs by HVPE: keys for accurate control of the growth morphologies," *J. Cryst. Growth* **222**, 482-496 (2001).
102. R. S. Williams, M.J. Ashwin, J.H. Neave, T.S. Jones, "Optimizing the growth of pyramidal GaAs microstructures on pre-patterned GaAs(0 0 1) substrates," *J. Cryst. Growth* **227-228**, 56-61 (2001).
103. S. Koshiba, Y. Nakamura, T. Noda, S. Watanabe, H. Akiyama, H. Sakaki, "Transformation of GaAs (0 0 1)-(1 1 1)B facet structure by surface diffusion during molecular beam epitaxy on patterned substrates," *J. Cryst. Growth* **227-228**, 62-66 (2001).

104. W. Braun, V. M. Kaganer, A. Trampert, H. Schonherr, Q. Gong, R. Notzell, L. Daweritz, K. H. Ploog, "Diffusion and incorporation: shape evolution during overgrowth on structured substrates," *J. Cryst. Growth* **227–228**, 51-55 (2001).
105. R. S. Williams, M. J. Ashwin, and T. S. Jones, J. H. Neave, "Influence of the growth conditions on the ridge morphology during GaAs deposition on GaAs (001) patterned substrates," *J. Appl. Phys.* **95**, 6112-6118 (2004).
106. R. S. Williams, M. J. Ashwin, T. S. Jones and J. H. Neave, "Ridge structure transformation by group-III species modification during the growth of AlGaAs on patterned substrates," *J. Appl. Phys.* **97**, 044905 (2005).
107. R. J. Deri, E. Kapon and L. M. Schiavone, "Rib profile effects on scattering in semiconductor optical waveguides," *Appl. Phys. Lett.* **53**, 1483-1485 (1988).
108. R. T. Feuchter and C. Thirstrup, "High precision planar waveguide propagation loss measurement technique using a Fabry-Perot cavity," *IEEE Photon. Tech. Lett.* **6**, 1244-1247 (1994).
109. X. Yu, L. Scaccabarozzi, J. Harris, Jr., P. Kuo, and M. Fejer, "Efficient continuous wave second harmonic generation pumped at 1.55 μm in quasi-phase-matched AlGaAs waveguides," *Opt. Express* **13**, 10742-10748 (2005)
110. N. Pikhtin and A. D. Yas'kov, "Dispersion of the refractive index of semiconductors with diamond and zinc-blend structures," *Sov. Phys. Semicond.* **12**, 622 (1978).
111. K. J. Bachmann, U. Rossow, N. Sukidi, H. Castleberry, and N. Dietz, "Heteroepitaxy of GaP on Si (100)," *J. Vac. Sci. Technol. B* **14**, 3019-3029 (1996).
112. M. A. Lemay, P. E. Crago, W. G. Bi, X. B. Mei and C. W. Tu, "Growth studies of GaP on Si by gas-source molecular beam epitaxy," *J. Cryst. Growth* **164**, 256-262 (1996).
113. M. Sadeghi, S. Wang, "Growth of GaP on Si substrates by solid-source molecular beam epitaxy," *J. Cryst. Growth* **227-228**, 279-283 (2001).
114. Kroemer, K. J. Polasko, and S. C. Wright, "On the (110) orientation as the preferred orientation for the molecular beam epitaxial growth of GaAs on Ge, GaP on Si, and similar zinblend-on-diamond systems," *Appl. Phys. Lett.* **36**, 763-765 (1980).
115. S. L. Wright, M. Inada, and H. Kroemer, "Polar-on-nonpolar epitaxy: Sublattice ordering in the nucleation and growth of GaP on Si (211) surfaces," *J. Vac. Sci. Technol.* **21**, 534-539 (1982).
116. S. L. Wright, H. Kroemer, and M. Inada, "Molecular beam epitaxy growth of GaP on Si," *J. Appl. Phys.* **55**, 2916-2927 (1984).

117. B. W. Liang and C. W. Tu, "A study of group-V desorption from GaAs and GaP by reflection high energy electron diffraction in gas-source molecular beam epitaxy," *J. Appl. Phys.* **72**, 2806-2809 (1992).
118. S. L. Wright and H. Kroemer, "Operational aspects of a gallium phosphide source of P₂ vapor in molecular beam epitaxy," *J. Vac. Sci. Technol.* **20**, 143-148 (1982).
119. M. J. Mondry, E. J. Caine, and H. Kroemer, "A GaP decomposition source for producing a dimmer phosphorus molecular beam free of gallium and tetramer phosphorus," *J. Vac. Sci. Technol. A* **3**, 316-318 (1985).
120. R. D. Bringans, D. K. Biegelsen, and L.-E. Swartz, "Atomic-step rearrangement on Si (100) by interaction with arsenic and the implication for GaAs-on-Si epitaxy," *Phys. Rev. B* **44**, 3054-3063 (1991).
121. R. Clawson, "Guide to references on III-V semiconductor chemical etching," *Mat. Sci. Eng.* **31**, 1-438 (2001).
122. E. Kapon and R. Bhat, "Low-loss single-mode GaAs/AlGaAs optical waveguides grown by organometallic vapor phase epitaxy," *Appl. Phys. Lett.* **50**, 1628-1630 (1987).
123. R. J. Deri, E. Kapon, and L. M. Schiavone, "Scattering in low-loss GaAs/AlGaAs rib waveguides," *Appl. Phys. Lett.* **51**, 789-191 (1987).
124. R. J. Deri and E. Kapon, "Low-loss III-V semiconductor optical waveguides," *IEEE J. Quan. Electron.* **27**, 626-640 (1991).
125. R. Y. Fang, D. Bertone, M. Meliga, G. Magnetti, G. Morello, S. Murgia, G. Olivetti, R. Paoletti, and G. Rossi, "1.55 μm InGaAsP-InP spot-size-converted (SSC) laser with simple technological process," *IEEE Photon. Technol. Lett.* **10**, 775-777 (1998).
126. K. Uppal, D. Tishinin, I. Kim, and P. D. Dapkus, "Study of 1.3- μm tapered waveguide spotsizer transformers," *IEEE Journal of Selected Topics In Quantum Electronics* **3**, 975-979 (1997).